AN EXPERIMENTAL STUDY OF CRACK INITIATION AND GROWTH FROM COLDWORKED HOLES

Dissertation for the Degree of Ph. D.

MICHIGAN STATE UNIVERSITY
NOPPORN CHANDAWANICH

1977

This is to certify that the

thesis entitled

An Experimental Study of Crack Initiation and
Growth From Coldworked Holes

presented by

Nopporn Chandawanich

has been accepted towards fulfillment
of the requirements for

Ph.D. degree in Mechanics

William N Sharpe Jr

Major professor

Date July 22, 1977

O-7639

ABSTRACT

AN EXPERIMENTAL STUDY OF CRACK INITIATION AND GROWTH FROM COLDWORKED HOLES

By

Nopporn Chandawanich

Crack initiation and crack growth behavior can be improved by coldworking a fastener hole. This report describes the experimental studies investigating the change of residual strain during crack initiation, the stress intensity factor for the crack emanating from a circular hole, and the strains ahead of a crack tip. The specimens were subjected to low-cycle fatigue conditions. Analytical procedures were evaluated based on correlation with the test data. These procedures included elastic/plastic analysis which was utilized to determine the stress-strain distribution surrounding the fastener holes and ahead of the crack tip. The experimental data showed that the moiré method is acceptable for measuring the strains in this investigation.

The data revealed that the relation between the total notch strain range and cycles to initiation is satisfactory for engineering predictions. The comparison of the crack initiation life of base line fatigue data to the test

data was favorable if initiation was defined as the development of a 0.006 inch (0.15 mm) crack.

Crack growth rate and interferometric displacement gage (IDG) techniques were used to determine the stress intensity factor (K_I). The test data for the coldworked specimens showed that an analytical formula was good for the longer cracks but not for shorter ones.

AN EXPERIMENTAL STUDY OF CRACK INITIATION AND GROWTH FROM COLDWORKED HOLES

By

Nopporn Chandawanich

A DISSERTATION

Submitted to
Michigan State University
in partial fulfillment of the requirements
for the degree of

DOCTOR OF PHILOSOPHY

Department of Metallurgy, Mechanics,
and Materials Science

1977

ACKNOWLEDGMENTS

I wish to express my sincerest appreciation and
de to Dr. William N. Sharpe, Jr., my major professor
helpful information and suggestions during the course
investigation.

I also wish to take this opportunity to thank
L. Cloud, Dr. J. S. Frame, Dr. G. E. Mase and Dr.
cGrady for serving as the Guidance Committee.

I would like to give grateful thanks to the Royal
r Force which sponsored my graduate program.

Grateful acknowledgment is hereby extended to the
ce Office of Scientific Research which provides the
or this study.

I want to pay special tribute to my wife, Suvalai,
wonderful patience, encouragement, and help in taking
our children during my study. My special thanks to
t. Martin and Mr. W. J. Cesarz, Jr., for reviewing the
pt of my thesis.

TABLE OF CONTENTS

LIST OF TABLES

LIST OF FIGURES

CHAPTER 1

INTRODUCTION

The presence of cracks or flaws in structural com-
ts has resulted in the catastrophic failure of a
ty of engineering structures. Analyses of the failed
nents of pressure vessels, storage tanks, welded ship
tures, aircraft parts, bridges, pipelines, turbine
s and housings, rocket motor casings and various heavy
ne parts, have shown that crack- or flaw-induced frac-
is often responsible for the failures.

In recent years the operational lives of many mili-
nd commercial aircraft have been limited by flaws
initiate from bolt or rivet holes of aircraft struc-
and propagate to failure. It is necessary for the
er to account for the presence of flaws in the design
aircraft structure.

One way to protect against flaws is to use materials
high value of fracture toughness. However, this is
y associated with a decrease in yield strength of the
al which reduces the load-carrying capacity. The
er also has to account for weight-saving which is one
most important criteria for aircraft design.
Another economical technique to improve the fatigue
the structure is to inhibit or slow the growth of

ys emanating from the holes. This can be done by pre-
essing the metal around the hole either by coldworking
n an oversized mandrel or by interference-fit fasteners.
slower growth of flaws is attributed to compressive
idual stresses around the edge of the hole generated by
pre-stressing operation. The improvement of fasteners
processing techniques requires an understanding of the
idual stress state around the hole and the change in this
ess state with static or fatigue loading.

Purpose and Motivation

The purpose of this research is to study the change
the residual strain field around coldworked holes during
tiation of cracks, and the crack opening displacements
strains as the crack propagates. This investigation
ludes the studies of crack initiation, crack propagation
avior, the stress intensity factor, and the strain ahead
the crack tip.

The earliest theoretical study of the coldworked
dual stress and strain behavior by Nadai (1) is still
useful today. In recent years, among the various ana-
cal theories considered, the Hsu-Forman (2) and the
er-Ting-Grandt (3,4) are the best. The theories assume
the hole is radially loaded and a state of plane stress
s everywhere in the sheet, and that the sheet is
ite in extent. The theories have difficulty predicting
esidual stress/strain state near the hole edge.

From a mechanics viewpoint, failure of the metal
s at the highly strained regions where cracks initiate.
local repeated plastic strain is responsible for crack
ation (5), procedures that account for the crack
ation due to this strain would be expected to result in
accurate fatigue life estimations than procedures based
minal stresses away from the stress concentration.
tical studies for the local stresses and strains have
performed elastically by Timoshenko-Goodier (6), and
nd (7); and plastically by Neuber (8), and Stowell (9).
the local stresses and strains have been determined, a
ty of methods exists for estimating the number of the
initiation cycles.

The analytical study of the stress intensity factor
or the non-coldworked holes was originated by Bowie (10)
ter modified by Grandt (11). In the Grandt solution,
ack face pressure p(x) can be defined either as the
stress caused by remote load for the non-coldworked
or the addition of that local stress and the compres-
esidual stress caused by a coldworking process for the
rked holes. If the residual stresses were accurately
the Grandt solution for K_I as a function of crack
should be accurate.

Experimental information about the nature of the
field around a coldworked hole obtained by Adler-
(12) and Sharpe (13) does not agree with the theories.

work has been done experimentally on the change of the esidual strains during crack initiation for the coldworked les in a plane stress condition. The only existing experental study employs fatigue crack growth rates to determine stress intensity factor calibrations for coldworked les. This study has been conducted by Grandtnnerichs (14). Some experimental error in their study y be introduced by differentiating the data especially r longer crack lengths, the growth rates of which are ry high.

Moiré, IDG, and crack length measurements are the chniques used for determining the strain and the stress tensity factors in this investigation. The moiré method observe the fringe pattern change during uniaxial tenon and measure the displacement in a strained body with isfactorily accurate results. The IDG technique, which loys laser interferometry, is quite sensitive (about 0.1 ron resolution) and provides most acceptable results. ck length measurements are made in this investigation to ermine the stress intensity factor for small displacets at very short crack (less than 1 mm), for which the technique is not applicable.

Organization of Dissertation

The description of the material used in this investation, its properties, coldworking procedure, and specipreparation are given in the first part of Chapter 2.

The experimental procedures for fatigue testing, the techniques for the moiré method and the interferometric displacement gage (IDG) are also described in Chapter 2. A brief review of the coldworking theories and the results of measured coldworking strains are presented in Chapter 3.

Theoretical stress concentration factors, both elastic and plastic, the base line fatigue data for 7075-T6 aluminum, the crack initiation behavior, and the number of cycles required to initiate the crack for various coldworked holes are described in Chapter 4. Chapter 5 shows the large difference in crack growth data between non-coldworked and coldworked specimens. The crack closure which caused the crack to close above zero load and decreased the amount of crack opening is presented in Chapter 6.

Chapter 7 discusses the stress intensity factors from the Bowie solution for the non-coldworked hole and the Grandt solution for the coldworked hole compared with the measured results from the IDG and crack growth technique. Crack mouth displacements and crack surface profiles are given in Chapter 8.

The theoretical solutions, both plastic and elastic with plastic zone correction factor, for the strains ahead of the crack tips compared with the measured strains by moiré method are discussed in Chapter 9. The thesis concludes with Chapter 10 which discusses the findings of this investigation.

CHAPTER 2

EXPERIMENTAL PROCEDURES

Material Specification and Specimen Preparation

.1 Coldworking Procedure

The coldworking procedure studied in this research is one developed by

J. O. King, Inc.
711 Trabert Avenue, N.W.
Atlanta, Georgia 30318

A thin-walled (about 0.0075 inch (0.19 mm) thick) ve is first inserted into the hole. A tapered mandrel is pulled through this sleeve. After the mandrel has been ved, the sleeve may or may not be removed before the ener is inserted, but usually the sleeve is left in the . The specific amounts of expansion used in this study 0.0080 inch (0.20 mm) and 0.012 inch (0.30 mm) diametral nsion of the 0.196 inch (4.98 mm) holes. The sleeve was ved for these experiments because none of the modern ies for plane stress condition account for the pressure sleeve.

Material Specifications

The material used for this study was aluminum type T6, 1/8 inch (3.20 mm) thick. The stress-strain curve photograph of the microstructure are shown in Figures nd 2.2. The Rockwell B hardness measurement for this

material is

$$R_B = 90.3$$

An ASTM standard tension test specimen was cut from the same sheet as the specimens. Different dimensions were used in order to fit the tension test specimen to the testing machine. This specimen was pulled in uniaxial tension at a strain rate of 0.0267 in./in. per min. Foil gages were applied to measure the strain. The tensile strengths obtained are:

Yield strength (0.2% offset)	73.0 ksi
Ultimate strength	76.5 ksi

A Ramberg-Osgood representation was used for representing the constitutive behavior of the material in the plastic range using the stress-strain curve in Figure 2.1. The form of the Ramberg-Osgood relation is

$$\frac{\varepsilon_p}{\varepsilon_{ys}} = \alpha \left(\frac{\sigma_p}{\sigma_{ys}}\right)^n \qquad (2.1)$$

where ε_p is the plastic strain

ε_{ys} is the tensile yield strain = $\frac{\sigma_{ys}}{E}$ where σ_{ys} is the tensile yield stress and E is the initial slope of the stress-strain curve,

σ_p is the plastic stress

α is a material constant,

n is a power hardening coefficient.

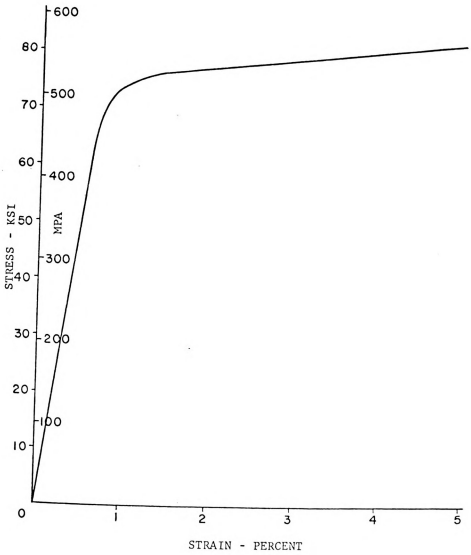

gure 2.1 Stress-strain curve for the test specimen of 7075-T6 aluminum.

Figure 2.2 Photomicrograph of the test specimen of 7075-T6 aluminum. Magnification x 100.

The experimentally determined values of the power hardening coefficient n = 15, and the material constant α = 1.

2.1.3 Specimen Preparation

The dimensions shown in Figure 2.3 were used for all specimens in this investigation. The specimens were prepared by the machine shop to obtain round, nontapered holes to a specific dimension so that one can accurately measure the amount of coldworking deformation. A certain tolerance on the holes is required if one is to compare coldworking between various specimens.

Holes were prepared by first drilling them with a 0.1875 inch (4.760 mm) drill and then using a honing machine to bring the diameter up to the nominal 0.195 ±0.0020 inch (4.953 ±0.051 mm). The honing machine produced straight walls in the hole (no evidence of spiraling) and square edges of the hole. The size was determined with a plug gage with a "go" cylinder of 0.1948 inch (4.948 mm) and a "no-go" cylinder of 0.1952 inch (4.958 mm). Upon receipt from the machine shop, the holes in the specimens were measured with a microscope equipped with an x-y stage. The greatest uncertainty in this measurement is in locating the edges of the holes accurately. Measurements were made along the diameter at 45 degree intervals, and each measurement was repeated at least three times. The variation in repeated measurements was usually less than 0.0001 inch (3 microns). Typical diameters measured for the specimens

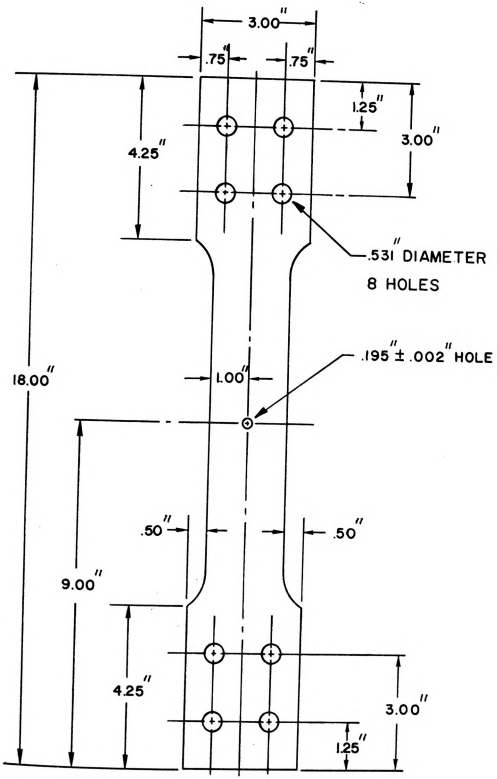

Figure 2.3 Dimensions of the test specimen.

are given in Table 2.1. From this measurement it was found that the hole diameters varied from 0.195 inch (4.966 mm) to 0.1999 inch (5.078 mm).

TABLE 2.1.--Diameter of Holes (in Inches) for the Specimens

Specimen	0°	45°	90°	135°
1	0.1963	0.1957	0.1961	0.1960
2	0.1994	0.1987	0.1993	0.1989
3	0.1980	0.1982	0.1982	0.1980
4	0.1995	0.1996	0.1999	0.1993
5	0.1958	0.1958	0.1954	0.1955
6	0.1956	0.1956	0.1956	0.1955
7	0.1958	0.1959	0.1958	0.1956
8	0.1958	0.1958	0.1959	0.1957

After the holes had been measured, the surface of the specimens was coated with a moiré grille by a process which will be explained in detail in Section 2.3. The holes were then coldworked by pulling a mandrel through them, as illustrated by the schematic in Figure 2.4. The tapered mandrel is inserted into the sleeve, and the mandrel and sleeve inserted into the hole. The washer of the sleeve is pressed against an anvil, and the mandrel pulled through the sleeve. This is the same as the industrial process specified by J. O. King, Inc. A machine incorporating a hand-operated hydraulic cylinder was constructed to pull a

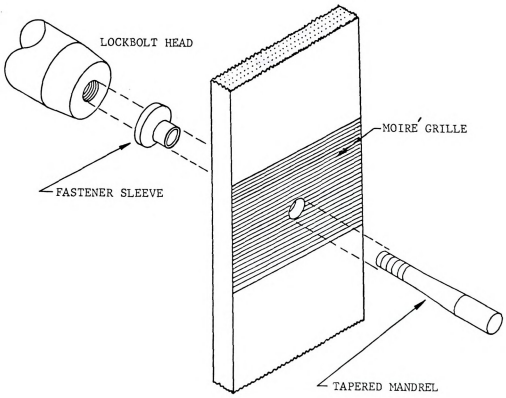

Figure 2.4 Schematic of the King coldworking process and moiré printing.

mandrel in the laboratory; a photograph of it is given in Figure 2.5. The tension rod linking the mandrel to the cylinder piston had been instrumented with strain gages to permit calibration of the force in terms of the cylinder hydraulic pressure. A typical load-displacement curve for pulling a mandrel through the hole is shown in Figure 2.6. The peak forces for the 0.0040 inch (0.102 mm) radial expansion was 1250 pounds (5.56 KN) and for the 0.0060 inch (0.152 mm) radial expansion was 1300 pounds (5.785 KN).

The sleeves inserted in the hole were part number JK 5535-C06N10L from J. O. King, Inc. These were supplied with the mild steel washer attached (see Figure 2.7), and a dry film lubricant applied to the inside and outside. The function of the mild steel washer is simply to protect the sleeve and specimen as the mandrel is pulled through; it pops off after coldworking. Several sleeves were sectioned, and the average wall thickness was found to be 0.0075 inch (0.19 mm).

The 0.188, 0.190 and 0.192 inch (4.775, 4.826 and 4.877 mm) mandrels used were J. O. King, Inc. part numbers JK 6540-06-188 to 192; one is shown in Figure 2.7. According to the J. O. King, Inc. literature, the 0.192 inch (4.877 mm) diameter mandrel will give a radial expansion of 0.0070 inch (0.178 mm) to a 0.195 inch (4.953 mm) hole, but this is based on a sleeve thickness of 0.0085 inch (0.216 mm). A maximum radial expansion of 0.0060 inch (0.152 mm) would be achieved with the 0.0075 inch (0.191 mm) thick

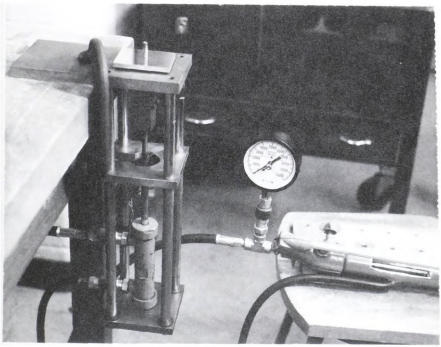

Figure 2.5 Photograph of the device for pulling the mandrel through the hole.

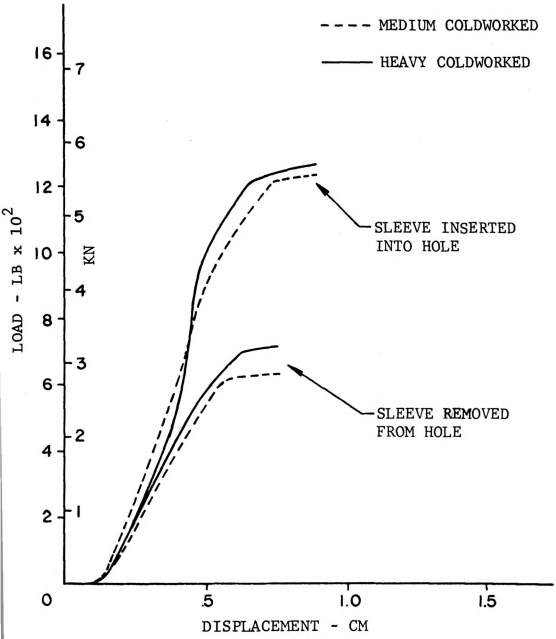

Figure 2.6 Load-displacement curves for pulling the mandrel through the hole.

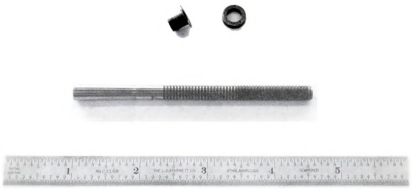

Figure 2.7 Photograph of the mandrel and sleeve.

sleeves. Because of the variation of the hole diameters the size of the mandrels had to be selected to obtain the right amount of coldworking.

The sleeve is tightly wedged into the hole after the mandrel has been pulled through it. To remove the sleeve, the washer on the end of it was surrounded by a larger washer for the anvil to react against and the mandrel was pulled through it a second time. The force required to pull the sleeve out was approximately 650-720 pounds (2.89-3.20 KN). The dimensions of the holes and the residual diametral expansion after the removal of the sleeve are shown in Tables 2.2 and 2.3. The deformed regions near the hole edge for 0.0040 inch (0.102 mm) and 0.0060 inch (0.152 mm) radial expansions are shown in Figure 2.8.

TABLE 2.2.--Hole dimensions (in inches) of specimens after sleeve removal.

Specimen	Mandrel Diameter (inch)	0°	45°	90°	135°
1	0.188	0.2041	0.2034	0.2039	0.2035
2	0.192	0.2071	0.2069	0.2074	0.2069
3	0.190	0.2056	0.2060	0.2057	0.2056
4	0.192	0.2065	0.2066	0.2066	0.2065
5	0.192	0.2077	0.2076	0.2075	0.2075
6	0.192	0.2067	0.2062	0.2070	0.2063
7	0.192	0.2080	0.2083	0.2080	0.2077
8	0.192	0.2063	0.2062	0.2064	0.2060

TABLE 2.3.--Residual diametral expansion (in inches).

Specimen	0^{o}	45^{o}	90^{o}	135^{o}
1	0.0078	0.0077	0.0078	0.0075
2	0.0077	0.0082	0.0081	0.0080
3	0.0076	0.0078	0.0075	0.0076
4	0.0070	0.0070	0.0067	0.0072
5	0.0119	0.0118	0.0121	0.0120
6	0.0111	0.0106	0.0114	0.0108
7	0.0122	0.0124	0.0122	0.0121
8	0.0105	0.0104	0.0105	0.0103

Sharpe (13) found that the hole is not uniform through the plate thickness after coldworking; it is slightly smaller on the back side where the washer is attached to the sleeve. The nature of the coldworking operation is to exert a force perpendicular to the specimen surface through the sleeve and thus constrain deformation of the hole on the back side.

2.2 Fatigue Testing Procedure

This section describes the experimental methods and techniques used in fatigue testing of the aluminum specimens. They were tested in a servocontrolled closed-loop hydraulic testing machine, and all tests were performed at room temperature (70-75°F).

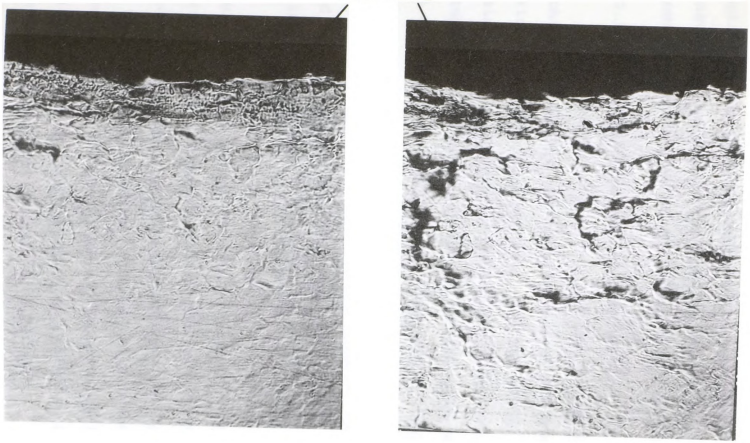

Figure 2.8 Photographs of the deformed region around the hole for; (a) 0.0040 inch (0.102 mm), and (b) 0.0060 inch (0.152 mm) radial expansion.

A moiré grille was used to measure strains on the specimen surfaces. A load cell was used to monitor the load applied to the specimen; a traveling microscope was used to measure the lengths of the propagating cracks. Figure 2.9 shows an overall view of the experimental setup.

2.2.1 Servocontrolled Testing Machine

The servocontrolled closed-loop hydraulic testing machine (series 810) was manufactured by MTS Systems Corporation, Minneapolis, Minnesota. The MTS series 810 consists basically of a hydraulic power supply model 506.02, an actuator (servoram) model 204.63, a load frame model 312.21, the electronic control console model 406.11, and a function generator model 410. A load cell model 661.21A-03 connects in series with the specimen and the actuator ram senses the load applied to the specimen. The machine has a dynamic rating of ±20 kips.

The actuator is connected to the hydraulic power supply through a servovalve and a hydraulic accumulator. Hydraulic fluid is ported through the servovalve to the actuator's cylinder, causing ram movement and applied force. The magnitude and direction of fluid through the servovalve is controlled by a signal from the servocontroller. Hydraulic power is supplied by a pump rated at 6 gallons per minute with a maximum pressure of 3,000 psi.

The control console consists of a servocontroller, a control unit, a function generator, a cycle counter, and a

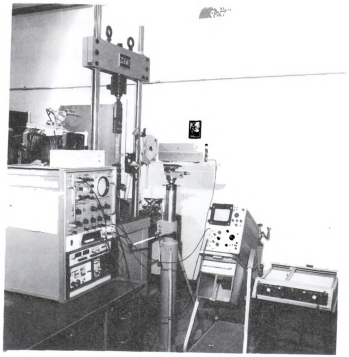

Figure 2.9 Overall view of the experimental setup.

transducer output panel. Servoram movement is controlled through the servovalve. This servovalve opens or closes according to the control signal from the servocontroller. An input module which is plugged into the servocontroller receives a programmed signal from the function generator, and after scaling it suitably, combines it with the manual command to give a composite command. Manual command is fed through the set point and/or span control of the input module. Composite command and feedback signals are compared by the servocontroller. Thus the servocontroller acting as a comparator-controller causes the control quantity (load or strain) to follow the output of the function generator. The command signal has a full scale input amplitude of ±10 VDC. The servocontroller has an error detector circuit that can open a system failsafe interlock to stop the test if an error between command and feedback exceeds a preset limit. The output signal is indicated by both a digital voltmeter (DVM) and an oscilloscope.

The servocontrolled hydraulic actuator loads and thus strains the specimen. Haversine waveforms were used throughout this investigation with a testing frequency of 15 cycles per second. All specimens were fatigue loaded in increments of 5,000 cycles up to 15,000 cycles, then changed to increments of 500 cycles for the noncoldworked specimens and 2,000 cycles for the coldworked specimens until cracks were seen with the microscope. After a crack had initiated,

the increments of fatigue loading were 200 cycles for the noncoldworked and 5,000 cycles for the coldworked specimens.

2.2.2 Mounting of Specimens

The specimen dimensions shown in Figure 2.3 were chosen to suit the load capacity of the machine and factors influencing the stress diffusion from grip portion to the test section. The specimens were mounted in a pair of specially made grips, the top one attached to the load cell and the bottom attached to the piston rod (see Figure 2.10). These grips had holes corresponding to those in the specimens (Figure 2.3). The holes were 0.531 inch (13.49 mm) in diameter to accommodate the four bolts in each grip. Figure 2.10 shows the specimen and grips in position. Care was taken to eliminate any twisting of the specimen before cycling.

Because of the long distance between grip section and test section, the holes in the grip section have little effect on the stress distribution in the test section. Stresses are assumed to be uniformly distributed at the area more than two inches above and below the test section.

2.3 Moiré Techniques

All of the strain measurements in this investigation were obtained using moiré techniques. The application of the moiré-fringe technique to the measurement of displacement was developed in England beginning in 1951. The moiré effect is an optical phenomenon observed when two closely

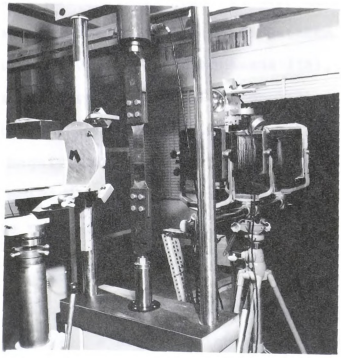

Figure 2.10 Specimen setup on the MTS.

spaced arrays
either transm
producing the
and Parks (15
provides whol
ticity. Simp
oped to relat
in the specim
Sciammarella
grating on th
significant ma
through the m
strain can be

2.3.1 Grid Pr

The st
duce on the sp
sufficient lin
ment purposes.
from Photolast
Graticules Lim
Britain. A se
original maste
a parallel lig

The ma
quality submas
experimentatio

spaced arrays of lines are superimposed and viewed with either transmitted or reflected light. The basic method for producing the moiré fringe pattern was introduced by Durelli and Parks (15). This technique is quite useful, since it provides whole field data similar to that of photoelasticity. Simple mathematical relationships have been developed to relate the change in the moiré pattern to the strain in the specimen by Vinckier and Dechaene (16), and also by Sciammarella and Durelli (17). By proper choice of the grating on the specimen surface, it is possible to achieve significant magnification of the specimen's deformation through the moiré pattern; hence measurements of very small strain can be made with good resolution.

2.3.1 Grid Production

The starting point for this technique is to reproduce on the specimen a high-quality master grating having sufficient line density to be acceptable for strain-measurement purposes. One 1,000 lpi master grille was purchased from Photolastic Inc., Malvern, Pennsylvania, and one from Graticules Limited, Sovereign Way, Tonbridge, Kent, Great Britain. A set of submasters had been made from the original masters by contact printing on Kodak HRP plates in a parallel light field as shown in Figure 2.11.

The master grille from Graticules produced the high quality submasters that have been successfully used in the experimentation (see Figure 2.12).

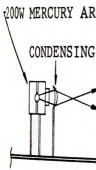

Figure 2.11

2.3.2 Printin

Before
micron alumina
the specimen wa
(which was purc
Mass.), with an
but the photore
edge. This eff
to obtain a fir
could be solved
printing proces

The pri
required the us
the illuminatio
(38.1 cm.) in f
were in contact

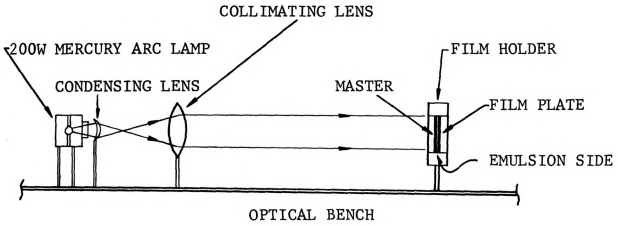

Figure 2.11.--Optical system used for producing submaster.

2.3.2 Printing of Grille on the Specimen

Before printing, the specimen was polished with 0.3 micron alumina and degreased with acetone. After cleaning, the specimen was coated by spraying AZ 1350B photoresist (which was purchased from Shipley Company, Inc., Newton, Mass.), with an airbrush. Spraying gave a fine uniform layer, but the photoresist formed a thicker coating around the hole edge. This effect caused it to be a little more difficult to obtain a fine grille around the edge of the hole, but could be solved by using a longer exposure time during printing process.

The printing process for this aluminum specimen required the use of a 200 watt mercury arc lamp to produce the illumination. This lamp was placed about 15 inches (38.1 cm.) in front of the submaster and specimen, which were in contact with each other (see Figure 2.13).


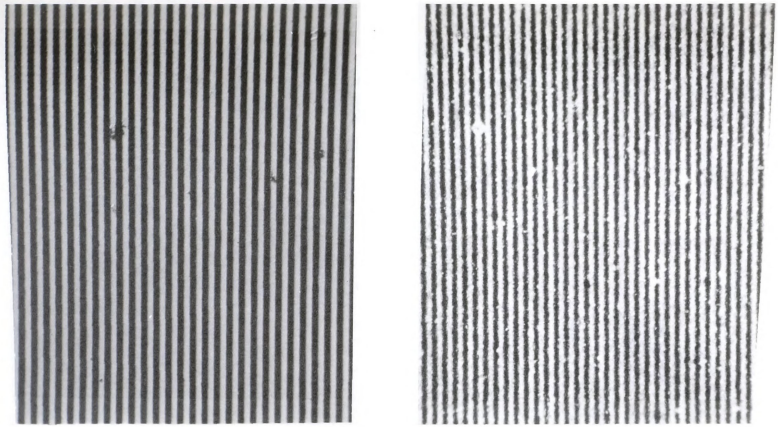

(a) (b)

Figure 2.12 1000 lines per inch grille of submaster. Magnification x 100, (a) from Graticules's master, (b) from Photolastic's master.

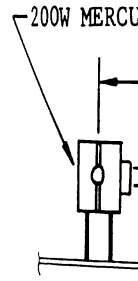

Figure 2.13.

The ex
minutes. A dc
master 90° for
are shown in F

2.3.3 Optical

The ca
Kreuznach with
length. This
angle iron bar
cation of 3.
response deman
exploited, led

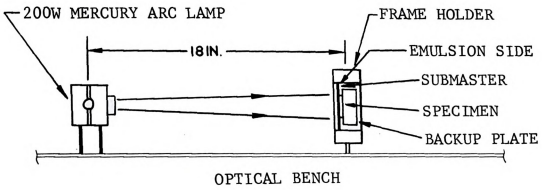

Figure 2.13.--Optical system for printing process.

The exposure of the photoresist was about 3 to 3½ minutes. A dot grating was produced by turning the submaster 90° for the second exposure. The acceptable results are shown in Figure 2.14.

2.3.3 Optical System

The camera used for this study was a Schneider Optik Kreuznach with an f4.5 lens of 300 mm (11.8 inches) focal length. This camera was mounted on a tripod and braced with angle iron bar. The camera was adjusted to obtain a magnification of 3. This use of magnification reduced the frequency response demands on the photo system and, when properly exploited, led to an increase of measurement sensitivity.

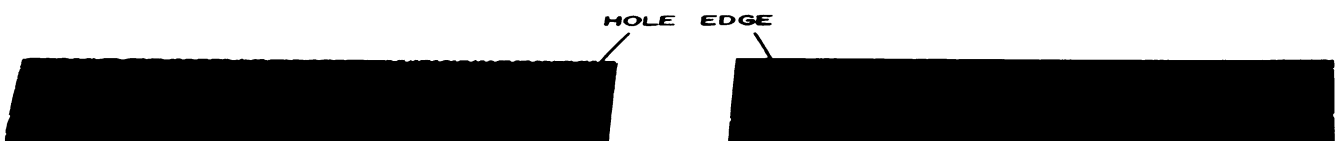
HOLE EDGE

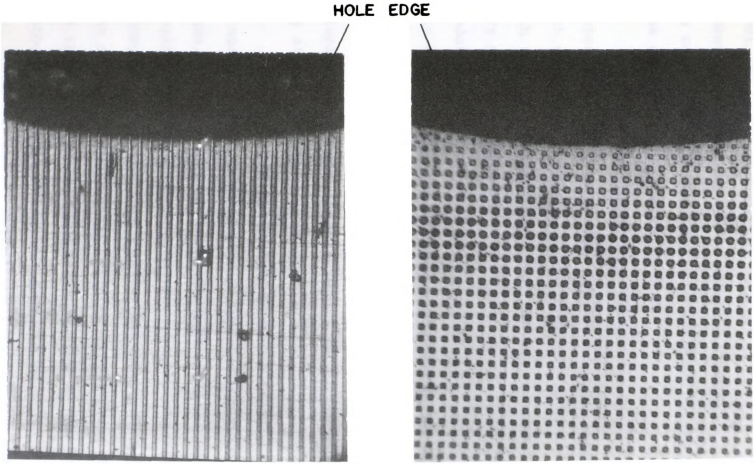

Figure 2.14 The grids around the specimen hole. Magnification x 100; (a) 1000 lines per inch, (b) 1000 dots per inch.

Illu

from a spotl

about 30° pr

improved sli

the camera be

area causing

Kodak

Plates Type 6

Both worked w

with the 649-

very good con

tendency, and

this experime

time and temp

that some dev

values could

ing stage.

Two o

fringe pattern

nique. This

specimen in a

photograph wit

tion on Kodak

was then remov

photographed a

In the

on the specime

Illuminating the specimen with diverging white light from a spotlight with the angle of incidence of the light about 30° produced the best results. Grating contrast was improved slightly by using lighting from only one side of the camera because the coated lines shadowed the uncoated area causing it to become darker.

Kodak High Resolution Plates and Kodak Spectroscopic Plates Type 649-F were used for recording grating images. Both worked well. The results reported here were obtained with the 649-F material. Kodak D-19 developer, which gives very good contrast, high effective speed with low fogging tendency, and high useful developing capacity was chosen for this experiment. The control of exposure and development time and temperature was somewhat critical. It was found that some deviation from optimum exposure and processing values could be compensated for in the optical data processing stage.

Two optical systems were used to obtain the moiré fringe patterns. One method is the double-exposure technique. This technique was performed by first mounting the specimen in a holder on an optical bench, and taking a photograph with the high resolution camera at 3:1 magnification on Kodak Spectroscopic Plates Type 649-F. The specimen was then removed, mandrelized, replaced in its holder, and photographed again using the same plate.

In the second method the image of the model grille on the specimen was projected onto Kodak 649-F plates with a

high resoluti
exposure, the
reference gri
pattern.

This
3, meaning th
equal to 3,00
readily intro
the camera in
large number
analysis. Th
photography i

The p
improved with
Cloud (18).
the iris diaph
tions were cal
cies as requir
photography to
Although the s
photography, t
obtained. Hig
be produced by
process of an
system. It al
turbance trans

high resolution camera at magnification 3:1. After the exposure, the specimen photo plates were superimposed on the reference grille of 1,000 lpi to obtain the moiré fringe pattern.

This technique improved the multiplication factor by 3, meaning that the model grille obtained the sensitivity equal to 3,000 lpi. With this method, pitch mismatch can be readily introduced. A slight change of the magnification of the camera introduced pitch mismatch which resulted in a large number of fringes producing more data points for moiré analysis. The schematic of the optical system for moiré photography is shown in Figure 2.15.

The photograph from this optical setup can be improved with the slotted apertures technique described by Cloud (18). Slotted apertures were designed to fit behind the iris diaphragm inside the lens. Slot sizes and locations were calculated to tune the lens to spatial frequencies as required. This technique was performed during photography to improve the fringe pattern (see Figure 2.16). Although the slotted-apertures technique improves the moiré photography, the highest quality pictures still cannot be obtained. Higher contrast of the moiré fringe pattern can be produced by optical fourier data processing which is the process of an optical spatial filtering in a coherent light system. It alters the input signal (i.e., the light disturbance transmitted through a moiré pattern) by placing

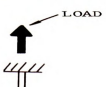
LOAD

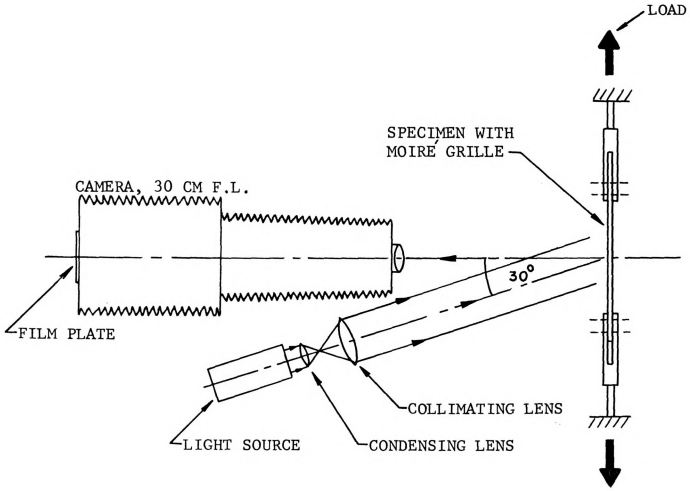

Figure 2.15 Optical system for moiré photography.

Figure 2

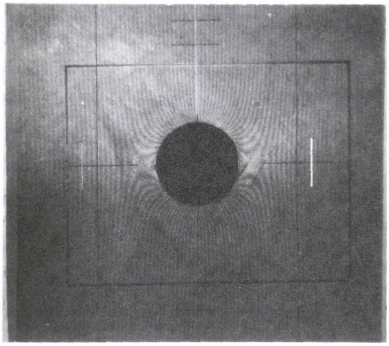

Figure 2.16 Real time moiré fringe pattern with initial mismatch for residual cold-worked specimen by slotted aperture technique. (Magnification 3:1).

spatial filte
as described
sor is in Fig
film plate (c
displacement
the optical s
plate was cor
the light was
The fringe pa
on the image.
so that it co
give an image
illustrate th
exposure and

2.3.4 Moiré

The m
is a 1,000 lp
can be measur
double-exposu
erence grille
were shifted,
be neglected.
displacement
using the fol

spatial filters along the optical path of the light system as described by Duffy (19). The photograph of this processor is in Figure 2.17 and the schematic in Figure 2.18. The film plate (containing interference fringes indicative of displacement in the specimen) was placed along the axis of the optical system. The inverse transfer or image of that plate was constructed by the camera, but only a portion of the light was allowed to pass through the filter aperture. The fringe pattern was photographed by focusing the camera on the image. The camera was mounted on a swinging support so that it could be placed behind the filter aperture to give an image without vignetting. Figures 2.19 and 2.20 illustrate the results of the method from the double-exposure and the mismatch technique, respectively.

2.3.4 Moiré Analysis of Strain

The master grille that was used in the experiments is a 1,000 lpi, unidirectional grating, therefore the strain can be measured only in one direction at a time. For the double-exposure technique, the model grille and the reference grille were placed at the same position. No lines were shifted, and therefore the original pitch mismatch can be neglected. From Durelli and Parks (15), the relative displacement between model and master is easily calculated using the following formulas.

Figure

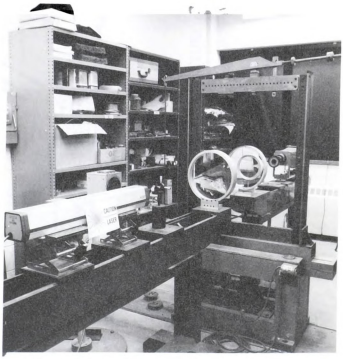

Figure 2.17 Photograph of Fourier data processor setup.

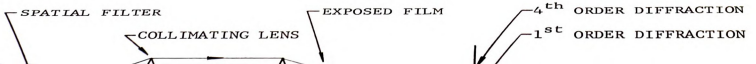
SPATIAL FILTER
COLLIMATING LENS
EXPOSED FILM
4th ORDER DIFFRACTION
1st ORDER DIFFRACTION

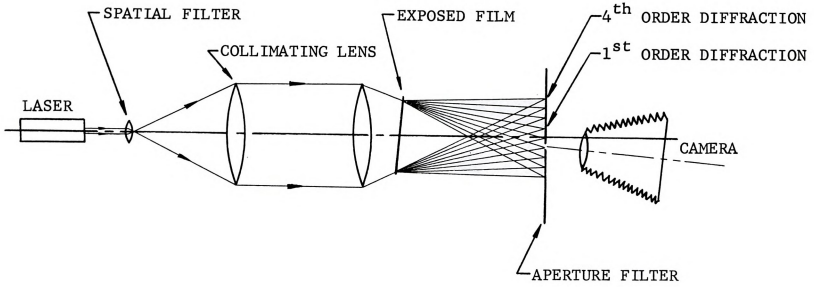

Figure 2.18 Optical system for Fourier data processor.


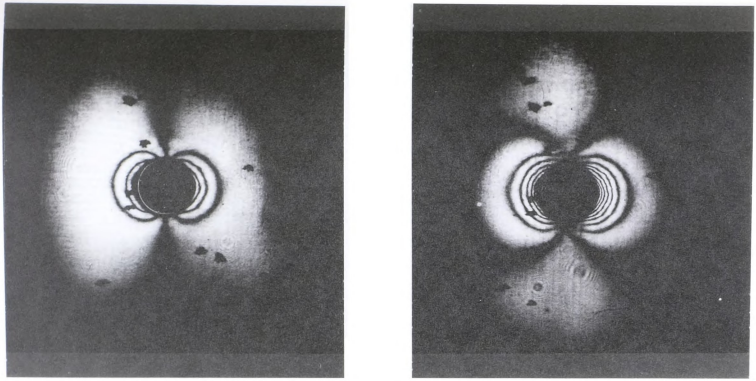

(a) (b)

Figure 2.19 Moiré fringe pattern photographs of the residual strain field around the coldworked hole; (a) first order, (b) second order.


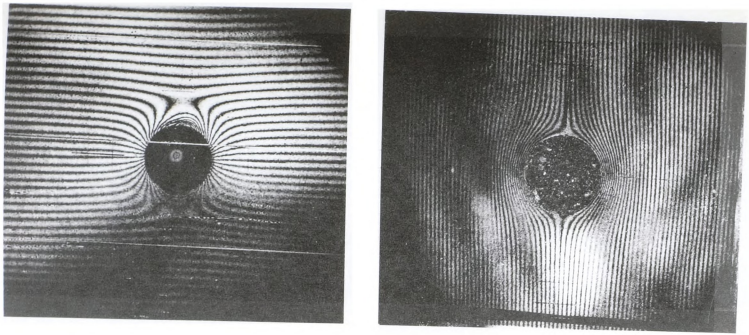

(a) (b)

Figure 2.20 Moiré fringe pattern photographs of the residual strain field around the hole by mismatch technique; (a) tension, (b) compression mismatch.

U is

N is

p is

From the defi

strai

here

but

there

The p

illustrated i

point of inte

was projected

from the moir

up from the b

plotted, defi

at a point gi

be followed t

of these deri

The p

slopes of the

determination

$$U = Np \tag{2.2}$$

U is the x-component of displacement.

N is the moiré fringe order.

p is the pitch distance of master.

From the definition of strain

strain $$\varepsilon_x = \frac{\partial U}{\partial x} \tag{2.3}$$

here $$\varepsilon_x = \frac{\partial (Np)}{\partial x} \tag{2.4}$$

but p = constant

therefore $$\varepsilon_x = p\frac{\partial N}{\partial x} \tag{2.5}$$

The procedure to obtain a partial derivative of U is illustrated in Figure 2.21. The horizontal position of each point of intersection of the moiré fringes with the line AB was projected onto the base line CD. The orders were read from the moiré fringes, and distances equal to Np were scaled up from the base line. A line drawn through the points, thus plotted, defines the displacement. The slope of this curve at a point gives the derivative $\frac{\partial U}{\partial x}$. The same procedure can be followed to obtain other partial derivatives. The values of these derivatives give the strains.

The precision of the graphical computation of the slopes of the displacement curve, which is necessary for the determination of the strains, depends on the number of points

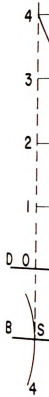

Figure 2.2

defining the
large number
For a given s
grating pitch
alternative p
to have an in
the fringe sp
"mismatch" wi
the moiré pat
undeformed st

The fi
written in the

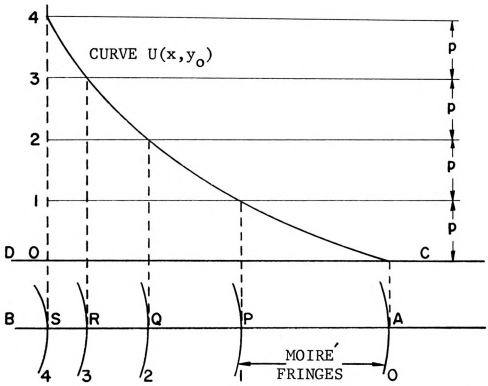

Figure 2.21.--Construction of the intersection curve.

defining the differentiated curve. In the moiré method a large number of points requires a large number of fringes. For a given strain the number of points depended on the grating pitch. If the grid pitch cannot be changed, an alternative procedure to increase the number of points is to have an initial pattern and to work with the change of the fringe spacing. Therefore, the advantages of grid "mismatch" will be discussed when the strains are small and the moiré pattern has been referred to the initial or undeformed state.

The fringe spacing for the pitch mismatch can be written in the form of:

where

δ_m is

p is

ε_m is

For the defor

where

δ_d is

ε_d is

The fringe sp

ε_m and ε_d is

where the plu

minus sign to

To in

This is achie

when $\varepsilon_d\varepsilon_m>0$.

$$\delta_m = \frac{p}{|\varepsilon_m|} \tag{2.6}$$

where

δ_m is the fringe spacing for the initial pitch mismatch.

p is the master-grating pitch.

ε_m is the initial fictitious strain.

For the deformed grating the corresponding fringe spacing is

$$\delta_d = \frac{p}{|\varepsilon_d|} \tag{2.7}$$

where

δ_d is the fringe spacing of deformed grating.

ε_d is the strain produced by the applied deformation.

The fringe spacing resulting (δ_f) from the superposition of ε_m and ε_d is

$$\delta_f = \frac{p}{|\varepsilon_m| \pm |\varepsilon_d|} \tag{2.8}$$

where the plus sign applies to the case $\varepsilon_d\varepsilon_m>0$, and the minus sign to the case $\varepsilon_d\varepsilon_m<0$.

To increase the precision it is desired that

$$\delta_f < \delta_d \tag{2.9}$$

This is achieved by any

$$|\varepsilon_m| > 0 \tag{2.10}$$

when $\varepsilon_d\varepsilon_m>0$.

But when $\varepsilon_d \varepsilon_p$

It is then c
produce more
that a mismat
at least twic

The p
linear strain
the nonlinear
strain(15) sh

The E

The ab
grating; for d
lagrangian for

ε

But when $\varepsilon_d \varepsilon_m < 0$, inequality (Eq. 2.9) is satisfied if

$$|\varepsilon_m| > 2\ |\varepsilon_d| \tag{2.11}$$

It is then clear that a mismatch of the same sign will always produce more fringes and so will always be advantageous; and that a mismatch of opposite sign, to be advantageous, must be at least twice the magnitude of the strain to be analyzed.

The preceding methods will be satisfactory for small linear strain in x and y axes only. For more accurate results, the nonlinear Eulerian and Lagrangian normal strain and shear strain (15) should be used.

The Eulerian formula can be expressed as follows:

$$\varepsilon_x = 1 - \sqrt{1 - 2\frac{\partial u}{\partial x} + \left(\frac{\partial u}{\partial x}\right)^2 + \left(\frac{\partial v}{\partial x}\right)^2} \tag{2.12}$$

$$\varepsilon_y = 1 - \sqrt{1 - 2\frac{\partial v}{\partial y} + \left(\frac{\partial v}{\partial y}\right)^2 + \left(\frac{\partial u}{\partial y}\right)^2} \tag{2.13}$$

$$\varepsilon_{xy} = \arcsin \frac{\frac{\partial u}{\partial y} + \frac{\partial v}{\partial x} - \left(\frac{\partial u}{\partial x}\frac{\partial u}{\partial y} + \frac{\partial v}{\partial x}\frac{\partial v}{\partial y}\right)}{(1-\varepsilon_x)(1-\varepsilon_y)} \tag{2.14}$$

The above equations are used for undeformed specimen rating; for deformed specimen grating one has to apply the agrangian formula displayed below:

$$\varepsilon_x = \sqrt{1 + 2\frac{\partial u}{\partial x} + \left(\frac{\partial u}{\partial x}\right)^2 + \left(\frac{\partial v}{\partial x}\right)^2} - 1 \tag{2.15}$$

Both

cross gratin

patterns at

that can be

which is exp

and

Where N

N_s

$N_{x'}^{x}$

Δu

$\Delta x'$

Δx

Shif

for small st

$$\varepsilon_y = \sqrt{1+2\frac{\partial v}{\partial y} + \left(\frac{\partial v}{\partial y}\right)^2+\left(\frac{\partial u}{\partial y}\right)^2} - 1 \qquad (2.16)$$

$$\varepsilon_{xy} = \arcsin\frac{\frac{\partial u}{\partial y} + \frac{\partial v}{\partial x} + \left(\frac{\partial u}{\partial x}\frac{\partial u}{\partial y} + \frac{\partial v}{\partial x}\frac{\partial v}{\partial y}\right)}{(1+\varepsilon_x)(1+\varepsilon_y)} \qquad (2.17)$$

Both Eulerian and Lagrangian methods require moiré cross grating to obtain u and v families of moiré fringe patterns at the same time. Another method for strain analysis that can be applied to the experiments is a shifting method which is expressed in the following form:

$$\frac{\Delta u}{\Delta x'} = \frac{Np}{\Delta x'} = \frac{N}{N_s} \qquad (2.18)$$

and

$$\frac{\Delta x}{\Delta x'} = \frac{N^x_{x'}}{N_s} \qquad (2.19)$$

$$\varepsilon_x = \frac{\Delta u}{\Delta x} = \frac{N}{N^x_{x'}} \qquad (2.20)$$

where N is the fringe number.

N_s is the shift to pitch ratio.

$N^x_{x'}$ is the moiré line order of shifting.

Δu is the displacement on fringe line.

$\Delta x'$ is the amount of shift.

Δx is the distance between two points of interest.

Shifting method will not produce accurate results for small strains, but it is still good for approximating the

strains. The larger the shift, the more sensitivity will be obtained.

In this experiment, the specimens were loaded in uniaxial tension. Dot gratings were used to measure the transverse strains, but these strains were found to be very small and could be ignored. Therefore only equations 2.2 to 2.11 have been applied to the experimental analysis.

2.3.5 Pitch Error

Basic to all moiré analysis, both for displacement and strain analysis, is the assumption of a constant known value of the pitches of both master and undeformed specimen gratings. From Durelli and Parks (15), if the two pitches are well matched but have a common error of 1 percent, the error occurring in displacement, assuming a density of 1,000 lpi which have been used in this investigation, will be only 0.00001 inch (0.00025 mm) and on a 0.1 inch (2.54 mm) base length the error in strain will be 0.0001.

In the case of mismatch, the pitch of master grating and the pitch of the undeformed specimen grating are different, but each has to be known, and errors in these figures will be reflected directly in any analysis. It is simple to obtain an overall estimate of any mismatch by overlaying master and undeformed specimen gratings and recording the total number of fringes produced in the field.

A serious systematic error will be made by assuming matched pair of grating and neglecting mismatch, since a

mismatch of 0.1 percent will immediately show up as a large strain of 0.001. The chief precaution in moiré analysis for overall variation in pitch (mismatch) is to record any initial fringes before loading and subtract out this "fictitious" displacement and strain in the analysis.

It is estimated that the pitch lines may vary some ±1/100 of the pitch spacing so that the error in pitch of a 1,000 lpi grating will be the order of ±0.00001 inch (0.00025 mm). On the base length of 0.08 inch (2.03 mm) that had been used in the experiments would produce a fictitious strain as great as

$$\varepsilon = \frac{\pm 0.00001}{0.08} = \pm 0.000125.$$

This, however, would require that the error in pitch be repeated over a number of grating lines in the region in order to effect the position of a moiré fringe.

Essentially, this is the problem with periodic pitch error, which repeats itself systematically over a number of grating lines and produces herringbone effects when overlaid by a strain pattern.

2.4 The Interferometric Displacement Gage (IDG) Technique

Interferometry methods have been employed by several investigators (20-22) to obtain the complete crack surface displacement field in the transparent specimens. Examination of the interference fringe patterns obtained for various

loadings revealed that the crack perimeter was closed at zero load. Although the fringe patterns provided a quantitative mapping of the entire crack surface profile, the interior displacement measurements by this method are restricted to transparent materials. In this experiment the surface displacement measurements were measured with an IDG technique developed by Sharpe (22). The method is based on laser interferometry measurements of the in-plane displacement in the vicinity of the crack tip.

In the crack tip displacement method, one measures the displacement at some point near the crack tip as a function of remote load by the laser interferometry method and then computes K from the elastic displacement relation by Paris and Sih (23). For Mode I loading the appropriate equations for conditions of plane stress are:

$$u_x = \frac{K_I}{G}\sqrt{\frac{r}{2\pi}} \cos\frac{\theta}{2}\left[\frac{1-\upsilon}{1+\upsilon} + \sin^2\frac{\theta}{2}\right] \qquad (2.21)$$

$$u_y = \frac{K_I}{G}\sqrt{\frac{r}{2\pi}} \sin\frac{\theta}{2}\left[\frac{2}{1+\upsilon} - \cos^2\frac{\theta}{2}\right] \qquad (2.22)$$

where u_x and u_y are the x and y components of displacement at a point near the crack tip located by the polar coordinator (r,θ) as shown in Figure 2.22.

G is the shear modulus.

υ is the Poisson's ratio.

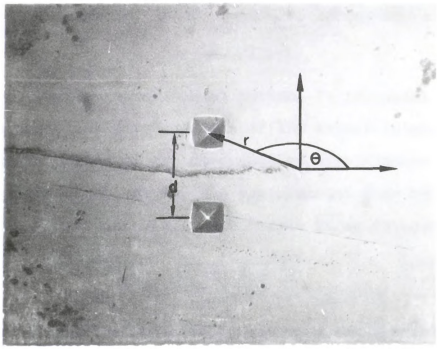

Figure 2.22 Photomicrograph of a fatigue crack defining the crack tip coordinates and showing the surface indentations.

The crack tip displacement method requires a technique capable of measuring small displacements very near the crack tip. As a rule of thumb, the above displacement relations are assumed to be sufficiently accurate within a distance a/20 from the crack tip, where 'a' is the crack length.

The general stress intensity factor equation is:

$$K_I = \sigma\sqrt{\pi a}F(a) \tag{2.23}$$

For the experimental method, it is useful to rearrange the elasticity equation of the stress intensity factor and the equation of the component of displacement into a form more convenient for the experimental data by combining Equations 2.22 and 2.23. The result is as follows:

$$F(a) = \frac{G}{F(\theta)\sqrt{\frac{2}{ra}}}\frac{u_y}{\sigma} \tag{2.24}$$

where $F(\theta)$ is the angle dependent term in Equation 2.22.

The plane stress form for u_y is chosen since all of the displacements are made on the specimen surface.

In addition to presenting F(a) in terms of experimental quantities, Equation 2.24 also enables one to account for local yielding encountered in actual experiments. In particular, plastically deformed material left in the realm of a propagating fatigue crack can cause crack closure (24), the phenomena characterized by an initial nonlinear load-displacement response. Once the opening load (24) is reached, however, behavior is again elastic. Thus, when the slope

$\frac{u_y}{\sigma}$ in Equation 2.24 is taken from the linear portion of the load displacement record following the opening load, an elastic stress intensity factor is obtained.

2.4.1 Basics of the IDG

The principles of the IDG have been described in detail in Reference (22); only a basic review of the technique is given here. Shallow reflective indentations are pressed into the polished surface of the specimen on either side of a crack as shown in Figure 2.22. When coherent light impinges upon the indentations, it is diffracted back at an angle (α_o) with respect to the incident beam shown schematically in Figure 2.23. Since the indentations are placed close together, the respective diffracted beams overlap resulting in interference fringe patterns on either side of the incident laser beam.

In observing the fringe pattern from a fixed position at the angle α_o, fringe movement occurs as the distance 'd' between the indentations changes. Application of a tensile load, causing the distance between the indentations to increase, results in positive fringe motion towards the incident beam. Conversely, the removal of the tensile load results in negative fringe motion away from the incident beam.

The relationship between the indentation spacing and the fringe order shown schematically in Figure 2.23 is:

$$d \sin \alpha_o = m\lambda \qquad (2.25)$$

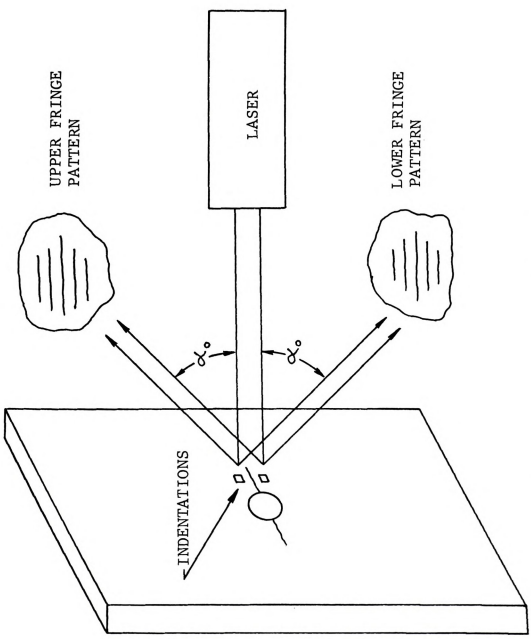

Figure 2.23 Schematic of the IDG.

where m is the fringe order.

d is the spacing between indentations.

λ is the wave length of the incident beam.

α_o is the angle between the incident and reflected beams, thus defining the zeroth fringe order.

The relationship between the change in indentation spacing 'δd' and the change in fringe order at the fixed observation point 'δm' is given by:

$$\delta d = \frac{\delta m \lambda}{\sin \alpha_o} \tag{2.26}$$

It is this relation that serves as the basis of the IDG.

Fringe motion can be caused by rigid body motion as well as relative displacement. When the specimen moves parallel to its surface and along a line between the indentations (i.e., vertically in Figure 2.23), one fringe pattern moves toward the incident beam, and one moves away. Therefore, averaging the fringe motions eliminates the rigid body motion, and one should calculate the displacement from:

$$\delta d = \frac{\lambda}{\sin \alpha_o} \quad \frac{\delta m_1 + \delta m_2}{2} \tag{2.27}$$

This component of rigid-body motion is present in every ordinary system for loading specimens, so that it is very important that it be averaged out. Other rigid-body motions (i.e., one perpendicular to the specimen surface) are not averaged out and can lead to errors. In a carefully aligned

testing machine these components of rigid-body motion can be made small, eliminating the need for corrections.

Using typical values of λ = 0.6328 micron (He-Ne laser) and α_o = 42°, the calibration constant $\lambda/\sin\alpha_o$ is 0.95 micron. In other words, when one complete fringe shift has been observed, the corresponding displacement is about one micron. An electro-optical recording system that simply counts the fringes of one pattern as they pass will have a resolution of one micron. A recording system that counts both patterns and increments the output voltage whenever either pattern moves one fringe will have a resolution of one-half micron.

The "gage" consists of the two reflecting indentations that are applied with a Vicker's hardness tester using the 100 p weight. The diamond indentor in the tester permits the accurate location and application of high quantity pyramidal indentations. One can locate the indentations within ±2 microns if care is taken. These indentations are typically 25 microns long on each side. A typical application of the indentations that were used in this experiment are shown in Figure 2.22 where x = -50 microns and d = 50 microns. The corresponding fringe pattern is shown in Figure 2.24. After application of the indentations r and θ were measured with the ocular scale of the microhardness tester, to locate the gage points with respect to the crack tip.

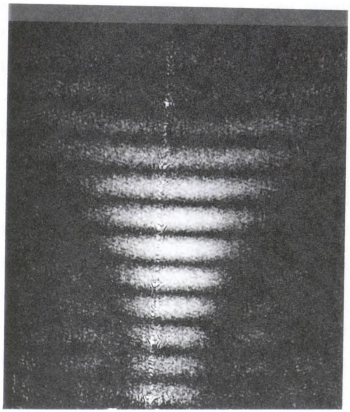

Figure 2.24 Typical interference fringe pattern.

2.4.2 Displacement Measuring Instrument

Two phototransistors type 2N5777 were used for uni-axial displacement measurement in this investigation; they were mounted on microscope translation stages which were attached to a two-armed frame, and placed approximately 17 cm from a pair of indentations on the specimen. Both photo-transistors were connected to a fringe counting unit to allow monitoring of the fringe motion and to provide a d-c voltage output. The d-c output of the fringe counting unit was used to drive a x-y recorder.

The light source utilized for this work was a Spectra Physics Model 120, 5-mW HeNe laser. The two-armed frame and the laser were mounted on the same tripod; relative motion or vibration was no problem (see Figure 2.25).

The instrument and its operating procedures are described in a forthcoming report on NASA grant NSG 3101.

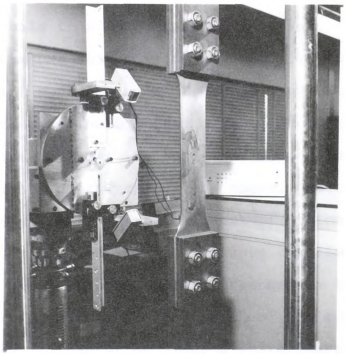

Figure 2.25 The equipment used for the IDG technique.

CHAPTER 3

RESIDUAL STRAINS AROUND COLDWORKED HOLES

3.1 Overview

Several theoretical solutions exist for the problem of an expanded hole in a thin sheet of material. All of these theories assume that the hole is radially loaded so that the material near the hole is loaded above its yield stress. Some theories assume that a state of plane strain exists everywhere in the thick sheet and some theories assume plane stress exists everywhere in the sheet. Most of them assume that the sheet is infinite in extent. Aluminum sheet, 1/8 inch (0.320 mm) thick is used in these experiments, and one can assume plane stress exists everywhere in the sheet.

A small (compared with the width of the specimen) circular hole in the center provides a state nearly the same as an infinite plate. Therefore the analytical formulas for the infinite plate may be used for a solution of this finite width specimen with a small circular hole.

After the loading is removed, most theories assume that the material unloads elastically with no reverse yielding at the hole edge. Some solutions, such as Hsu-Forman (2) take into account the effect of workhardening during loading. For the aluminum 7075-T6 specimen, the effect of this workhardening during loading is very small according to Manson

(25) and may be negligible. The Potter-Ting-Grandt (3,4) theory has a limit on the allowable radial displacement of 0.0037 inch (0.094 mm) for the 3/16 inch (4.760 mm) hole. So the 0.0040 inch (0.102 mm) and 0.0060 inch (0.152 mm) radial expansion of the experiments is not permitted.

The geometrical shape being studied analytically is a flat circular sheet of radius "b" with a circular hole of radius "a" in the center (see Figure 3.1). Most theories that have been developed assume "b" to be infinitely large and the thickness of the sheet sufficiently small relative to dimension "b" so that a condition of plane stress exists. Deformation of the sheet is caused by either a uniform positive radial displacement, u_a, or a uniform negative pressure, -p, at r = a.

The problem is symmetric about the Z-axis because of the radial loading, so the strains are given by

$$\varepsilon_r = \frac{\partial u}{\partial r} \; ; \; \varepsilon_\theta = \frac{u}{r} \tag{3.1}$$

where u is the radial displacement of the material. The equilibrium equation, which must hold for either elastic or plastic stresses, is:

$$\frac{d\sigma_r}{dr} + \frac{\sigma_r - \sigma_\theta}{r} = 0 \tag{3.2}$$

For a radial displacement, u_a, small enough that the material remains <u>elastic</u> everywhere, the stresses, strains,

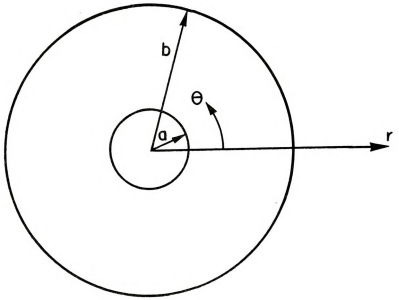

Figure 3.1 Geometry and coordinate system used in coldworked hole theories.

and displacements are given by Little (26):

$$\sigma_r = A[-\frac{1}{r^2} + \frac{1}{b^2}], \quad \sigma_\theta = A[\frac{1}{r^2} + \frac{1}{b^2}] \tag{3.3}$$

$$\varepsilon_r = \frac{A}{E}[-\frac{1+\upsilon}{r^2} + \frac{1-\upsilon}{b^2}], \varepsilon_\theta = \frac{A}{E}[\frac{1+\upsilon}{r^2} + \frac{1-\upsilon}{b^2}] \tag{3.4}$$

$$u = \frac{A}{E}[\frac{1+\upsilon}{r} + \frac{(1-\upsilon)r}{b^2}] \tag{3.5}$$

$$A = \frac{Eu_a}{\frac{1+\upsilon}{a} + (1-\upsilon)\frac{a}{b^2}} \tag{3.6}$$

where E and υ are the modulus of elasticity and Poisson's ratio. The boundary conditions here are that $\sigma_r = 0$ at $r = b$ and $u = u_a$ at $r = a$.

The Mises-Hencky yield criterion becomes:

$$\sigma_r^2 + \sigma_\theta^2 - \sigma_r\sigma_\theta = \sigma_{ys}^2 \tag{3.7}$$

where σ_{ys} is the yield stress from the uniaxial stress-strain curve.

The largest radial displacement that can be applied to the hole without causing plastic deformation is:

$$u_{aE} = \frac{\sigma_{ys}}{E[\frac{1}{b^4} + \frac{3}{a^4}]^{\frac{1}{2}}}\ [\frac{1+\upsilon}{a} + \frac{(1-\upsilon)a}{b^2}] \tag{3.8}$$

Once u_{aE} (or its equivalent pressure, p_E) is exceeded, the material in the neighborhood of "a" becomes plastically deformed and the solution of the problem is no longer easy. Denote the interface between the elastic region and the plastic region by r_p. As u_a increases, r_p increases; i.e., the elastic-plastic boundary moves out into the material. The problem in the plastic region to be solved is now one in which $u = u_a$ at $r = a$ (or $\sigma_r = -p$ at $r = a$) and the stresses, strains, and displacements match the elastic ones at $r = r_p$. If r_p is known, these elastic stresses, etc., are easily calculated because it is known that, if $b \to \infty$, $\sigma_r = -\sigma_\theta$, and therefore from equation 3.7:

$$\sigma_r|_{r_p} = \frac{-\sigma_{ys}}{\sqrt{3}} = -\sigma_\theta|_{r_p} \tag{3.9}$$

In the elastic region, $r > r_p$:

$$\sigma_r = -\frac{\sigma_{ys}}{\sqrt{3}} \left(\frac{r_p}{r}\right)^2, \quad \sigma_\theta = \frac{\sigma_{ys}}{\sqrt{3}} \left(\frac{r_p}{r}\right)^2 \tag{3.10}$$

$$\varepsilon_r = -\frac{\sigma_{ys}(1+\upsilon)}{E\sqrt{3}} \left(\frac{r_p}{r}\right)^2, \quad \varepsilon_\theta = \frac{\sigma_{ys}(1+\upsilon)}{E\sqrt{3}} \left(\frac{r_p}{r}\right)^2 \tag{3.11}$$

$$u = \frac{\sigma_{ys}(1+\upsilon)}{E\sqrt{3}} \frac{r_p^2}{r} \tag{3.12}$$

The problem in plasticity theory is then to find the stresses, etc., subject to the known boundary condition at $r = a$ and $r = r_p$. An important part of the problem is the

determination of the relation between loading and r_p. Various theories have been developed to predict these quantities, and they fall into three classes: analytical, numerical, and finite-element. The analytical theories produce closed-form equations based on either an elastic-perfectly-plastic stress-strain curve or a two-parameter plastic stress-strain curve. The numerical ones develop the solution in terms of incremental rings between a and b corresponding to increments on the plastic stress-strain curve. The one finite element solution uses an elastic-plastic computer code.

Once the hole has been expanded to the prescribed conditions, the loading is removed at r = a. This generates, because of the elastic relaxation of material outside (and inside) r_p, residual stresses. The analytical and numerical theories (except for (4)) represents this unloading by superposing an elastic stress field:

$$\sigma_r = \sigma_m \left(\frac{a}{r}\right)^2, \quad \sigma_\theta = -\sigma_m \left(\frac{a}{r}\right)^2 \tag{3.13}$$

where σ_m is the magnitude of the radial stress generated at r = a by the loading process. This guarantees that $\sigma_r = 0$ at r = a after unloading.

Four theories are discussed in the following sections and compared in the results section. In each case the residual stresses and strains for 7075-T6 aluminum subjected to: u_a = 0.0040 inch (0.102 mm) and 0.0060 inch (0.152 mm) at a = 0.0980 inch (2.490 mm) are calculated.

3.2 Nadai Theory

Nadai (1) in 1943 published a theory on plastic expansion of tubes fitted into boilers. The plate of the boiler has a tube fitted into it and in the manufacturing process these tubes were expanded by a rolling process to insure a leak-free fit. He considered both the plastic deformation in the steel plate and the plastic deformation of the copper alloy tubes. He first solved the plate problem, which is the one of interest here. His assumptions were:

1) Uniform pressure at the edge of the hole in the plate.

2) A linear approximation to the Mises-Hencky yield criterion.

3) Perfectly plastic material response.

In the plastic zone he develops the following equations:

$$\sigma_r = \frac{\sigma_{ys}}{\sqrt{3}}\left(-1 + 2 \ln \frac{r}{r_p}\right) \tag{3.14}$$

$$\sigma_\theta = \frac{\sigma_{ys}}{\sqrt{3}}\left(1 + 2 \ln \frac{r}{r_p}\right) \tag{3.15}$$

$$u = \left(\frac{3}{2}\right)^3 \frac{u_a E \frac{r}{a}}{\left(\frac{3}{2} + \ln \frac{r}{r_p}\right)^3} \tag{3.16}$$

where r_p is the radius of the plastic zone;

r is the radial distance of the calculated point from the center;

a is the outer radius of the tube.

The residual stresses and strains after relaxation are plotted and compared with Hsu-Forman theory in Figures 3.2, 3.3, 3.4 and 3.5. For the test case of 0.0040 inch (0.102 mm) and 0.0060 inch (0.152 mm) radial expansion, the theory computes $r_p = 2.069a$ and $r_p = 2.281a$ respectively.

He also developed the theory for the stresses in a tube with a general stress-strain curve. This complete theory could be applied to coldworking procedures in which the sleeve remains in the hole. Nadai formulated the problem in terms of the Mises-Hencky criterion, but he linearized this criterion to obtain a closed-form solution.

3.3 Hsu-Forman Theory

The Hsu-Forman theory (2) of 1975 is basically the Nadai theory extended to account for workhardening. Their solution is based on J_2 deformation theory together with a modified Ramberg-Osgood law. The sheet is orthotropic in the thickness dissection but isotropic in its plane. Only small displacements are considered. The change in hole size and the variation of the sheet thickness are neglected. The assumptions are:

1) Uniform pressure at the hole.

2) Mises-Hencky yield criterion.

3) Ramberg-Osgood representation of stress-strain curve.

The material behavior is represented by

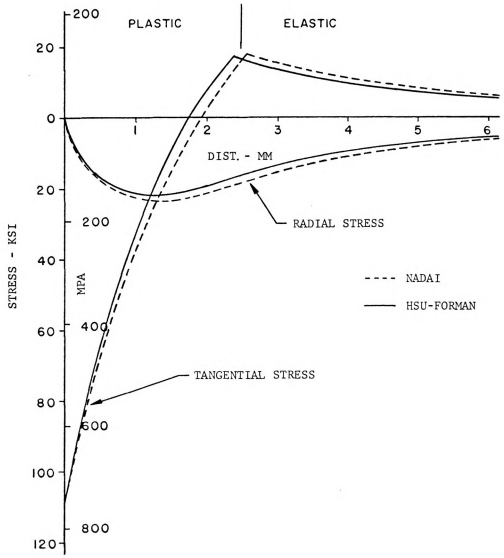

Figure 3.2 Residual stresses after coldworking for 0.0040 inch (0.102 mm) radial expansion.

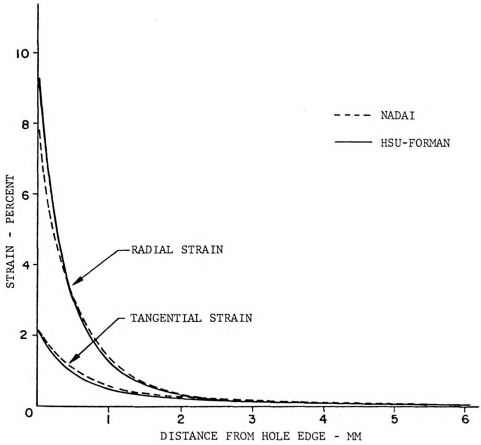

Figure 3.3 Residual strains after coldworking for 0.0040 inch (0.102 mm) radial expansion.

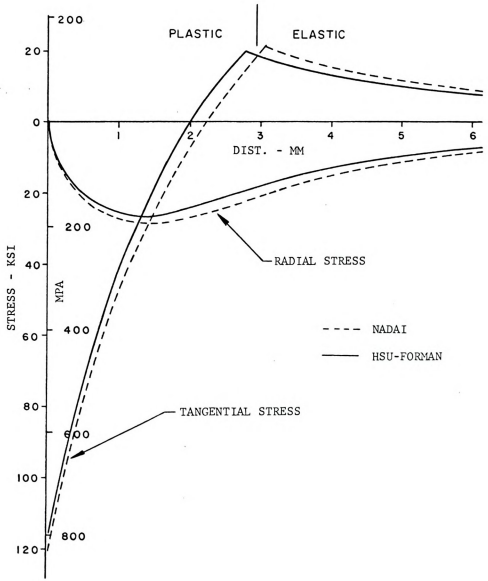

Figure 3.4 Residual stresses after coldworking for 0.0060 inch (0.152 mm) radial expansion.

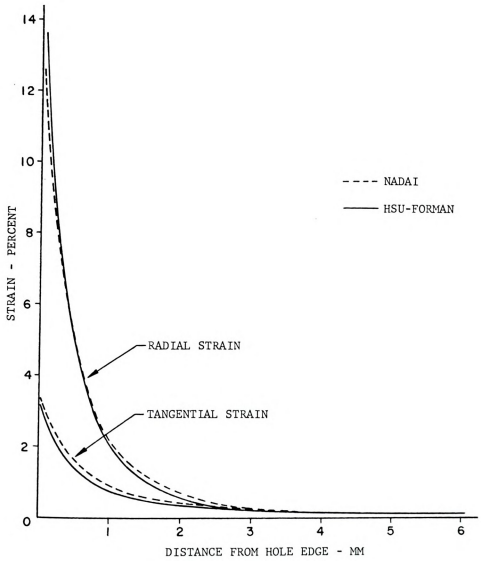

Figure 3.5 Residual strains after coldworking for 0.0060 inch (0.152 mm) radial expansion.

$$\varepsilon = \frac{\sigma}{E} \text{ for } |\sigma| \leq \sigma_{ys}$$

$$\varepsilon = \frac{\sigma}{E}\left|\frac{\sigma}{\sigma_{ys}}\right|^{n-1} \text{ for } |\sigma| \geq \sigma_{ys} \tag{3.17}$$

The test material of 7075-T6 aluminum is adequately represented by n = 15, σ_{ys} = 73 Ksi (504 MPa). The solution is developed in terms of a parameter α which varies between 90° and α_a, where α_a corresponds to a radial expansion u_a which is known by measurement.

In our case, α_a is equal to 133.3° for 0.0040 inch (0.102 mm) and 137.0° for 0.0060 inch (0.152 mm) radial expansion. For each case of radial expansion, the elastic-plastic boundaries are found at r_p = 1.98a and r_p = 2.15 a. The stresses and strains are also plotted and compared with Nadai theory in Figures 3.2, 3.3, 3.4 and 3.5.

3.4 Potter-Ting-Grandt Theory

Potter and Grandt (4) applied the general solution of Potter and Ting (3) to the coldworked holes solution with an eye towards making it useful to designers. Their assumptions were:

1) Uniform radial displacement at the hole.

2) Mises-Hencky yield criterion.

3) Elastic-plastic material response.

Their work is similar to the earlier work of Nadai (1), except that they did not use a linearized yield criterion.

The Potter-Grandt theory has limits to allow the radial displacement. For the 7075-T6 aluminum and specimen dimension used in this investigation, the maximum radial displacement is 0.0037 inch (.094 mm), so the 0.0040 inch (0.102 mm) and 0.0060 inch (0.152 mm) radial expansion of the experiments are not permitted.

3.5 Adler-Dupree Solution

Adler-Dupree (12) performed an elastic-plastic finite element analysis of the two-dimensional stress field around a coldworked hole. They assumed plane stress and accounted for plastic behavior of the material by a Ramberg-Osgood formulation relates the equivalent plastic strain to the n^{th} power of the equivalent stress. The radially symmetric finite element mesh was made up of quadrilateral elements divided into two layers with two triangular elements in each layer. The specific problem they considered was a 0.006 inch (0.15 mm) radial expansion of a 0.260 inch (6.60 mm) hole in 7075-T6 aluminum and then removal of that expansion (the same as our test case). This models the coldworking process of J. O. King, Inc., in which an oversized tapered mandrel is pulled completely through a hole. The closest they could get to the hole edge for their computation was 0.025 inch (0.64 mm).

Because of the limited radial expansion and the hole size of this solution, it was only used to compare with the

experimental data for the 1/4 inch (6.4 mm) thick specimen in the next section.

3.6 Experimental Results

In this section the results of residual strains generated by coldworking are reported. Almost all of the specimens are 1/8 inch (3.2 mm) in thickness and have dimensions as shown in Figure 2.3. One specimen is 1/4 inch (6.4 mm) thick and has rectangular dimensions of 2.5 inches (6.4 cm) by 3 inches (7.6 cm), the hole is 0.260 inch (6.604 mm). The hole was radially expanded by 0.0035 inch (0.089 mm). The 1/4 inch (6.4 mm) thick specimen was tested to obtain the residual strains for comparison with the indentation technique by Sharpe (13) and the finite element method by Adler and Dupree (12).

In the specimen with the thickness of 1/8 inch (3.2 mm), the holes are 0.195 inch (4.95 mm). The holes were radially expanded by 0.0040 inch (0.102 mm) and 0.0060 inch (0.152 mm) then unloaded.

3.6.1 1/4 Inch Thick Specimen

Residual radial and tangential strains measured by moiré are plotted to compare with the indentation procedure in Figure 3.6. Note that this specimen had been tested at the beginning of this research, therefore, one cannot make measurements right up to the edge of the hole because of lack of resolution of the fringes; the radial strain was

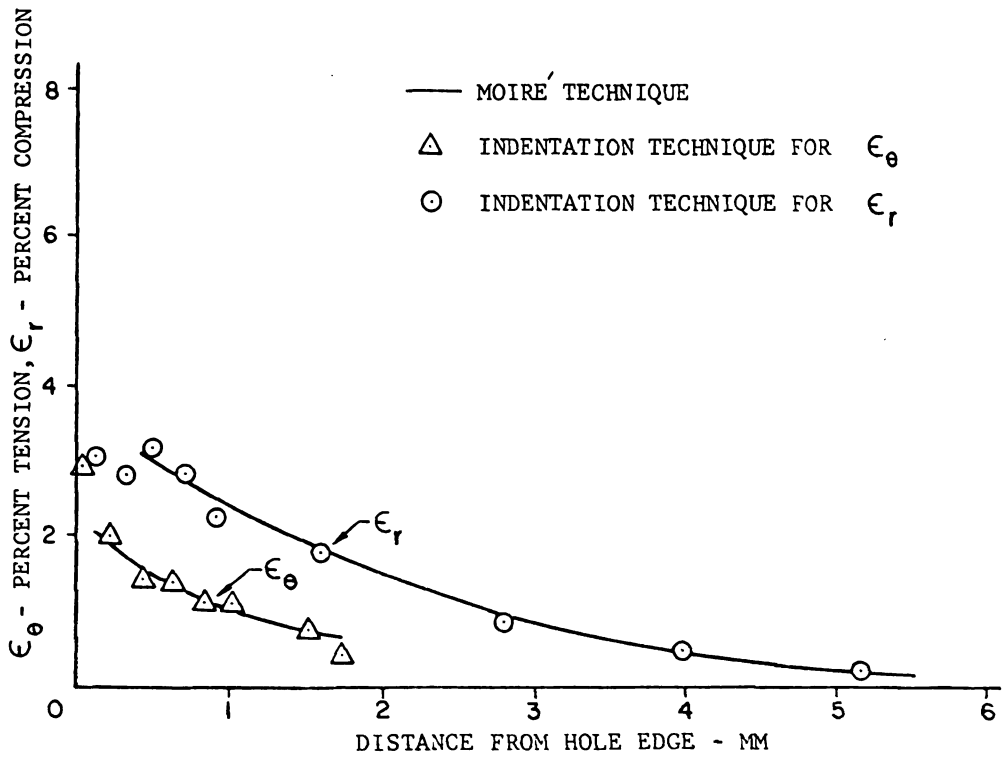

Figure 3.6 Residual strains measured by the moire' technique for the 1/4 inch (6.4 mm) specimen LL. Diametral expansion of the originally 0.261 inch (7.63 mm) hole was only 0.0069 inch (0.175 mm).

measured only to within 0.5 mm in Figure 3.6. The problem was that the printed grille tended to crack in the regions of high plastic deformation at the distance of about 1 mm from the edge of the hole, causing lack of definition there. This problem was solved later by curing the coating at an elevated temperature before coldworking. To assure that the moiré technique was giving the correct results, strain was also measured on the specimen by the indentation procedure. The indentations were applied, the grid printed, moiré measurements made, and then the grid dissolved off the specimen and final strain measurements made. The agreement between the strains is excellent, as shown in Figure 3.6.

One of the great advantages of the moiré technique is that it produces whole field strains. A whole field strain measurement (for one quadrant) is shown in Figure 3.7. This gives the strain in terms of ε_x and ε_y instead of the ε_r and ε_θ that are more conveniently used for theoretical analysis. The predicted strain field of Adler and Dupree (12) is also plotted in Figure 3.7. They used the finite element method and predicted a residual diametral expansion of 0.008 inch (6.2 mm), so the experiment and theory are not exactly the same (0.0069 inch versus 0.008 inch expansion), but the strains agree reasonably well.

3.6.2 1/8 Inch Thick Specimen with 0.004 Inch Radial Expansion

The average residual strain measurements (two on each specimen) from four specimens were obtained by the

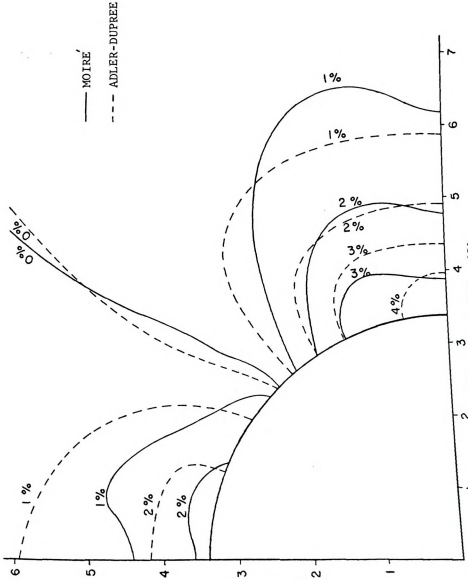

Figure 3.7 Whole-field moiré measurement of the residual strain of specimen LL compared with predictions of Adler-Dupree.

moiré technique then plotted and compared with the theories by Nadai (1) and by Hsu and Forman (2) in Figure 3.8. The vertical bars are the standard deviation of the strains at the points determined in the specimens. The size of the maximum deviation is 0.65% for the large strains near the hole; the average deviation is 0.18%. The specimen holes were originally 0.1960 inch (4.98 mm) to 0.1996 inch (5.07 mm) in diameter and were subjected to the standard cold-working procedures. Using the different sizes of the mandrel, 0.188 inch (4.78 mm) diameter for the 0.1960 inch (4.98 mm) hole and 0.192 inch (4.88 mm) diameter for the 0.1996 inch (5.07 mm) hole, the required radial displacement was obtained as shown in Table 2.3. The radial displacements were measured on the front, and the value varied from the maximum 0.0040 inch (0.102 mm) to the minimum 0.0035 inch (0.089 mm).

Figure 3.8 shows the maximum average radial strain to be 8.3 percent at the distance about 0.16 mm (0.0063 inch) from the hole edge, and Figure 3.9 shows the maximum average tangential strain to be 3.12 percent at the distance about 0.10 mm (0.0039 inch) from the hole edge.

The experimental results of radial and tangential strains are higher than the theories by Nadai (1) and by Hus and Forman (2). Note that Nadai's theory is for perfectly plastic material and the Hsu and Forman theory is basically the Nadai theory extended to account for work-hardening.

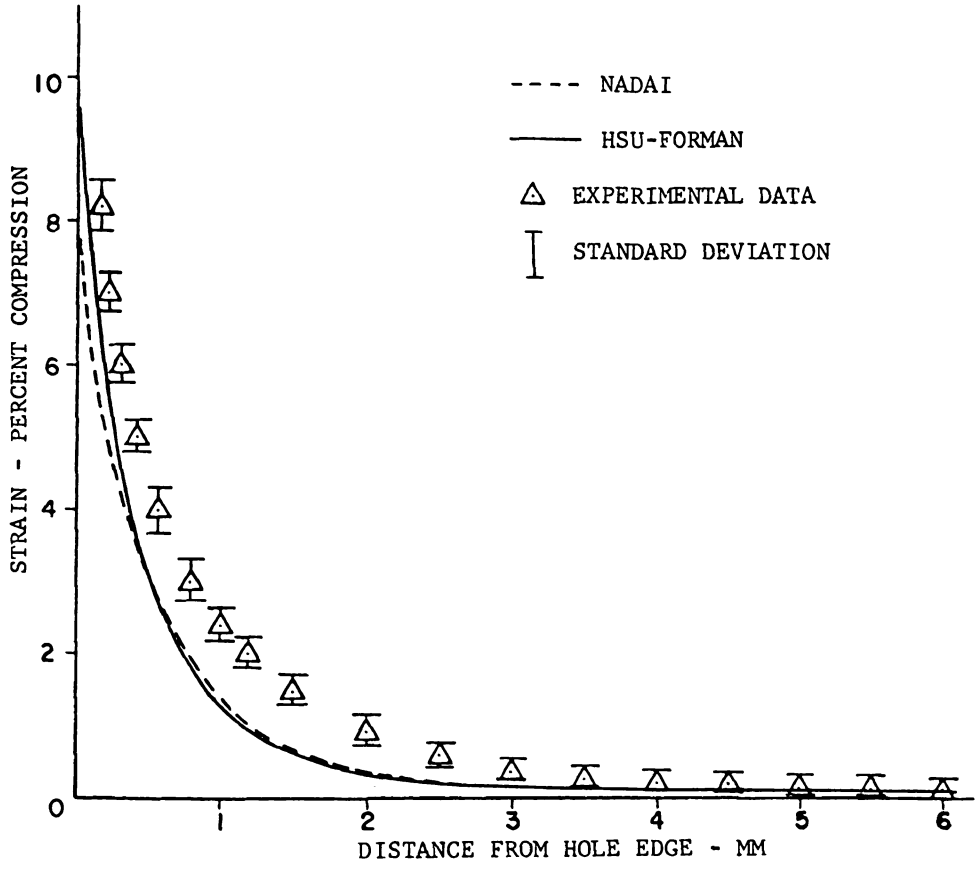

Figure 3.8 Comparison of residual radial strain of 0.0040 inch (0.102 mm) radial expansion with the theories.

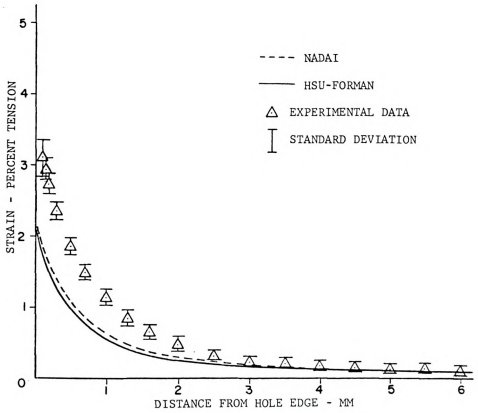

Figure 3.9 Comparison of residual tangential strain of 0.0040 inch (0.102 mm) radial expansion with the theories.

3.6.3 1/8 Inch Thick Specimen with 0.006 Inch Radial Expansion

Residual strain measurements (two on each specimen) of 0.0060 inch (0.152 mm) radial expansion which were performed on four specimens are also plotted and compared with the Nadai and Hsu-Forman theories in Figures 3.10 and 3.11. The size of the maximum deviation is 1.5% and the average deviation 0.2%. The original hole diameters in these specimens were slightly different in size, being from 0.1956 inch (4.968 mm) to 0.1958 inch (4.973 mm). Using the mandrel of 0.192 inch (4.88 mm) diameter, one could obtain the residual radial expansions which varied from 0.0061 inch (0.155 mm) to 0.0052 inch (0.132 mm).

The maximum average radial strain for this amount of coldworking is 10.4 percent at a distance of about 0.17 mm (0.0067 inch) from the hole edge, and the maximum average tangential strain is 4.6 percent at a distance about 0.10 mm from the hole edge.

Figures 3.10 and 3.11 compare the theories and the experiments. Note that the experimental results for both radial and tangential strains are still higher than theories by Nadai (1) and Hsu-Forman (2) as the results in the 0.004 inch (0.102 mm) radial expansion showed.

3.7 Discussion of Results

The experimental results do not quite agree with the theories. The residual radial strain and the residual tangential strain are always larger than the theories at the

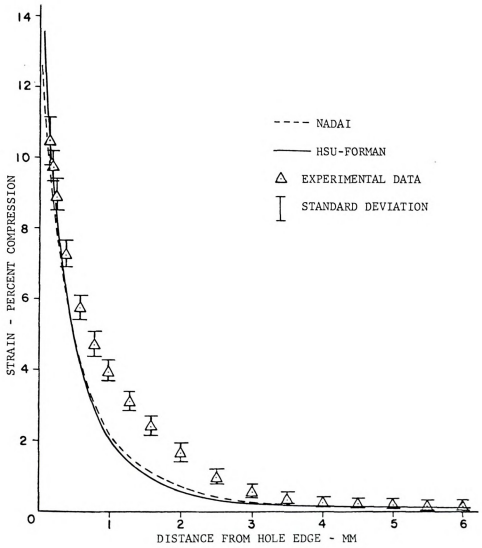

Figure 3.10 Comparison of residual radial strain of 0.0060 inch (0.152 mm) radial expansion with the theories.

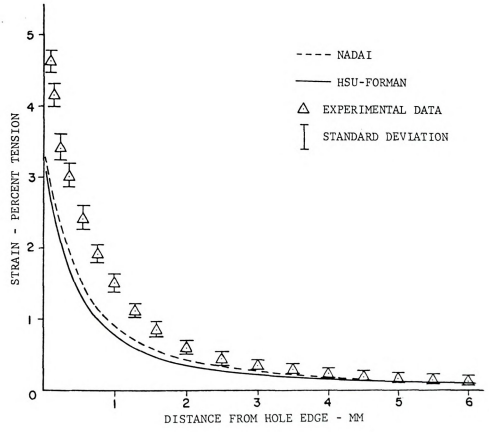

Figure 3.11 Comparison of residual tangential strain of 0.0060 inch (0.152 mm) radial expansion with the theories.

region of interest near the hole edge. The nature of cold-work by pulling a mandrel through the hole was described by Sharpe (13). His results from the indentation technique showed that the strains were larger than the theories in the area close to the hole edge. Also by his measurement, the strains were found to be larger on the front face than on the back face. The experimental strains in this investigation agree well with Sharpe's results. This particular coldworking process produces very nonhomogeneous deformation. Such deformation will vary through the specimen thickness; therefore, the real experimental conditions are not the same as the conditions that the theories assume.

CHAPTER 4

CRACK INITIATION

In this chapter, the strain prior to fatigue crack nucleation, the strain when the crack initiated, and also the number of cycles required to initiate a crack were investigated.

In general, there have been a number of theories proposed for crack initiation; some theories (i.e., 5, 27) are based on the results of a broadening of a slip band which ultimately produces a crack spreading from crystal to crystal; some theories (28-30) are based on the exhaustion of ductility by stresses being raised to some critical level during cyclic loading. Other viewpoints of crack initiation are common among many investigators; crack nucleation at inclusions as well as grain boundaries and at precipitation zones (31) have been two such viewpoints. More recently the idea of fatigue failure involving nucleation of grain boundary voids by interaction between moving dislocation and stationary obstacles, with subsequent void growth by vacancy diffusion was proposed (5). Cracks originating from slip bands formed by slip in crystal planes of preferred orientation is the most commonly accepted of all the nucleation mechanisms (32).

The initiation of a crack for a circular notched specimen is based on the theoretical stress concentration factor that has been discussed by several authors (33-37). Characteristically, fatigue failure in service initiates at geometric discontinuities that produce local stresses higher than the nominal stress applied. In weight-critical applications, these local stresses may be in the plastic range instead of the elastic range.

4.1 Local Strain Behavior Before and at the Initiation of Crack

The theoretical maximum value of the stress concentration factor at the edge of a circular hole in a straight tension member of infinite width is three times the applied uniform stress. This value is approximately correct whenever the plate width is four or more times the hole diameter. Timoshenko-Goodier (6) concurs with this opinion if the width is five or more times the diameter. Since the ratio of plate width to hole diameter is ten for the test specimens, a theoretical stress concentration factor of 3.00 can be accepted.

The elastic solution of local stresses for infinite plates, in the limiting case of plane stress is (6):

$$\sigma_r = \frac{s}{2}[1 - \frac{a^2}{r^2}] + \frac{s}{2}[1 + \frac{3a^4}{r^4} - \frac{4a^2}{r^2}]\cos 2\theta \qquad (4.1)$$

$$\sigma_\theta = \frac{s}{2}[1 + \frac{a^2}{r^2}] - \frac{s}{2}[1 + \frac{3a^4}{r^4}]\cos 2\theta \qquad (4.2)$$

$$\sigma_{r\theta} = \frac{s}{2}[1 - \frac{3a^4}{r^4} + \frac{2a^2}{r^2}] \qquad (4.3)$$

where s is the applied stress,

σ is the local stress,

a is the radius of the hole, and

r is the radius of the point determined.

For this investigation, one must consider the tangential stress σ_θ and the radial stress σ_r to determine the corresponding strain ε_θ by using elastic stress-strain relationship along the line $\theta = 90°$.

For the finite plate, the Howland solution (7) should be used to obtain more accurate results.

$$\sigma_r = s[\tfrac{1}{2}(1-\cos 2\theta) + 2m_o - \frac{d_o}{\rho^2} - 2\sum_{n=1}^{\infty}\{\frac{n(2n+1)d_{2n}}{\rho^{2n+2}} + \frac{(n+1)(2n-1)e_{2n}}{\rho^{2n}} + n(2n-1)l_{2n}\rho^{2n-2} + (n-1)(2n+1)m_{2n}\rho^{2n}\}\cos 2n\theta] \tag{4.4}$$

$$\sigma_\theta = s[\tfrac{1}{2}(1+\cos 2\theta) + 2m_o + \frac{d_o}{\rho^2} + 2\sum_{n=1}^{\infty}\{\frac{n(2n+1)d_{2n}}{\rho^{2n+2}} + \frac{(n-1)(2n-1)e_{2n}}{\rho^{2n}} + n(2n-1)l_{2n}\rho^{2n-2} + (n+1)(2n+1)m_{2n}\rho^{2n}\}\cos 2n\theta] \tag{4.5}$$

$$\sigma_{r\theta} = s[\tfrac{1}{2}\sin 2\theta + 2\sum_{n=1}^{\infty}\{n(2n-1)(l_{2n}\rho^{2n-2} - \frac{e_{2n}}{\rho^{2n}}) + n(2n+1)(m_{2n}\rho^{2n} - \frac{d_{2n}}{\rho^{2n+2}})\}\sin 2n\theta] \tag{4.6}$$

For this experiment, $\lambda = \frac{a}{b} = 0.1$. The coefficients d, e, l, and m will have the values as in Table 4.1.

TABLE 4.1.--Coefficients of the stress function.

$d_o = 5.01 \times 10^{-3}$	———	$l_2 = 4.13 \times 10^{-3}$	$m_o = 5.69 \times 10^{-4}$
$d_2 = 2.54 \times 10^{-5}$	$e_2 = -5.08 \times 10^{-3}$	$l_4 = 1.06 \times 10^{-3}$	$m_2 = -1.13 \times 10^{-3}$
$d_4 = 3.15 \times 10^{-11}$	$e_4 = -4.21 \times 10^{-9}$	$l_6 = 2.83 \times 10^{-4}$	$m_4 = -5.95 \times 10^{-4}$
$d_6 = 1.40 \times 10^{-15}$	$e_6 = -1.68 \times 10^{-13}$	$l_8 = 7.24 \times 10^{-5}$	$m_6 = -2.28 \times 10^{-4}$
$d_8 = 5.00 \times 10^{-20}$	$e_8 = -5.72 \times 10^{-18}$	$l_{10} = 1.82 \times 10^{-5}$	$m_8 = -7.65 \times 10^{-5}$
		$l_{12} = 4.65 \times 10^{-6}$	$m_{10} = -2.39 \times 10^{-5}$
		$l_{14} = 1.15 \times 10^{-6}$	$m_{12} = -7.30 \times 10^{-6}$

where a is the hole radius

b is the specimen width, and

ρ is the proportion of r over b.

For 'a' equal to 'b' and angle $\theta = 90°$, the value of the function of local stress to applied stress equals 3.03. This value is close to the value for the equation of an infinite plate as discussed before.

In fact, the ultimate success or failure of a structure depends on the very localized behavior at its notches and the stresses which become plastic at the area close to the hole before a propagating crack starts.

The theory of plasticity to predict the stress and strain concentration factor of a circular hole in a large, wide sheet specimen in tension was originated by Neuber (8)

and later modified by Stowell (9). An experimental study was performed by Griffith (38). Their results showed that, as the amount of plastic flow increased, the stress concentration factor is appreciably reduced, and the strain concentration factor is appreciably increased.

In order to introduce plasticity into the predicted strain distribution Neuber's rule (8) is applied:

$$K_t = (K_\sigma K_\varepsilon)^{\frac{1}{2}} \tag{4.7}$$

where K_t is the theoretical concentration factor,

K_σ is the stress concentration factor, and

K_ε is the strain concentration factor.

Now, consider a notched specimen subjected to nominal cyclic stress and strain ranges of Δs and Δe respectively. Let the local stress and strain ranges at the notch root be $\Delta\sigma_\theta$ and $\Delta\varepsilon_\theta$. Substituting these quantities in Equation 4.7 we get,

$$K_t = \left(\frac{\Delta\sigma_\theta}{\Delta s} \cdot \frac{\Delta\varepsilon_\theta}{\Delta e}\right)^{\frac{1}{2}} \tag{4.8}$$

or

$$\Delta\varepsilon_\theta = \frac{K_t^2 \Delta s \Delta e}{\Delta\sigma_\theta} \tag{4.9}$$

which can be written as:

$$K_t(\Delta s \Delta e E)^{\frac{1}{2}} = (\Delta\sigma_\theta \Delta\varepsilon_\theta E)^{\frac{1}{2}} \tag{4.10}$$

where E is the modulus of elasticity.

Equation 4.10 is an identity in nominal and actual stress and strain values. Duplicating a quantity equivalent to the R.H.S. in a smooth specimen is the same as reproducing

the deformation behavior at the notch root. The equivalence of the L.H.S. and the R.H.S. implies that when the value $(\Delta\sigma_\theta \Delta\varepsilon_\theta E)^{\frac{1}{2}}$ in a smooth specimen is equivalent to $K_t(\Delta s \Delta e E)^{\frac{1}{2}}$ of a notched member, then the root of this notch is subjected to the same stress and strain conditions as the smooth specimen. Thus, the fatigue life of the notch root and the smooth specimen must be the same, when the size effect in the notched member is taken into consideration.

In fatigue application, the fatigue notch factor K_f is used instead of K_t. Then Equation 4.10 becomes:

$$K_f(\Delta s \Delta e E)^{\frac{1}{2}} = (\Delta\sigma_\theta \Delta\varepsilon_\theta E)^{\frac{1}{2}} \tag{4.11}$$

As long as Δs is less than the proportional limit, Δe can be replaced by $\Delta s/E$. This gives

$$\Delta\sigma_\theta \Delta\varepsilon_\theta = \frac{(K_f \Delta s)^2}{E} \tag{4.12}$$

The local stress and strain at the notch in Equation 4.12 can be determined by the Stadnick-Morrow techniques (35).

Note that for the long fatigue life, K_f is nearly equal to K_t. In this investigation the cycle to initiate the crack are quite large, therefore one can use K_t instead of K_f in Equation 4.12.

Figure 4.1 compares the local strain with the distance from the circular notch for three theories in the 7075-T6 aluminum specimen at the nominal stress of 30.1 Ksi

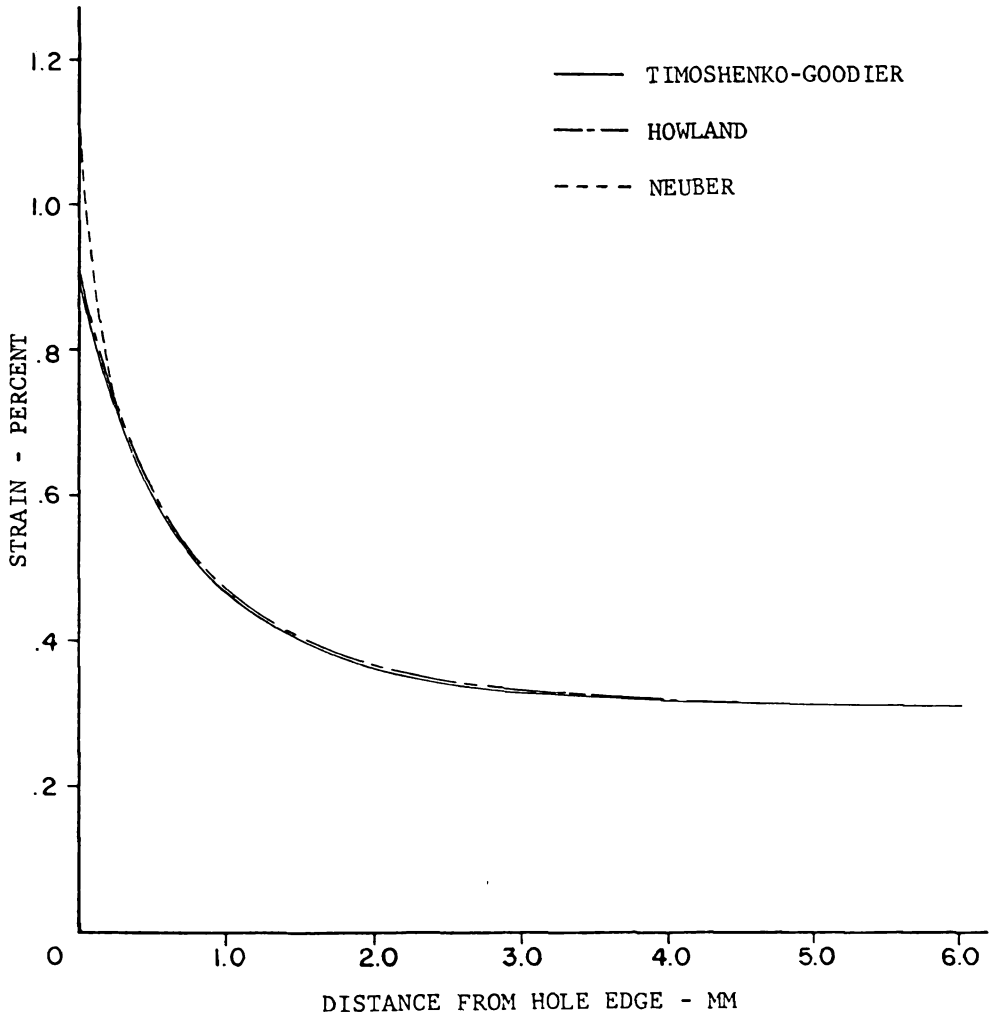

Figure 4.1 Local strains versus distance from circular notch for three theories with a remote loading of 30.1 ksi.

(207.7 MPa). The Howland solution gives results almost identical with the Timoshenko-Goodier solution because the small hole in the test specimen of finite width provides results almost the same as those of the infinite plate that Timoshenko-Goodier assumed. One of these two theories can be selected to compare with the measured strains, the error due to finite width of the plate can be neglected. The Neuber solution is just good for providing information within the plastic zone, therefore the dashed line in Figure 4.1 represents the Neuber solution for the plastic zone.

4.2 Crack Initiation in Terms of Total Strain

Once the stress-strain behavior at the critical location is determined, a cumulative damage analysis is made based on the calculated stresses and strains. The linear relationship between both plastic and elastic strain and the fatigue life was suggested by Smith-Hirschberg-Manson (39) as:

$$\frac{\Delta\varepsilon_\theta}{2} = \frac{\sigma_f'}{E}(2N_f)^b + \varepsilon_f' (2N_f)^c \qquad (4.13)$$

where $\Delta\varepsilon_\theta$ is the total strain amplitude, and

N_f is the number of fatigue cycles.

Morrow (40) defined the constants b, c, σ_f' , and ε_f' by looking upon the fatigue properties of the metal as follows:

σ_f' is the fatigue strength coefficient; σ_f'/E is

elastic strain when $2N_f = 1$,

b is the fatigue strength exponent; the slope of the log $\Delta\varepsilon_e/2$ versus log $2N_f$ plot,

ε_f' is the fatigue ductility coefficient; the intercept of the log $\Delta\varepsilon_p/2$ versus log $2N_f$ plot at $2N_f = 1$, and

c is the fatigue ductility exponent; the slope of the log $\Delta\varepsilon_p$ versus log $2N_f$ plot.

The above constants are experimentally obtained from fatigue testing and substituted into Equation 4.13 to produce base line fatigue data for each type of material.

The first term of the R.H.S. in Equation 4.13 represents the elastic strain curve and the second term represents the plastic strain curve. For long lives, the elastic curve is dominant and for short lives the plastic line dominates (41).

Note that the theoretical solution is based on cycles to failure instead of cycles to initiate the crack. The reason is that the constant values in Equation 4.13 are obtained from the fatigue testing for each type of metal. The test specimens used to obtain base line fatigue data are small unnotched specimens, the initial crack being followed quickly by specimen failure. Therefore, the theory treats the cycles to initiate the crack the same as the cycles to failure when the crack propagation stage is negligible. In this investigation one can compare the number of cycles to initiation and the total strain with

the theoretical solution. Several authors (35-37,40-43) have worked on the total strain-life relationship and produced the base line fatigue data in cumulative damage studied for 7075-T6 aluminum. Endo-Morrow (42) studied the short fatigue life while Martin (41) studied the long fatigue life. The constant-amplitude loading that was applied to the specimens in this study gave the number of the cycles to initiate the crack as about 15,000. This fairly large number of initiation cycles will better fit the Martin data which were used for the long fatigue life.

Data from Martin (41) was based on the completely reversed tensile and compressive stresses or zero mean stress with constant-amplitude loading. In this study, a mean stress has to be considered to eliminate error in fatigue life calculations. Morrow (40) introduced the mean stress parameter as:

$$(\frac{\Delta\sigma}{2})_{eff} = \frac{\Delta\sigma/2}{1-\sigma_m/\sigma_f'} \tag{4.14}$$

where $(\Delta\sigma)_{eff}$ is the equivalent completely reversed stress range,

$\Delta\sigma$ is the true stress range,

σ_m is the mean stress, and

σ_f' is the fatigue strength coefficient.

For long lives, $\Delta\sigma$ can be elastically related to $\Delta\varepsilon$, the true strain range ($\Delta\varepsilon$) can be measured from the experiment by the moiré technique, σ_m and σ_f' are known values, then $(\Delta\sigma)_{eff}$ will be obtained.

All of the above equations apply to the non-coldworked specimen. None of the theories had worked on the total strain-life of the coldworked specimen subjected to the mandrel hole enlargement in the plane stress condition. Rich-Impellizzeri (37) predicted the design limit stress-life of coldworked holes in aluminum under plane strain conditions. Therefore, the experimental data for the total strain-life of coldworked specimens in this investigation are also compared with the base line fatigue data of the non-coldworked specimen.

4.3 Experimental Results

The experimental data in this section are obtained from 6 specimens, 2 non-coldworked, 2 medium coldworked, and 2 heavy coldworked. Constant-amplitude loading at 30.1 Ksi (207.7 MPa) maximum and 3.1 Ksi (21.4 MPa) minimum were applied throughout this investigation. The local strains and total strains were measured by moiré techniques as in Chapter 2. For coldworked specimens, only the change of residual strains were measured not including the residual strains during coldworking process. Life to crack initiation was determined from crack growth measurements during the initial stage of the growing crack.

4.3.1 Local Strain Versus Distance from Edge of Hole

Figure 4.2 shows the moiré fringe patterns which were used for measuring the strains. The local strains were measured with both maximum and zero loads applied and they

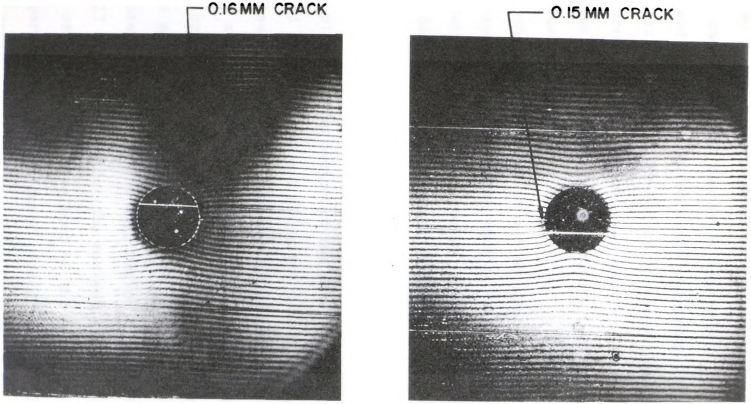

Figure 4.2 Moiré fringe patterns of the initiation of a crack from the hole edge in test specimens; (a) non-coldworked, (b) coldworked.

were the average of the data obtained from the R.H.S. and L.H.S. of the hole. At the beginning, the strains were measured after each increment of cyclic loading (see Figures 4.3 and 4.4) until the crack initiated. The experiments showed no plastic deformation appearing during the first ten cycles of loading, therefore the experimental strain data in Figures 4.3 and 4.4 were recorded at 100, 1,000,. . ., etc. cycles. There is good agreement between measured and theoretical strains at the area close to the hole edge. At a distance of about 0.5 to 3.0 mm away from the hole edge, the theory predicts a little smaller value, and for distances larger than 3.0 mm the theory agrees quite well. The plastic deformation increase is proportional to the increment of cyclic loading. The non-coldworked specimens exhibited more plastic deformation than the coldworked ones, for example the plastic deformation of the non-coldworked specimens measured at zero load was about 0.1 percent strain at 17,400 cycles while that of the coldworked ones was about 0.05 percent strain at 25,000 cycles. When the crack had initiated and grown to a length of about 0.1 to 0.2 mm, the strains were measured again and compared with the same theories in Figures 4.5 - 4.7. The deformation increased by the amount of 17 to 30 percent for the maximum load applied and a factor of two for the zero load of the non-coldworked specimen compared with the non-crack condition. The deformation for the cracked and non-cracked conditions at the maximum load

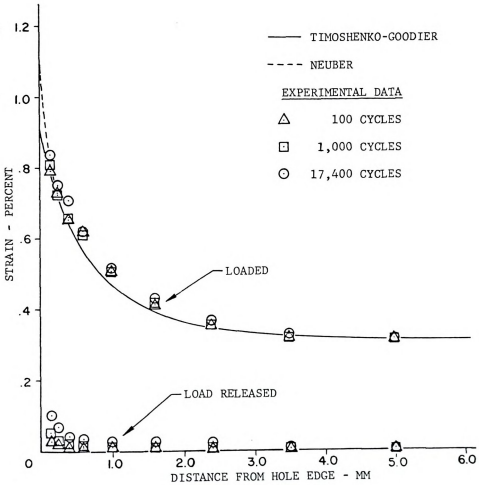

Figure 4.3 Comparison of local strains versus distance from hole edge with the theories for non-coldworked specimen.

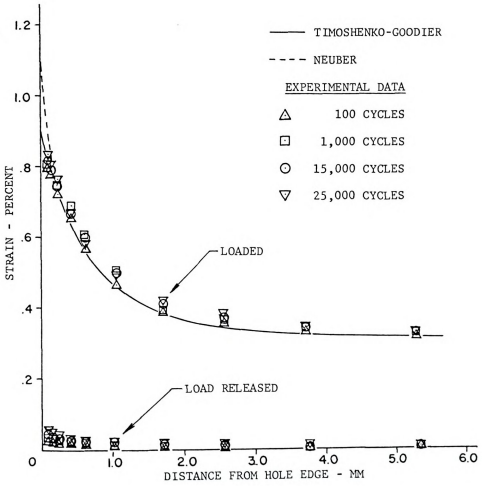

Figure 4.4 Comparison of local strains versus distance from hole edge with the theories for cold-worked specimen.

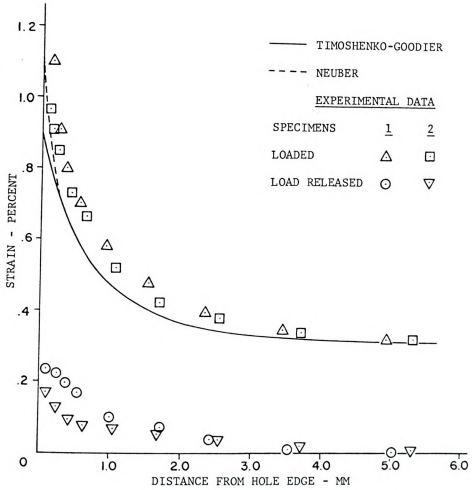

Figure 4.5 Local strains versus distance from hole edge after a crack had initiated in the non-coldworked specimens.

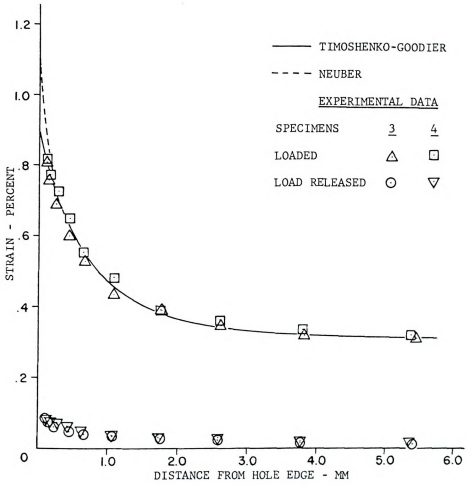

Figure 4.6 Local strains versus distance from hole edge after a crack had initiated in the medium coldworked specimens.

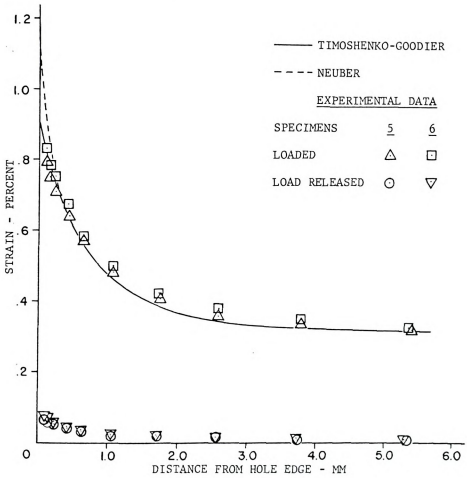

Figure 4.7 Local strains versus distance from hole edge after a crack had initiated in the heavy coldworked specimens.

were almost the same for the coldworked specimens, while the deformation at the zero load increased by about 40 percent.

4.3.2 Total Strains Versus Cycles to Crack Initiation

Cycles to crack initiation in smooth specimens were obtained from the long life fatigue data of Martin (41). The effect of mean stress was determined to correct the values of the total strain '$\Delta\varepsilon$'.

The experimental data and the results from Martin (41) are compared on the log-log scale in Figure 4.8; there is close agreement in both non-coldworked and coldworked specimens.

The strain-amplitude is about 0.85 percent strain and the crack initiation cycles are about 17,500 for the non-coldworked specimens. For the coldworked specimens, the strain-amplitude is about 0.73 percent strain. The cycles to crack initiation is 35,000 for medium coldwork and 24,000 for heavy coldwork. Since all of the experimental data are along the elastic line of the total strain-life curve, this means that the elastic condition dominates for this investigation of strains versus crack initiation cycles.

4.4 Discussion of Results

The local strains increased for each increment of cyclic loading; this material will be strain hardened under cyclic conditions (25). In other words, the strain concentration factors at the notch root will increase during

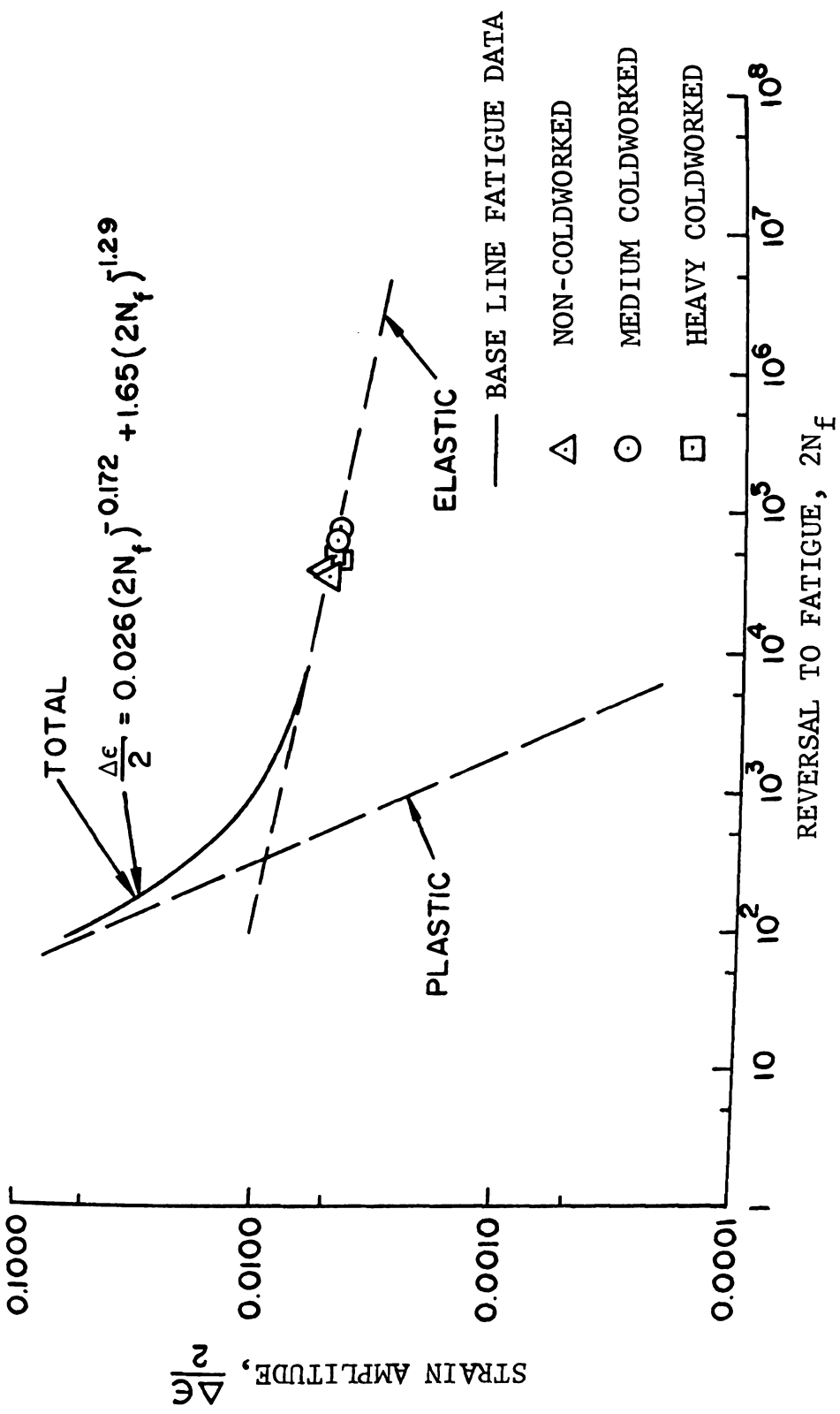

Figure 4.8 Comparison of total strains versus initiation life with base line fatigue data for 7075-T6 aluminum.

cycling. The increasing amount of the strain concentration factors are very small for this material (25) due to the cyclic hardening and the small nominal stress applied. A constant nominal stress of 30 Ksi (207 MPa) will produce a local stress at the notch root of about 90 Ksi (621 MPa), this amount of local stress is just a little larger than 73 Ksi (504 MPa) which is the yield stress of 7075-T6 aluminum that was used in the experiment. Although the measured strains obtained from cyclic loading were compared with the theoretical results obtained from monotonic loading, they are still in good agreement.

Comparison of crack initiation in smooth and notched specimens for the total strain-life showed that the Smith-Hirschberg-Manson solution (39) used to obtain the base line fatigue data for 7075-T6 aluminum by Martin (41) worked well to predict the cycles to initiation. The initiation life of the heavy coldworked specimens were shorter than those of the medium coldworked ones; these results might be explained by an optimum interference level (4, 44 and 45). Potter-Grandt (4) predicted that the maximum allowable mandrel interference 'u_o^*' for this type of specimen is about 0.0037 inches (0.094 mm) radial expansion. This value compares with the 0.0040 inches (0.102 mm) radial expansion in this study. Since u_o^* leads to the maximum region of residual compressive stresses (4), the larger radial expansion such as 0.0060 inches (0.152 mm) will reduce the amount of these residual compressive stresses and cause shorter crack initiation life.

CHAPTER 5

CRACK GROWTH

5.1 Overview

Crack propagation occupies a major portion of the useful fatigue life in many cracked structural components. Cracks tend to be generated in components with notches and unintentional stress raisers such as tool marks or burrs on polished surfaces. The toleration of visible cracks, in a "fail-safe" structure, and their growth during the operation of aircraft are factors which further established the significance of crack propagation studies.

There is still no method whereby the life of a structural element can be predicted with sufficient accuracy without carrying out fatigue tests which take careful account of all the parameters involved. This is mainly because the actual mechanism of fatigue is still not understood and therefore empirical technical solutions must be sought. In general, crack propagation rate depends on the kind of material, the alloying elements and the grain structure.

Careful observation of striations during crack propagation indicates crack extension during each interval of load cycles. In any case, if the final objective is to make a crack growth prediction for structure member, a knowledge of the average crack growth is sufficient. In other words, crack propagation can be considered to be continuous.

The general form of the crack propagation laws were proposed by Christensen and Harmon (46) in the form,

$$\frac{da}{dN} = F[\sigma_\infty, \sigma_{\infty m}, a, d_i] \tag{5.1}$$

where: a is the half crack length.

N is the number of cycles.

σ_∞ and $\sigma_{\infty m}$ are the amplitude of cyclic stress, and the mean stress respectively at points remote from the crack.

d_i are material constants (i = 1, 2, 3, - - -).

The crack propagation laws mentioned above gave only indirect quantitative consideration to crack tip stresses. A more fundamental approach for crack propagation depending on crack stresses was proposed by Paris and Erdogan (47).

$$\frac{da}{dN} = c(\Delta K)^m \tag{5.2}$$

where: c and m are empirical constants.

ΔK is the range between maximum and minimum stress intensity factors.

For the 7075-T6 aluminum, the constants c and m were found from baseline fatigue tests of crack geometrics with known stress intensity calibrations by Grandt and Hinnerichs (14) to be equal to 0.945045×10^{-19} in./cycle and 3.44371 respectively when ΔK is in psi-in.$^{\frac{1}{2}}$.

5.2 Experimental Results

Crack lengths were measured on both surfaces of the specimen, but the results used were from the front side. Crack lengths between the front and back side of the non-coldworked specimens were almost identical. For the cold-worked specimens, the crack lengths on the back side were slightly shorter than the crack lengths on the front side after the same number of cycles because of the different amount of residual strains between front and back side. These different amounts of residual strains were caused by the nature of the coldworking operation in which a force was exerted perpendicular to the specimen surface through the sleeve and thus constrained deformation of the hole on the back side (13).

Crack growth curves for three different coldworking processes are given in Figure 5.1.

For the non-coldworked specimens, two cracks were observed during fatigue testing, one on each side of the hole and both cracks grew almost the same length. The cracks originated at the edge of the holes in a plane perpendicular to the surface of the test piece and perpendicular to loading direction [this is called stage II (48)]. The crack lengths at this condition were about 0.1 to 0.3 mm., then the fracture plane rotated around the axis in the direction of the crack propagation until it formed an angle of about 45° with the loading direction and the surface of the sheet. The transition occurred gradually and had its origin in the shear

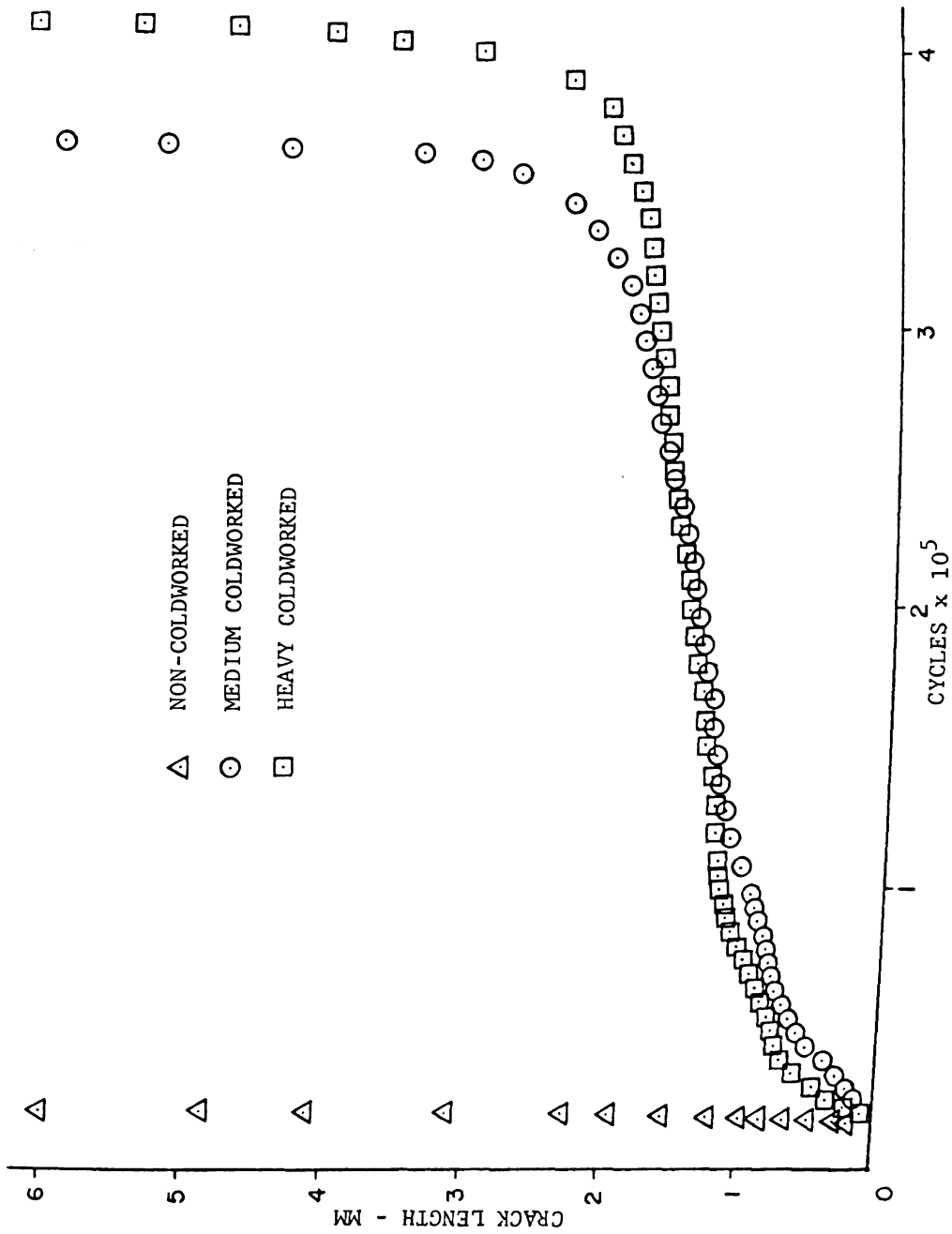

Figure 5.1 Comparison of growth curves for cracks emanating from holes in various coldworked specimens.

lip planes at the surface of the sheet, from where it spread to the whole length of the specimen. The extension of the fatigue crack in this inclined plane after the rotation is called stage III (48). The stage III in the experiment occurred as a single shear plane on both sides of the hole.

For the coldworked specimens, several cracks appeared almost simultaneously in all specimens, but just one on each side of the holes continued to grow to the final crack length of about 6.00 mm. The cracks on both sides of the hole grew almost the same length in the plastic zone when subjected to the stage II condition. The crack lengths at this stage II condition for the coldworked specimen were much longer than for the non-coldworked specimen. There was about 2.00 mm to 3.00 mm before they changed to stage III condition (see Figure 5.2). When the crack on one side of the hole grew through the elastic-plastic boundary it would grow rapidly to the final crack length and the crack on another side of the hole would stop or grow slowly with its tip still in the plastic zone or just beyond the elastic-plastic boundary.

Crack growth rates for the medium coldworked and the heavy coldworked specimens in Figure 5.3 are almost the same. Crack growth originated at the edge of the hole at the rate of about 0.20 to 0.29 x 10^{-4} mm per cycle and gradually dropped to the slowest rate of about 0.30 x 10^{-5} mm per cycle at a distance 1.50 mm from the edge of the hole. After that the growth rates increased and had the value about 0.90 x 10^{-3} mm per cycle at the final crack length. The growth rates for the

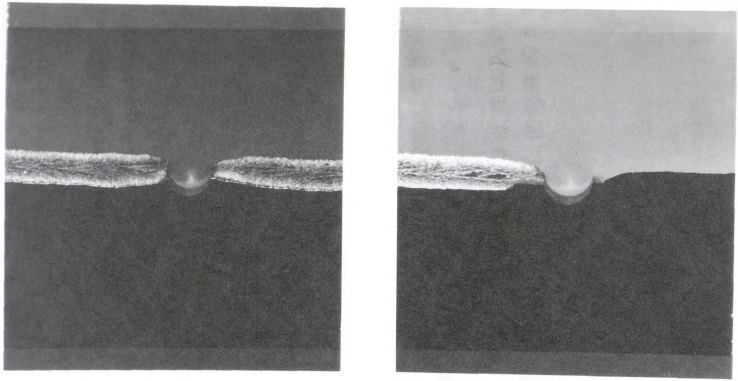

(a) (b)

Figure 5.2 Photographs of fatigue fractures; (a) non-coldworked specimens, (b) coldworked specimens.

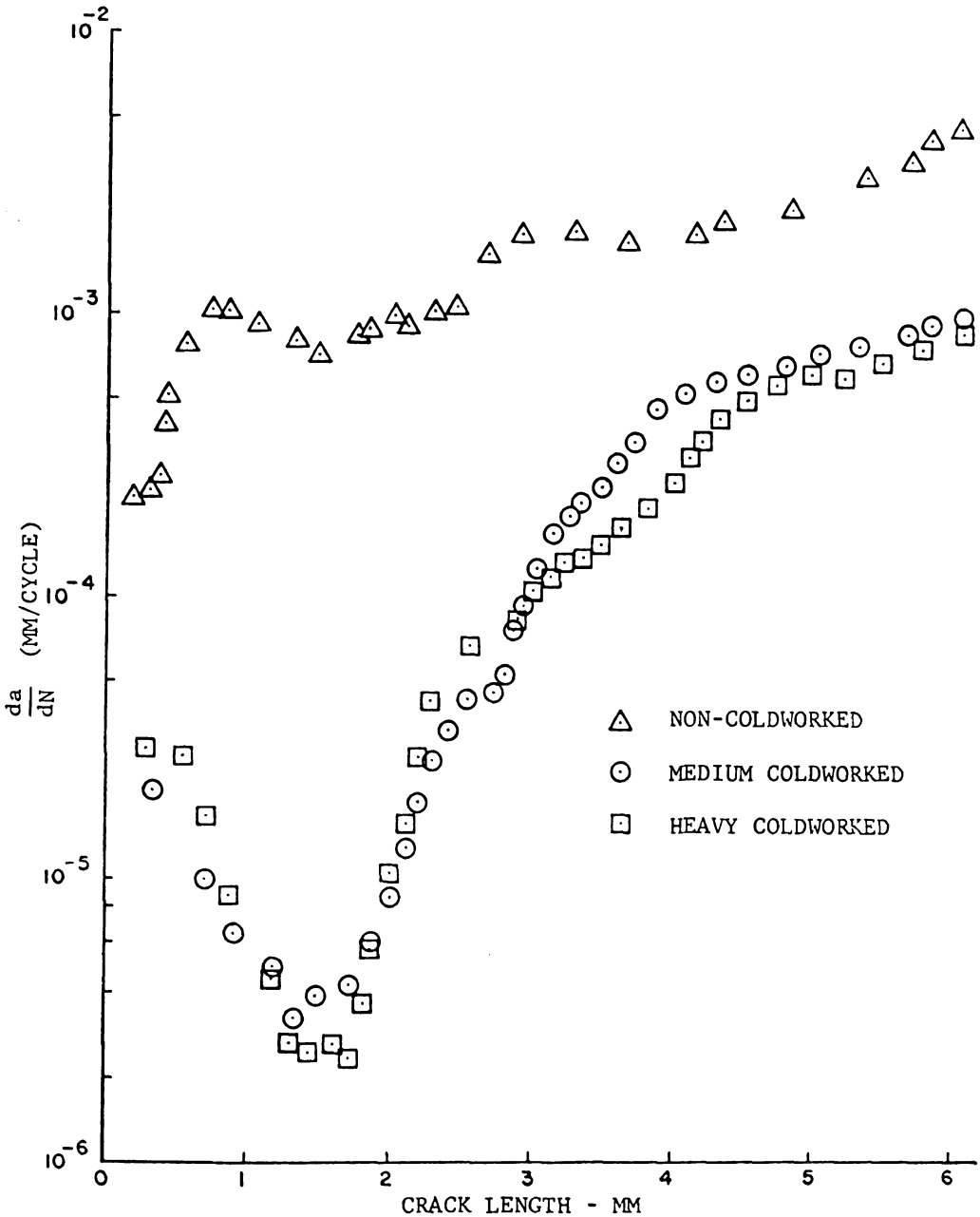

Figure 5.3 Comparison of growth rates for cracks emanating from holes in various coldworked specimens.

non-coldworked specimens were much higher than the coldworked ones; crack growth rates started at 0.23×10^{-3} mm per cycle at a distance of about 0.20 mm from the hole edge and rapidly increased to 1.00×10^{-3} mm per cycle at a distance 0.75 mm from the edge, then slowly increased to the rate of 0.47×10^{-2} mm per cycle at the final crack length.

Crack lengths in the stage II condition for the coldworked specimens were seen to be within the plastic region and have very small deformation or burrs along the crack lines. They then gradually change to stage III condition when the cracks pass through the elastic-plastic boundaries. The stage III condition occurs in the elastic region and obtains large deformation along the crack lines, the same as in non-coldworked specimens (see Figures 5.4 and 5.5). These deformations will affect the residual strains ahead of the crack tips.

5.3 Discussion of Results

From the results, the coldworked holes had a much longer fatigue life than the non-coldworked holes (about 16.8 times for medium coldworked and 18.6 times for heavy coldworked holes). Phillips (49) recorded increased fatigue life with increasing amounts of interference--roughly a factor of 10 for maximum interference over the non-coldworked hole. But those were 0.375 inch (9.50 mm) holes in 0.25 inch (6.40 mm) thick specimens. In a comparison of specimen thickness effects, all 0.375 inch (9.50 mm) holes were coldworked to 0.019 inch (0.48 mm)--equivalent to a 0.010 inch

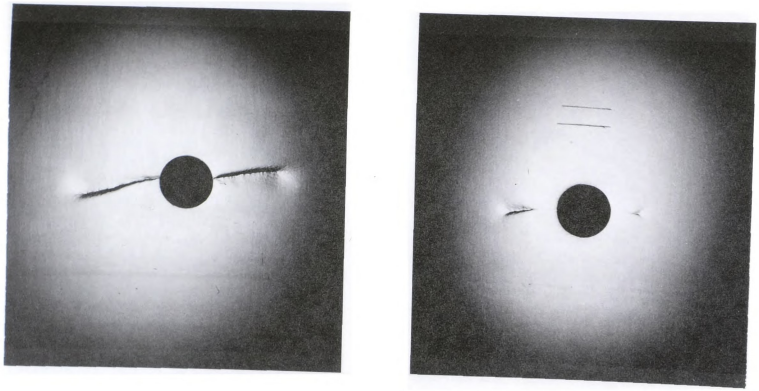

(a) (b)

Figure 5.4 Photographs of plastic deformation in the wake of cracks; (a) non-coldworked specimen, (b) coldworked specimen.

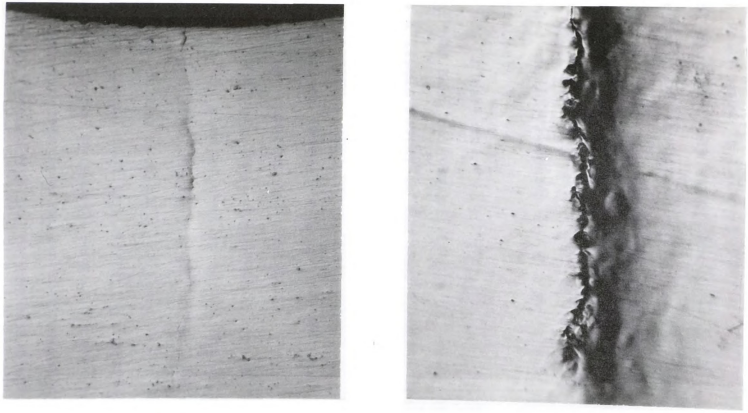

(a) (b)

Figure 5.5 Photomicrographs of plastic deformation in the wake of a crack of coldworked specimen (Magnification x 100); (a) in plastic zone, (b) in elastic zone.

(0.25 mm) expansion on a 0.195 inch (4.95 mm) hole which is between the 0.0080 inch (0.204 mm) and 0.0120 inch (0.304 mm) value used in this experiment. His material was 2024-T851 aluminum, his stress levels were 30 Ksi (207 MPa), and the ratio of the minimum stress to the maximum stress was equal to 0.10. His experiments gave a life to failure of approximately 400,000 cycles compared with 370,000 cycles for the medium coldworked and 410,000 cycles for the heavy cold-worked in this research. The results are in quite good agreement.

A feature of crack propagation for the specimens that had been coldworked is that the crack propagation rate was a little faster in the area close to the hole edge and gradually dropped until at a crack length of about 1.50 mm, it increased. This early rapid growth gives higher values of the stress intensity factor at the area close to the hole edge in the experimental analysis.

The very small deformations or burrs along the crack lines in the plastic regions around the holes of the cold-worked specimens are the effect of the small local stresses that act on the area close to the holes. These small local stresses caused from the linear superposition of the local stresses caused by remote tensile forces and the compressive residual stresses from coldworking operation. The dramatic reduction in stresses due to residual compression caused very small deformation along the crack lines in the plastic regions.

CHAPTER 6

CRACK CLOSURE

During crack propagation a zone of residual tensile deformation is left in the wake of the moving crack. This residual tensile deformation occurred in the specimen that had not been coldworked. For the coldworked one, additional residual compressive stress had already been in the specimen from the coldworking process.

These deformations (or residual stresses) effectively decrease the amount of crack opening. During unloading, these residual stresses can cause the crack to close above zero load. Elber (24) explained fatigue crack retardation by the residual strains in the plastically deformed wake of the propagating crack. The residual compression must be overcome before the crack surface can separate to allow propagation. Sharpe and Grandt (50) used a laser interferometry technique (almost the same as IDG technique) to determine the opening load. Their technique had the significant advantage of providing the sensitivity capable of determining when the crack physically separated at the specimen surface.

6.1 Load-Displacements at Crack Tips and Discussion

Typical plots of load versus displacement at the tip for various crack lengths and coldworkings are shown in Figures

6.1 - 6.3. These were recorded with the IDG fringe counter at a distance of about 50 microns from the crack tip with a distance of 50 microns between the indentations. The straight lines in those figures are the predicted load-displacement relations taken from reference (23) for elastic specimens.

The disadvantage of the fringe counter unit is that it always counts every change of fringe order as the same sign for both loading and unloading. Sometimes, fringe motion can be caused by rigid-body motion and the change in fringe order will be in a different direction, causing no change in displacement, yet the fringe counter still records it as the same sign. For the real test, one has to observe the direction of fringe motion to eliminate this error. Some of the load-displacement curves in Figures 6.1 - 6.3 had to be redrawn to account for the different direction of fringe motion to obtain the correct results.

The results above the crack opening load agree fairly well with the theory for the non-coldworked specimen with a short crack (1 mm) and for all specimens when the cracks are long (3 mm and 6 mm). The displacements are very small for the coldworked specimens with short cracks (about 1 mm) and none of these agree with theory.

6.2 Crack Opening Load and Discussion

Six specimens, two for each coldworking process, were fatigue tested and the crack opening load observed. Figure

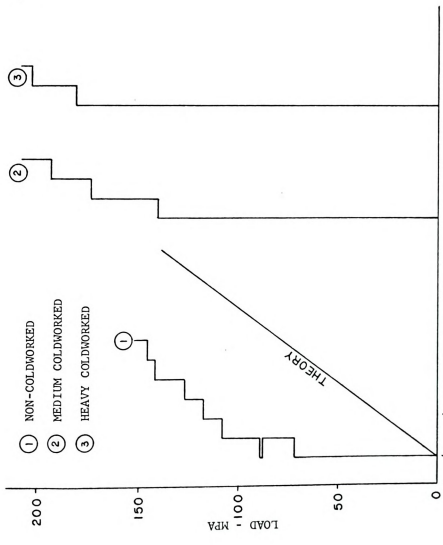

Figure 6.1 Load-displacement curves of 1 mm cracks for various coldworked specimens.

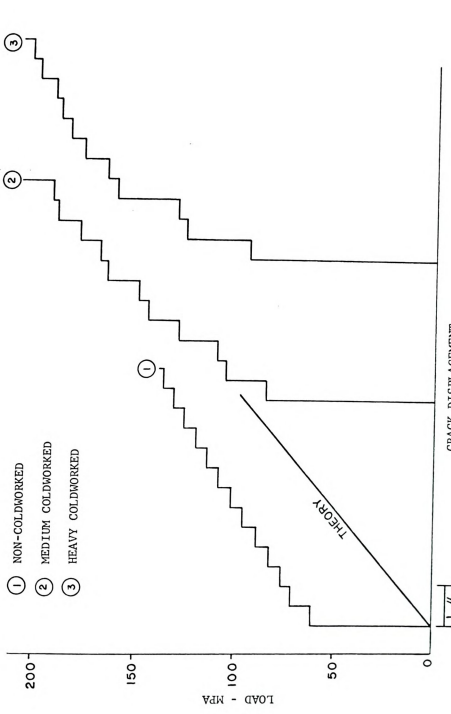

Figure 6.2 Load-displacement curves of 3 mm cracks for various coldworked specimens.

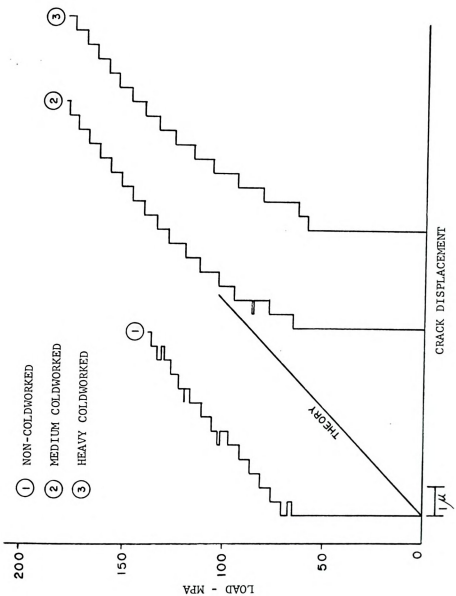

Figure 6.3 Load-displacement curves of 6 mm cracks for various coldworked specimens.

6.4 shows that for the non-coldworked specimens the load ratios $Q_{open} = P_{open}/P_{max}$ are the same for every crack length. Q_{open} was about 0.3 when the specimen loading was increased to the maximum and 0.23 when the specimen loading was decreased to the minimum. For medium coldworked (0.102 mm radial expansion) specimens in Figure 6.5, Q_{open} of the short cracks (1 to 2 mm) is about 0.7 and drops to 0.25 at long cracks (4 to 6 mm). Figure 6.6 shows Q_{open} in heavy coldworked (0.152 mm radial expansion) specimens, the value of Q_{open} begins at 0.8 when the cracks are 1 to 2 mm long and drops to 0.25 for the 4 mm cracks, then gradually increases to 0.3 for the 6 mm cracks.

The results given in the opening statement indicated that the effect of the deformation at the crack tip for various crack length of non-coldworked specimens were the same. For the coldworked specimens, the residual compressive stress caused more crack closure and high Q_{open} in the plastic zone but dropped to the same value of Q_{open} that the non-coldworked specimens had in the elastic zone. The more coldwork applied the more crack closure will occur.

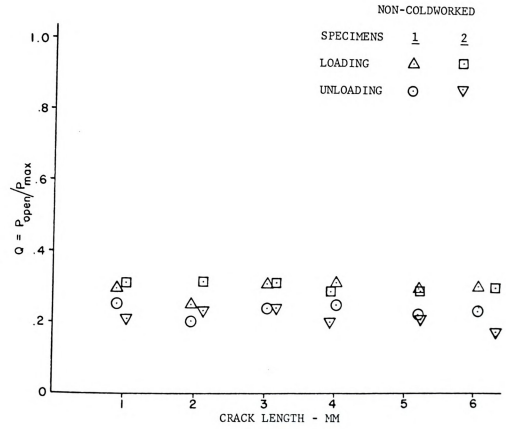

Figure 6.4 Relationship between crack tip opening load and crack length for non-coldworked specimens.

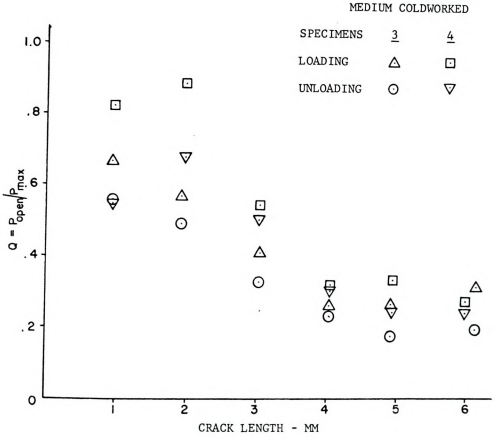

Figure 6.5 Relationship between crack tip opening load and crack length for medium coldworked specimens.

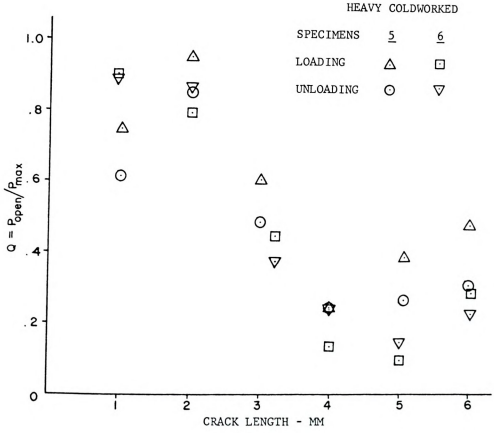

Figure 6.6 Relationship between crack tip opening load and crack length for heavy coldworked specimens.

CHAPTER 7

STRESS INTENSITY FACTOR

7.1 Theories of the Stress Intensity Factor

The stress intensity factor, K_I, is the linear elastic fracture mechanics parameter which characterizes crack behavior in many materials. The relationship of stress intensity factor and elastic stresses were first calculated by Inglis (51). The mode I crack tip stresses are:

$$\sigma_x = \frac{K_I}{\sqrt{2\pi r}} \cos\frac{\theta}{2}[1 - \sin\frac{\theta}{2} \sin\frac{3\theta}{2}] \qquad (7.1)$$

$$\sigma_y = \frac{K_I}{\sqrt{2\pi r}} \cos\frac{\theta}{2}[1 + \sin\frac{\theta}{2} \sin\frac{3\theta}{2}] \qquad (7.2)$$

$$\sigma_{xy} = \frac{K_I}{\sqrt{2\pi r}} \sin\frac{\theta}{2}\cos\frac{\theta}{2}\cos\frac{3\theta}{2} \qquad (7.3)$$

where r and θ are the polar coordinates with the origin at the crack tip and the crack along the negative x-axis

K_I is the mode I stress intensity factor.

The corresponding elastic strains for the plane stress case are:

$$\varepsilon_x = \frac{K_I}{E\sqrt{2\pi r}} \cos\frac{\theta}{2}[(1-\upsilon) - (1+\upsilon)\sin\frac{\theta}{2}\sin\frac{3\theta}{2}] \qquad (7.4)$$

$$\varepsilon_y = \frac{K_I}{E\sqrt{2\pi r}} \cos\frac{\theta}{2}[(1-\upsilon)+(1+\upsilon)\sin\frac{\theta}{2}\sin\frac{3\theta}{2}] \qquad (7.5)$$

$$\varepsilon_{xy} = \frac{2(1+\upsilon)K_I}{E\sqrt{2\pi r}} \sin\frac{\theta}{2}\cos\frac{\theta}{2}\cos\frac{3\theta}{2} \qquad (7.6)$$

where E and υ are Young's modulus and Poisson's ratio, respectively.

The general equation for the stress intensity factor will be written as:

$$K = \sigma\sqrt{\pi a}\ F\ (a) \qquad (7.7)$$

Bowie (10) has analyzed the case of cracks at the edge of circular hole in plates loaded in remote tension. He showed that the stress intensity factor can be expressed as:

$$K_B = \sigma\sqrt{\pi a}\ F\ (\frac{a}{r_o}) \qquad (7.8)$$

The function of $(\frac{a}{r_0})$ may be represented by the least squares approximation for radially cracked holes as:

$$F(\frac{a}{r_0}) = [\frac{F_1}{F_2 + \frac{a}{r_o}} + F_3] \qquad (7.9)$$

where F_1, F_2 and F_3 are the constants shown in Table 7.1.

Emery (52) has been using Duhamel's theorem for linear superposition to obtain the stress intensity factor directly from the hoop stress surrounding an unflawed hole as shown in Figure 7.1. The unflawed stress distribution

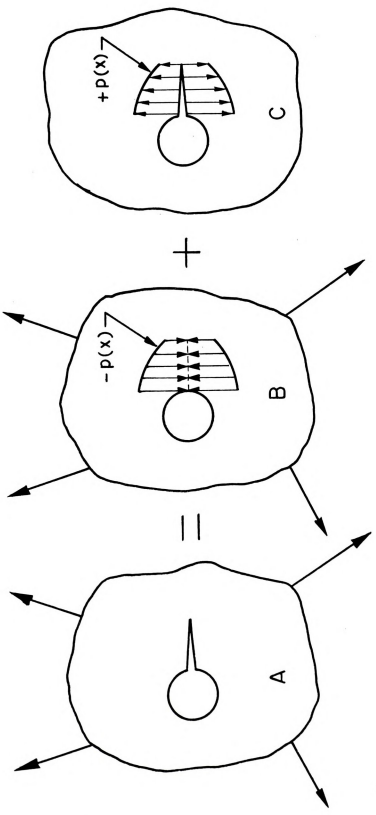

Figure 7.1 Schematic of linear superposition method.

may result from remote loading or be introduced by cold working process. Since there is no crack in case B of Figure 7.1,

$$K_{I,A} = K_{I,B} + K_{I,C} \tag{7.10}$$

$$\text{but } K_{I,B} = 0 \text{ (no crack)}$$

$$\text{therefore } K_{I,A} = K_{I,C}. \tag{7.11}$$

TABLE 7.1--Least squares approximation to Bowie solution for radially cracked holes.

	Single crack	Double crack
F_1	0.8733015	0.6865078
F_2	0.3245442	0.2771965
F_3	0.6762062	0.9438510

Grandt (11) developed a solution for radial hole cracks loaded with arbitrary crack face pressure. When the pressure is specified as the hoop stress surrounding an unflawed fastener hole (see Figure 7.2). The hoop stress may arise from remote and/or coldworking.

The analytical approach of Grandt (11) is based on work by Rice (53). The problem consists of radial cracks of length 'a' emanating from a circular hole of radius 'r_o'. The flaws are loaded with an arbitrary pressure p(x) which is perpendicular to the crack faces and symmetric with

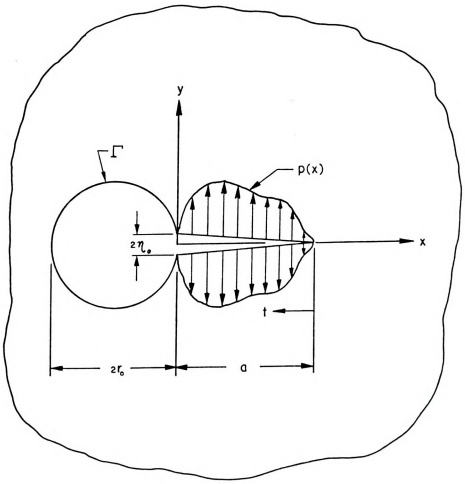

Figure 7.2 Open hole containing a radial crack subjected to pressure p(x).

respect to the x-axis. The pressure distribution is restricted to mode I loading only.

The stress intensity factor for a given crack geometry under arbitrary loading in the condition of plane stress is given by:

$$K_I = \frac{E}{K_B} \int_0^a p(x) \frac{\partial \eta}{\partial a} dx \qquad (7.12)$$

where E is the elastic modulus

K_B is the Bowie solution for the stress intensity factor.

$p(x)$ is an arbitrary crack face pressure.

η is the y-component of the crack surface displacements.

a is the crack length.

For the mandrel hole enlargement or coldworked hole, crack face pressure $p(x)$ may be defined as the addition of the residual hoop stress and the hoop stress along a radial line of an unflawed hole loaded with remote tension.

The hoop stress along a radial line of an unflawed hole loaded with remote tension has been expressed by Timoshenko-Goodier (6) as:

$$\sigma_H = \frac{\sigma}{2}[1+(\frac{r_o}{r_o+x})^2] - \frac{\sigma}{2}[1+3(\frac{r_o}{r_o+x})]\cos 2\theta \qquad (7.13)$$

Taking $\theta = \frac{\pi}{2}$ for this experimental problem, one can obtain the hoop stress for unflawed remote loading.

The hoop stress for the coldworked hole was determined by Nadai (1), Hsu-Forman (2), Potter-Grandt (4), etc.

To compute $\frac{\partial \eta}{\partial a}$, the crack opening displacement 'η' must be determined. Orange (54) has shown that the shape of edge cracks under remote tension or bending may be approximated within three percent by conic section of the form:

$$(\frac{\eta}{\eta_o})^2 = \frac{2}{2+m}(\frac{t}{a}) + \frac{m}{2+m}(\frac{t}{a})^2 \qquad (7.14)$$

where η_o is displacement at the crack mouth (t = a).

m is conic section coefficient.

$$m = \pi[\frac{E\eta_o}{2\sigma a y}]^2 - 2 \qquad (7.15)$$

where y is the factor defined from Equation 7.8 as

$$y = \frac{K_B}{\sigma\sqrt{a}} = \sqrt{\pi}[\frac{F_1}{F_2 + \frac{a}{r_o}} + F_3] \qquad (7.16)$$

Finite element results for the crack mouth displacement were closely represented by the least squares expression

$$\eta_o = r_o \sum_{i=0}^{6} D_i (\frac{a}{r_o})^i \qquad (7.17)$$

where D_i are the constants given in Table 7.2.

Figure 7.3 compares the non-coldworked theory by Bowie (10) and the coldworked theory by Grandt* (11). Note that

---

*Grandt provided for this investigation results of K_I obtained from the residual compressive stress as computed according to Hsu-Forman (2).

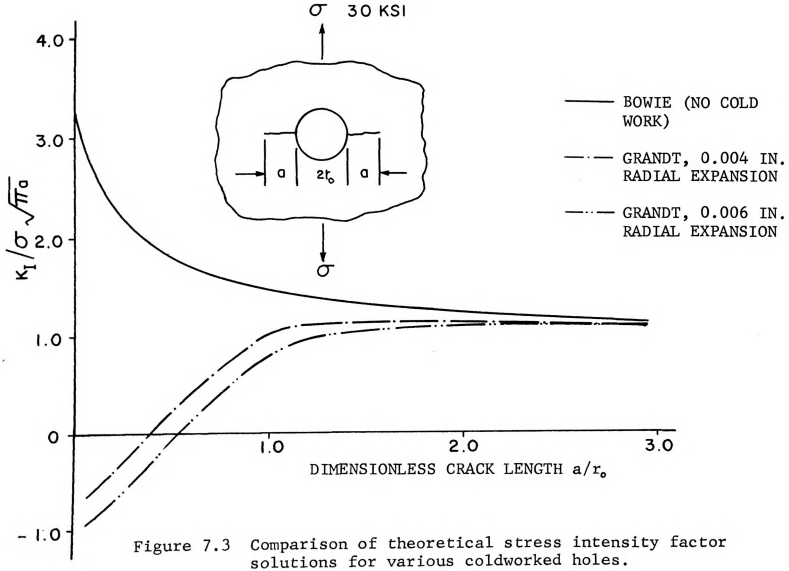

Figure 7.3 Comparison of theoretical stress intensity factor solutions for various coldworked holes.

the arbitrary crack face pressure in the Grandt solution is obtained by the addition of the hoop stress caused by a 30 Ksi (207 MPa) remote load from Timoshenko-Goodier (6) solution and the residual stress caused by the coldworking operation from Hsu-Forman (2) solution. The residual stress was fit with the least square polynomials first then added to the hoop stress caused by remote load.

TABLE 7.2.--Least squares fit of finite element data for crack mouth displacement.

Coefficient	Single crack	Double crack
D_0	-1.567×10^{-6}	1.548×10^{-5}
D_1	6.269×10^{-4}	5.888×10^{-4}
D_2	-6.500×10^{-4}	-4.497×10^{-4}
D_3	4.466×10^{-4}	3.101×10^{-4}
D_4	-1.725×10^{-4}	-1.162×10^{-4}
D_5	3.485×10^{-5}	2.228×10^{-5}
D_6	-2.900×10^{-6}	-1.694×10^{-6}

7.2 Experimental Results

The experimental stress intensity factors for this research were obtained from both the crack growth data and the IDG technique. There was not enough displacement for the IDG technique for very short crack lengths in the specimens that had been coldworked. Therefore, one had to use

crack growth data to calculate the stress intensity factor for very short crack lengths by using Grandt and Hennerichs (14) baseline data for 7075-T6 aluminum.

The stress intensity factor obtained from the crack growth data was computed from da/dN in Equation 5.2. Differentiating the crack growth data requires special care to prevent magnification of experimental error. All of the data analyzed here were first smoothed by a simple averaging technique. Next a least squares parabola was passed through a set of six to seven successive data points, and crack lengths were calculated at five to six regular intervals over the range of the set. The growth rate was calculated by a standard least squares formula which approximates the derivative at the center of six evenly spaced points. The set was then advanced one point and the process repeated until all the data were exhausted.

The data reduction by the IDG technique was taken from the linear portion of the load-displacement curve above the crack opening load in Chapter 6 to obtain the slope $\frac{u_y}{\sigma}$ in Equation 2.24, then an elastic stress intensity factor was reached.

The experimental results of stress intensity factors from two specimens that had not been coldworked are shown in Figure 7.4. The data were obtained from both IDG technique and crack growth curve. The results taken from the loading curve for the IDG technique show slightly higher values than the results from the unloading curve and all of

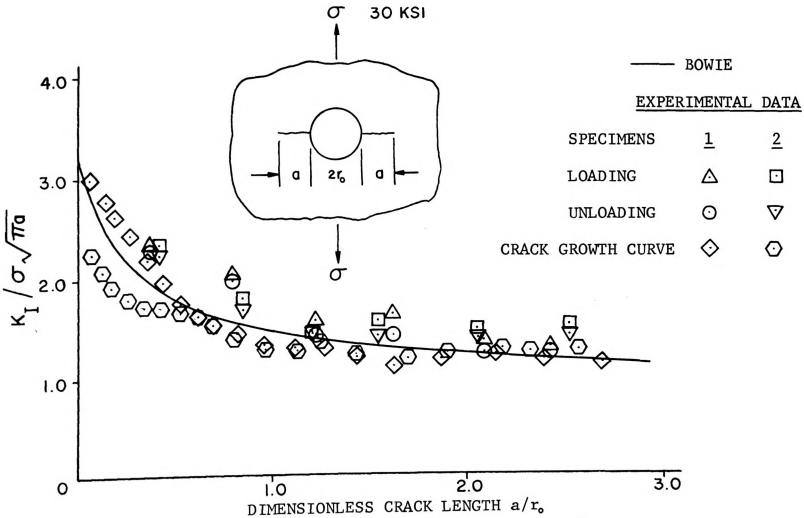

Figure 7.4 Comparison of experimental stress intensity factor with the theory for non-coldworked specimens.

them are higher than the theory by Bowie (10). Data from crack growth curves agree fairly well with the theory. Figures 7.5 and 7.6 compare the theories and experiments for the two coldworking processes. Comparisons with the IDG technique for medium coldworked (0.102 mm radial expansion) were obtained at the crack length about 2 mm from the hole edge and for heavy coldworked (0.152 mm radial expansion) were obtained at the crack length about 3 mm from the hole edge. The Bowie solution gives the stress intensity factor for the non-coldworked hole which had no residual compressive stress caused by the coldworking process. Grandt's solution applies for coldworked specimens and gives results which were very useful to compare with the experimental data. Grandt's solution predicts slightly lower stress intensity factor compared with IDG technique for crack lengths longer than 3 mm from the hole edge. For short cracks, Grandt's computation predicts higher values at 1.5 to 3 mm cracks and lower values at cracks less than 1.5 mm. Note that the larger amount of residual compressive stress from the Hsu-Forman solution compared with the local stress from remote load caused negative crack face pressure $p(x)$, and the stress intensity factor (K_I) in Equation 4.14 became negative at the area close to the hole edge. The negative K_I in Figures 7.3, 7.5 and 7.6 really mean that $K_I = 0$.

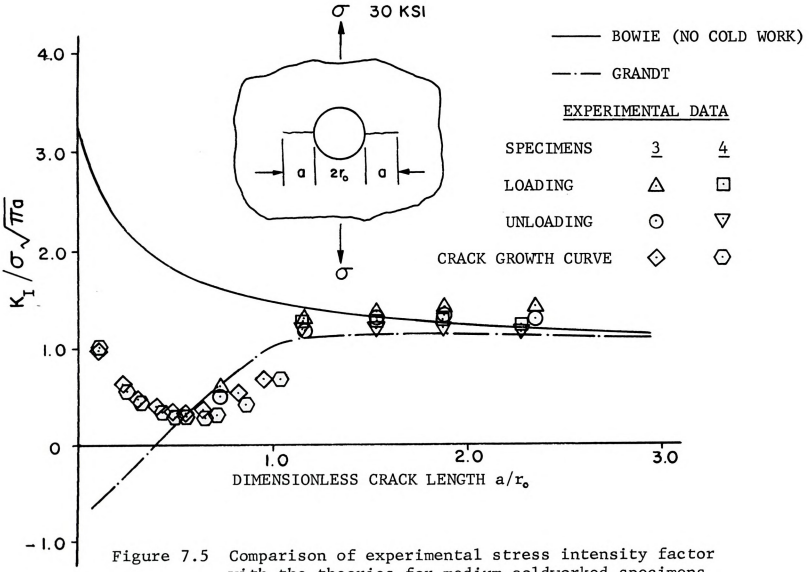

Figure 7.5 Comparison of experimental stress intensity factor with the theories for medium coldworked specimens.

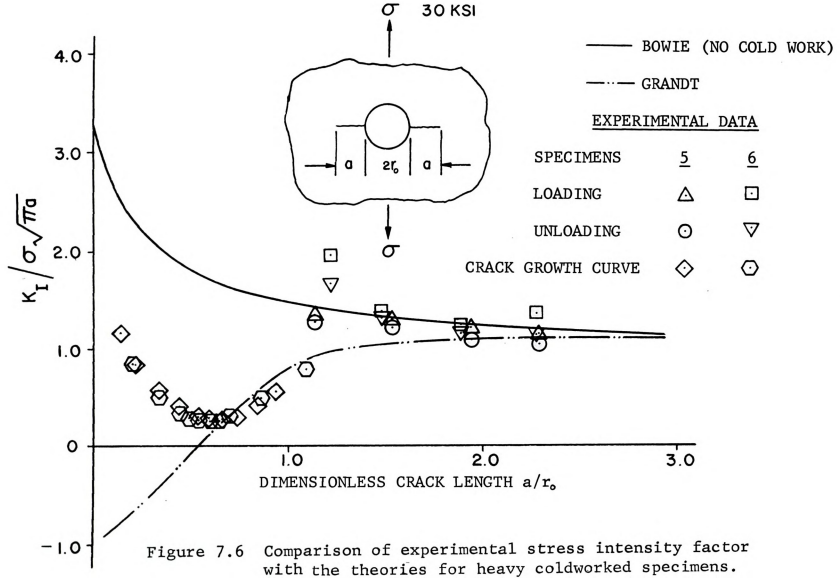

Figure 7.6 Comparison of experimental stress intensity factor with the theories for heavy coldworked specimens.

7.3 Discussion of Results

Only two theories exist to determine the stress intensity factors for radial cracks emanating from a circular hole in a plate, one by Bowie (10) in 1956 for non-coldworked holes and another by Grandt (11) in 1973 for coldworked holes. Grandt applied the integral method of Rice (53) and obtained arbitrary crack face pressure from the addition of local stresses caused by remote load and residual stresses caused by the coldworking process. For residual stress, only Potter-Ting-Grandt (3,4) solution accounts for compressive yielding which occurs on unloading at the area close to the hole edge. This compressive yielding will reduce the amount of residual stresses, resulting in an increase in the amount of arbitrary crack face pressure at the area close to the hole edge.

Unfortunately, the Hsu-Forman (2) solution does not account for compressive yielding. If one knows the approximate compressive yield zone by the theoretical solution there will be a better comparison with the experimental data.

The IDG techniques have a limit of 1 mm from the hole edge to measure the stress intensity factor because accurate measurements cannot be obtained for such small displacements. The set of indentations will be sufficiently accurate within a distance a/20 from the crack tip, where 'a' is the crack length. The distance between each pair of indentations has to be set at least 0.70 mm apart to avoid

interference of fringe patterns from another set, therefore, the data from IDG techniques cannot be plotted continuously as crack growth data can.

The experimental results obtained are slightly higher than those of the theory. This disagreement comes from incompleteness of model and experimental errors.

CHAPTER 8

CRACK SURFACE DISPLACEMENT

In recent years, crack surface displacements have been used widely to analyze fatigue crack growth and as a fracture criterion for materials. Accurate determination of crack surface displacements is often required for fundamental investigation of crack behavior. The shapes of cracks opened by tension are approximated by conic sections (54) and the conic section coefficients related to plate geometry by very simple empirical equations as in Chapter 7.

Experimental studies have been performed by interferometric measurement technique for crack displacement in glass specimens. Crosley-Mostovoy-Ripling (20) and Sommer (21) used this technique to determine the stress intensity factor calibrations. A new method for measuring crack surface displacements applicable to these types of problems has recently been developed by Sharpe-Grandt (50). The technique, which employs laser interferometry, was mentioned before in Chapter 6. This technique is quite sensitive (about 0.1 micron resolution), is readily adaptable to laboratory measurements, and has the capability of obtaining the entire crack displacement profile.

8.1 Experimental Results

The experimental data for crack displacements in this chapter were obtained from the IDG technique by measuring the load-displacement slope in the linear region above the crack opening load for loading and unloading condition. The displacement for a 1 Ksi (6.9 MPa) increment of stress in the linear region was compared with the theoretical solutions. The data for the crack mouth displacements was measured from a set of two indentations at a distance of 75 microns from the hole edge, the data were compared with a least square polynomial from the finite element method by Grandt (11). The crack opening displacement at any distance along the crack line was also measured by the IDG technique and compared with Equation 7.14. The experimental data for crack mouth displacements for the double crack are plotted against the theory in Figures 8.1-8.3. The data are the average of the cracks on R.H.S. and L.H.S. of the hole. The finite element method predicts smaller displacements for the non-coldworked specimens and there is about 10 percent difference between theoretical and experimental data (see Figure 8.1). For the coldworked specimens, the residual compressive stresses caused a smaller crack opening displacement as shown in Figures 8.2 and 8.3.

Crack surface profiles determined by Orange (54) for the double crack and the measured results are compared in Figures 8.4-8.6. Note that displacements closely match the theoretical solution near the crack area close to the hole

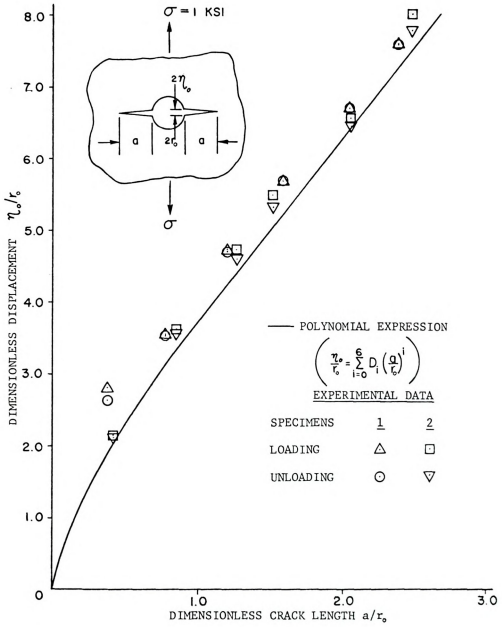

Figure 8.1 Comparison of crack mouth displacement with the theory for non-coldworked specimens.

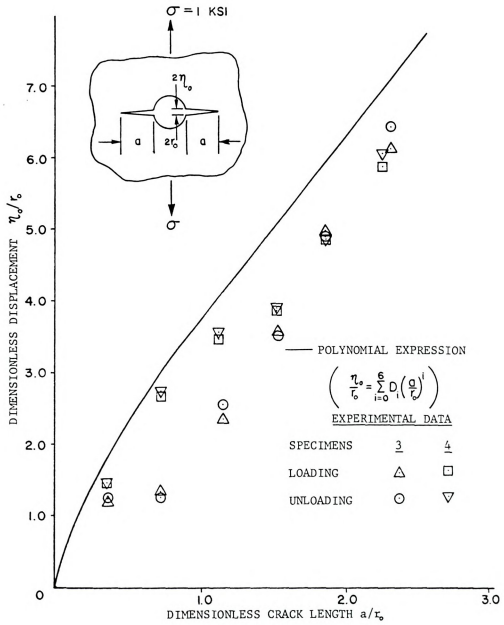

Figure 8.2 Comparison of crack mouth displacement with the theory for medium coldworked specimens.

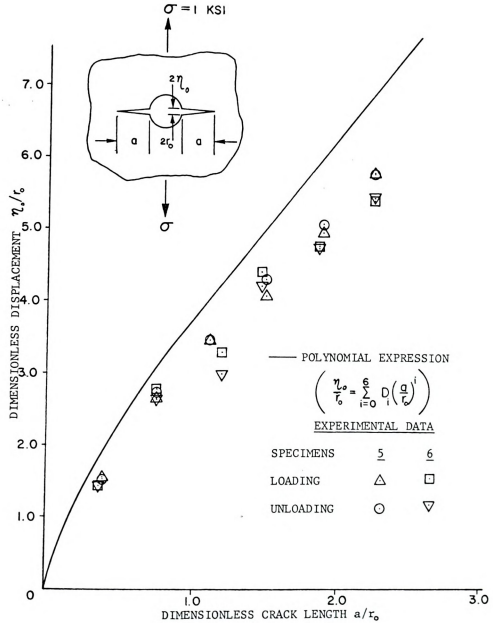

Figure 8.3 Comparison of crack mouth displacement with the theory for heavy coldworked specimens.

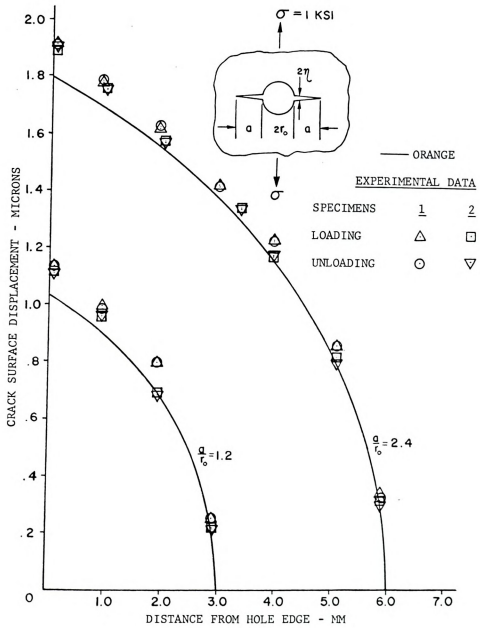

Figure 8.4 Comparison of crack surface profiles with the theory for non-coldworked specimens.

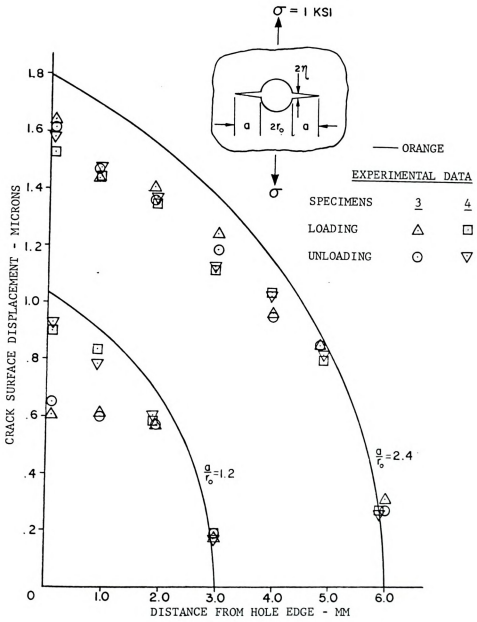

Figure 8.5 Comparison of crack surface profiles with the theory for medium coldworked specimens.

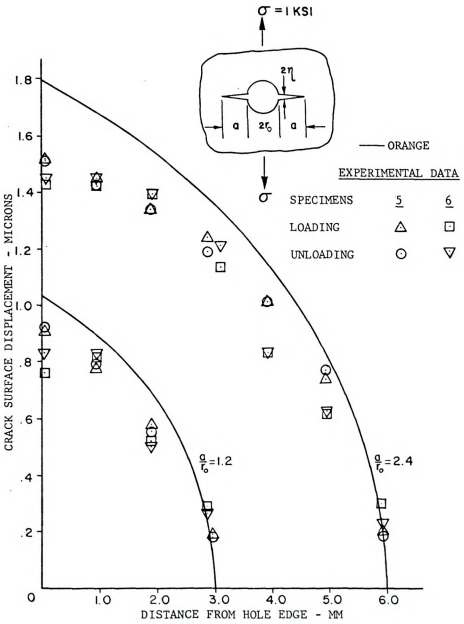

Figure 8.6 Comparison of crack surface profiles with the theory for heavy coldworked specimens.

edge of non-coldworked specimens. Due to residual compressive stresses, as mentioned before, the values for the experimental displacements of coldworked specimens were smaller than the value calculated from theory.

8.2 Discussion of Results

In the experiments, the natural cracks obtained from cyclic fatigue loading were not the same lengths on both sides of the circular hole at the same cycle. This unequal crack length causes some disagreement between experimental and theoretical values. For the non-coldworked specimens, the crack on one side started and grew to length about 1.0 to 2.0 mm then the other side initiated and grew at a faster rate than the first one. This second crack obtained almost the same crack length as the first crack when the lengths were about 5.0 to 6.0 mm. For the coldworked specimens, both R.H.S. and L.H.S. cracks started almost at the same fatigue cycle and maintained the same crack length until the crack on one side reached the elastic-plastic boundary. This crack then grew quite rapidly to the final crack while the crack on another side grew slowly and stopped within or just outside the plastic zone.

CHAPTER 9

STRAIN AHEAD OF CRACK TIP

When a specimen containing a crack or other similar defect is subjected to a tensile or shear stress, a very high stress concentration exists at the crack tip. If the material is assumed to remain elastic and the defect is sufficiently sharp, analytical linear elastic solution for the stress and strain distribution in the region of the crack tip can generally be obtained. However, virtually all metals exhibit some ability to deform plastically without fracture. This results in a region of plastic deformation around the crack tip. If the size of this zone is very much smaller than all other significant dimensions of the structure and defect, the stress and strain distribution outside the plastic zone is not significantly different from the distribution predicted by the elastic solution. When the plastic zone becomes larger, as in a relatively ductile material, the applicability of the above concepts becomes questionable. Attempts have been made by Irwin (55) and Dugdale (56) to correct for the effect of this plastic zone. These attempts have been somewhat empirical and approximate in nature and, although they have been used with some success in predicting actual fracture criteria, they do not represent a true physical model of stress-strain condition

at the crack tip. Analytical solutions to the above elastic-plastic boundary value problem have been developed both theoretically (57,58) and experimentally (59-62) during the past few years. Theoretical solutions work by Rice-Rosengren (57) and Hutchinson (58) applies directly to the tensile-mode crack problem. The experimental techniques are required to measure the strain distribution in the region of the crack tip on a microscopic scale.

In 1964, Oppel-Hill (59) published the results of a study evaluating the various techniques which could be used to conduct such an experiment. They indicated that the optical-interference technique provided the greatest sensitivity and accuracy. However, this method only provides a measurement of through-the-thickness strains in a sheet specimen. Later on, Kobayashi-Ingstrom-Simon (60), Liu-Ke (61), and others discussed several other methods which could provide a means of measuring in-plane strain. The grid-interference or moiré method appeared to be one of the best methods to provide sufficient sensitivity for the measurement of strains.

9.1 Theoretical Method

The linear elastic solution in the stresses and strains in cracked solids was mentioned before in Chapter 7. For stress applied well below the yield stress ($\sigma << \sigma_{ys}$), the plastic zone is negligibly small and linear elastic fracture mechanics is reasonable. In cases where the

plastic zone is larger, a "correction factor" may be used to account for its effect. Irwin (55) applied the plastic zone correction factor to the solutions of linear elastic stress intensity factor to obtain the correct results for the effect of plastic deformation at the crack tip.

The Bowie solution in Equation 7.8 becomes:

$$K_I = \sigma\sqrt{\pi(a+r_p^*)}\ F\left(\frac{a}{r_o}\right) \tag{9.1}$$

where r_p^* is the plastic zone correction factor, and

$$r_p^* = \frac{K^2}{2\pi\sigma_{ys}^2} \tag{9.2}$$

$$\text{The actual plastic zone } (r_p) = 2r_p^* \tag{9.3}$$

The stress intensity factor (K) in Equation 9.2 is first calculated by the linear elastic formula with no plastic zone correction factor, then r_p^* will be obtained. This r_p^* is substituted into Equation 9.1 to obtain the correct value of stress intensity factor (K_I).

In Equations 7.2 and 7.5 for angle $\theta = 0$, the mode I crack tip stress and strain in y-direction are

$$\sigma_y = \frac{K_I}{\sqrt{2\pi r}} \tag{9.4}$$

$$\varepsilon_y = \frac{K_I}{E\sqrt{2\pi r}}\ (1-\upsilon) \tag{9.5}$$

Hutchinson (58) developed a deformation theory of plasticity for a material obeying power law strain hardening.

The crack tip stresses, strains, and displacements can be written as

$$\sigma_{ij}(r,\theta) = K_{st}\, r^{-\frac{1}{n+1}}\, \sigma_{ij}(\theta) \tag{9.6}$$

$$\varepsilon^{p}_{ij}(r,\theta) = \alpha\, K^{n}_{st}\, r^{-\frac{n}{n+1}}\, \varepsilon_{ij}{}^{p}(\theta) \tag{9.7}$$

$$u_i(r,\theta) = \alpha\, K^{n}_{st}\, r^{\frac{1}{n+1}}\, u_i(\theta) \tag{9.8}$$

where K_{st} is the amplitude of the singularity,

n is the power hardening coefficient, and

α is a material constant.

$\sigma_{ij}(\theta)$, $\varepsilon^{p}_{ij}(\theta)$, and $u_i(\theta)$ can be obtained from the plastic properties of the materials.

The amplitude of the singularity for small scale yielding is:

$$K_{st} = \left(\frac{\pi}{\alpha I}\right)^{\frac{1}{n+1}} (\sigma^{\infty})^{\frac{2}{n+1}} \tag{9.9}$$

where $\overline{\sigma}^{\infty}$ is the magnitude of the tensile stress far from the crack and $\sigma^{\infty} = \sigma^{\infty}/\overline{\sigma}_{ys}$, and I is the numerical value for various values of n, I appears to approach a constant value ($\tilde{}$2.8) for the large n.

Equations 9.6-9.8 indicate that a single parameter K_{st}, as in the elastic case, completely prescribes the stresses, strains, and displacements near a crack tip.

The energy criterion of linear-elastic fracture mechanics is well known. Linear-elastic fracture mechanics

can also be established by the consideration of the characteristic crack tip stresses and strains. When a metallic specimen yields because of plastic deformation, the crack tip stresses and strains are not accurate when using Equations 9.4 and 9.5. It has been shown that, even with small scale yielding, the crack tip stresses and strains are characterized by the stress intensity factor (K). In other words, there exists a set of values of crack tip stresses and strains corresponding specifically to a given value of K.

9.2 Experimental results

In this section, the deformed characteristics of fatigue cracks will be described. For the specimen in plane stress, the intensity of plastic deformation is higher and the extent larger than that of plane strain, provided plastic deformation in those two cases takes place independently. Nevertheless, the plane-strain region in the interior of a thick specimen restrains the deformation in the plane-stress region on the specimen surface. The specimens used in this investigation were 1/8 inch (3.175 mm) thick and one can assume that the plane-stress exists everywhere in the sheet specimen.

The y-direction strains (ε_y) ahead of the crack tip, in the direction perpendicular to the load applied, were measured with the moiré method. The description for applying moiré grille onto the specimen surface was provided in

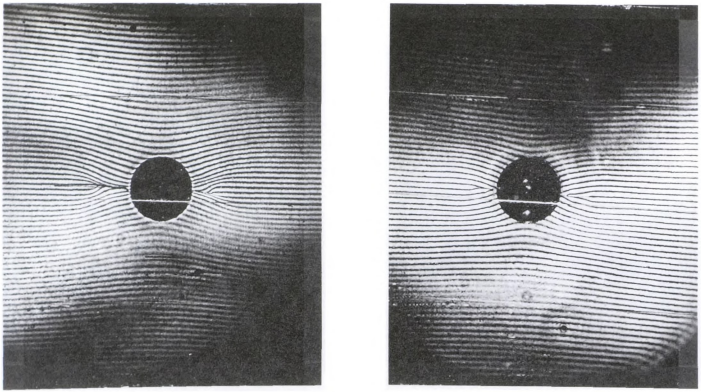

(a) (b)

Figure 9.1 Moiré fringe pattern of 3 mm crack from the hole edge in the test specimens; (a) non-coldworked, (b) coldworked.

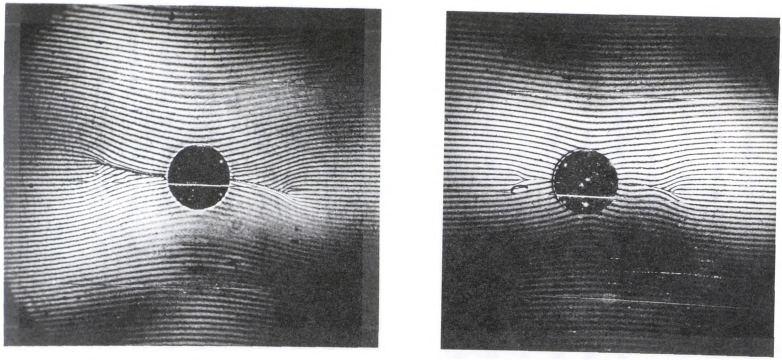

(a) (b)

Figure 9.2 Moiré fringe pattern of 6 mm crack from the hole edge in the test specimens; (a) non-coldworked, (b) coldworked.

Section 2.3. The strains were measured at the crack length of 3 mm and 6 mm from the hole edge. Figures 9.1 and 9.2 show the moiré fringe patterns by mismatch method at 3 mm and 6 mm crack from the hole edge subjected to the peak load for non-coldworked and coldworked specimens respectively.

The strains were measured at both maximum load and zero load. To measure the maximum strains, the photoresist coating was first exposed to the moiré grille at zero load with the grille line parallel to the crack line to record initial mismatch strain at the undisturbed area. The second exposure to the same grille was made at the maximum load. The subtraction between first and second exposure will determine the maximum strains. The strains at zero load caused by plastic deformation were also measured with the same procedure as the maximum strains.

Figures 9.3 and 9.4 compare the measured and calculated strains, both ε_{max} and ε_{zero}, ahead of the crack tip for the non-coldworked specimens. The solid line was calculated from the elastic formula with plastic zone correction factor, the dashed line was calculated from the plastic formula defined by Hutchinson (58). The maximum stress applied to the test specimen was 30 Ksi (207 MPa) using the elastic formula with the plastic zone correction factor, the corresponding K_I = 27.8 Ksi $\sqrt{in.}$ (30.5 MPa $\sqrt{m}$) for the crack length of 3 mm and K_I = 32.8 Ksi $\sqrt{in.}$ (36.0 MPa $\sqrt{m}$) for the crack length of 6 mm. The measurement

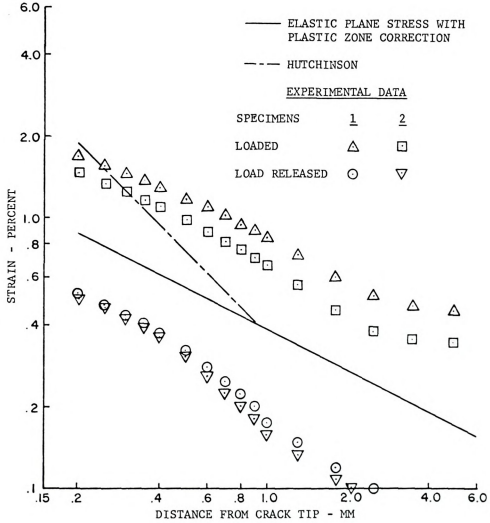

Figure 9.3 Comparison of measured strains ahead of crack tips with two theories at a crack length of 3 mm from the hole edge for non-coldworked specimens.

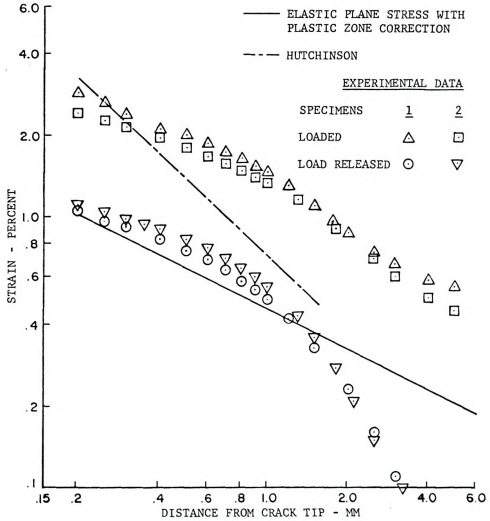

Figure 9.4 Comparison of measured strains ahead of crack tips with two theories at a crack length of 6 mm from the hole edge for non-coldworked specimens.

results have the values between the theories at an area very close to the crack tip and become higher for the area away from the crack tip. For the long crack length (6 mm), the difference in the measured and the elastically calculated ε_{max} becomes larger. Note that the ε_{zero} due to plastic deformation increases for the longer crack length.

The comparison between the measured and calculated strains for the coldworked specimens is also shown in Figures 9.5-9.8. The experimental data obtained for ε_{max} still have the value between that of the theories, but the difference in the measured and calculated ε_{max} is smaller than the non-coldworked specimens. The measured ε_{zero} of the specimens that had been coldworked is also smaller than the specimens that had not been coldworked.

9.3 Discussion of Results

The large difference in the measured and calculated strains was caused by crack tip necking. The strip necking zone was embedded in a diffused plastic zone, it took place when the size of the plastic zone was large compared with the specimen thickness. These experimental results agree with the results by Liu-Ke (61). They measured the strains ahead of the crack tip in the infinite plate of 2024-T351 aluminum with moiré method which is the same as the experimental technique used in this investigation.

The large size of the plastic zone in the test specimen compared with the crack length may have caused the

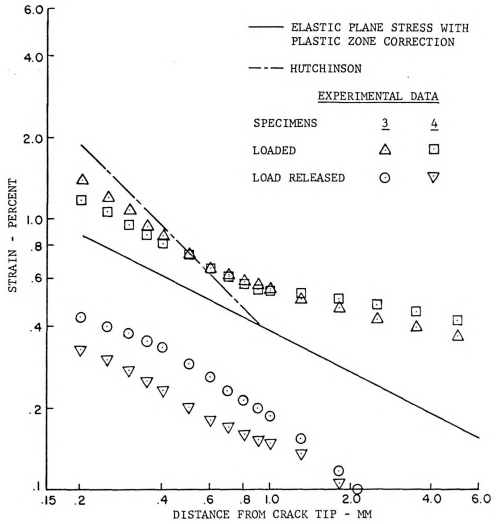

Figure 9.5 Comparison of measured strains ahead of crack tips with two theories at a crack length of 3 mm from hole edge for medium coldworked specimens.

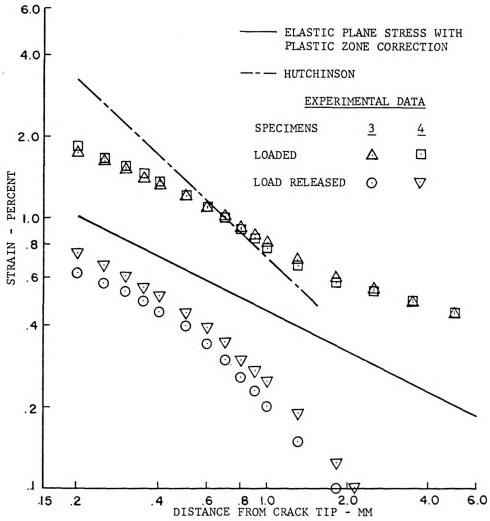

Figure 9.6 Comparison of measured strains ahead of crack tips with two theories at a crack length of 6 mm from hole edge for medium coldworked specimens.

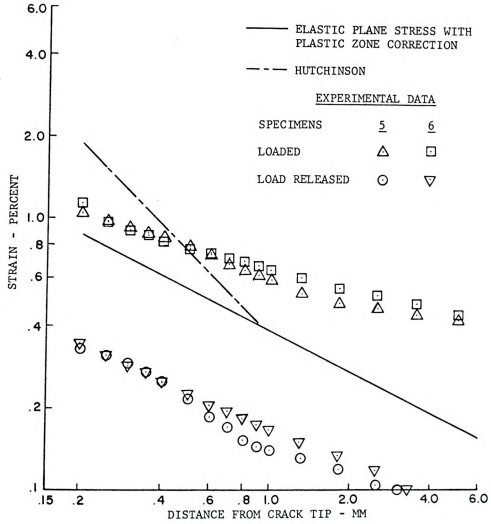

Figure 9.7 Comparison of measured strains ahead of crack tips with two theories at a crack length of 3 mm from the hole edge for heavy coldworked specimens.

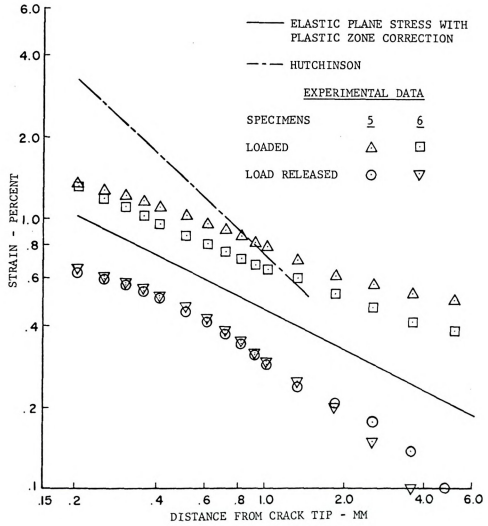

Figure 9.8 Comparison of measured strains ahead of crack tips with two theories at a crack length of 6 mm from the hole edge for heavy coldworked specimens.

disagreement problem. The radii of plastic zones in the test specimen for 3 mm and 6 mm crack were calculated by the Irwin solution and the values of 1.03 mm and 1.46 mm were obtained respectively. Those values are quite large compared with the crack lengths. The elastic solution has the better chance for the crack tip strains with small plastic zone at the crack tip compared with the crack length.

The finite width of the test specimen may have caused the large difference in the measured and calculated strains which were obtained from the infinite plate for the long crack. For example, when the cracks are 6 mm long the remote stress at the test section is 45 Ksi (310.5 MPa), this stress is quite high when compared with the remote stress of 30 Ksi (207.0 MPa) at the non-crack area. The corresponding strain at the distance away from the crack tip for the maximum load is 0.46%. If an analytical solution subjected to the crack problem existed for the strains in the finite plate, a comparison between the theoretical and experimental values could have been made.

CHAPTER 10

CONCLUSIONS

The specimens can be prepared with specific hole size so that the two specimens, when subjected to the same treatment, are nearly identical. The moiré method is quite suitable to measure the strains in this investigation. Although the large deformation at the critical areas (hole edge for coldworking process and crack tip for fatigue testing) will cause deformation of the specimen surface, the strains can be measured as close as 0.1 mm to these critical areas by the moiré technique.

Only one amount of radial expansion, 0.0040 inch (0.102 mm), was applied to 1/4 inch (6.4 mm) thick specimens with hole size of 0.26 inch (6.6 mm). The measured strains concur with the results from the indentation technique by Sharpe (13) and also with the finite element method by Adler-Dupree (12). Two amounts of radial expansion, 0.0040 inch (0.102 mm) and 0.0060 inch (0.152 mm), were applied to the 1/8 inch (3.2 mm) thick specimens with 0.196 inch (4.98 mm) hole size. The experimental results do not quite agree with the theories; values of the radial and tangential strains are higher than the theories. An industrial coldworking process for expanding the holes generates a strain distribution that varies through the thickness of the specimen near the hole.

The deformation near the hole may not be in plane stress condition; the strain on the surface opposite the sleeve lip is different from that on the surface attached to the sleeve lip. This industrial process does not produce the uniform radial expansion of the hole edge assumed by all theories. The shearing deformation associated with the pulling of the mandrel and the removal of the sleeve is important. On the vertical axis through the hole, the strains around a cold-worked hole are symmetrical. However, near the edge of the hole the strains are large, increase sharply, and become very inhomogeneous.

Fatigue tests were restricted to 1/8 inch (3.2 mm) thick specimens, a hole size of 0.196 inch (4.98 mm), and the constant-amplitude cyclic loading of 30.1 Ksi (207.7 MPa) maximum and 3.1 Ksi (21.4 MPa) minimum. This study shows that the crack initiation life for the non-coldworked specimen is about 60 percent compared with the coldworked ones and increasing the amount of coldwork will reduce the crack initiation life but improve the fatigue life of the 7075-T6 aluminum specimens.

Although the theoretical solutions for the local stress were derived with a monotonic stress-strain relation, their applicability compared to the experimental data under cyclic condition is good. Neuber's rule is fairly reliable when the nominal strain reaches yield and the condition becomes plastic. The cyclic dependent hardening and

softening behavior for the material used in this investigation is very small. No plastic deformation was observed at the hole edge during the first ten cycles. Very small plastic deformation occurred at 100 cycles and fairly large local residual strains developed for each increment of cycles in the non-coldworked specimens, but very small in the coldworked specimens.

The plot of total strain-amplitudes against initiation cycles, after suitable corrections for mean strain showed that the Smith-Hirschberg-Manson solution is valid. Comparison of total strain versus number of cycles to initiation in smooth and notched specimens indicated that this method is quite convenient and accurate enough for notch strain ranges less than about 1.0 percent.

Crack propagation and the growth rates were studied in both non-coldworked and coldworked specimens. The results show that the fracture surfaces for the coldworked ones do not show any clear striations. Striations could hardly be identified even at a magnification of 100 in Figure 5.5(b). Crack growth rates of the coldworked specimens at the area close to the hole edge are much slower than the non-coldworked ones because of the dramatic reduction of the local stress caused by compressive residual stress. The load-displacement curves in this study show the initial nonlinear region associated with fatigue crack closure and the linear portion after the crack faces are completely separated. Care was taken in the data reduction scheme to

ensure the linear portion of the curve was used to compute the stress intensity factor curve.

The experimental results of stress intensity factor obtained by the fatigue crack growth rate method and the IDG techniques agree well with the Bowie solution for the non-coldworked holes. For the coldworked holes, these experimental results agree quite well with the predictions made by linear superposition solution for longer crack lengths. The compressive yield stress in the coldworked specimens caused disagreement between theoretical and measured stress intensity factor at the area very near the hole edge. The actual cracks examined here were not perfectly straight on a microscale as assumed in the theories; this presents a likely source of error.

The crack mouth displacement determined by the least square polynomial from the finite element method by Grandt (11) compared favorably with the experimental data obtained from the IDG technique. The results of the crack surface profiles in this study turned out as predicted in the Orange solution (54). The slight difference between theoretical and measured data for the coldworked specimens at the area close to the hole edge was caused by the residual compressive stresses which decrease the amount of crack opening and also the unequal crack length on both sides of the hole at the same cycle.

The crack tip deformations for these cyclic strains have been successfully measured by the moiré method. Due to

recent developments in photoprinting, moiré method can measure the small crack tip strains quite accurately. Crack tip necking has been observed in the thin specimens used in this investigation. Elastic calculations with plastic zone correction factor correlate reasonably well for short crack length and small plastic deformation around the crack tip.

Plastic calculations of Hutchinson (58) are fairly good for long crack length and large plastic deformation. To establish the near-tip strains (NTS) criteria for ductile fractures, a convenient method to measure such a physical parameter has to be developed, especially for the specimens with finite width to count for the increasing strains at the test section for the long crack length. The effect of plate thickness and strain hardening rate must also be studied thoroughly in order to provide better accuracy of the strains near the crack tip.

The experimentally measured results in this research are restricted to the specified hole size, plate thickness, material, and constant-amplitude loading. Further research may be conducted varying these parameters. Those engaged in this kind of investigation in the near future will find the results of this study useful especially for comparison purposes.

REFERENCES

1. Nadai, A., "Theory of the Expanding of Boiler and Condenser Tube Joints Through Rolling," Transactions, American Society of Mechanical Engineers, Vol. 65, November 1943, pp. 865-880.

2. Hsu, Y. C., and R. G. Forman, "Elastic-Plastic Analysis of an Infinite Sheet Having a Circular Hole Under Pressure," Journal of Applied Mechanics, Vol. 42, No. 2, 1975, pp. 347-352.

3. Potter, R. M., and T. W. Ting, "The Problem of Forced Fittings," Archives of Rational Mechanics and Analysis, Vol. 58, No. 1, 1975, pp. 77-94.

4. Potter, R. M., and A. F. Grandt, Jr., "An Analysis of Residual Stresses and Displacements Due to Radial Expansion of Fastener Holes," Preliminary draft.

5. Ewing, Sir J. A., and J. W. C. Humfrey, "The Fracture of Metals under Repeated Alternation of Stress," Philosophical Transactions, Royal Society of London, Series A, Vol. 200, 1903, pp. 241-250.

6. Timoshenko, S. P., and J. N. Goodier, Theory of Elasticity, Third edition, New York: McGraw-Hill, 1970.

7. Howland, R. C. J., "On the Stress in the Neighbourhood of a Circular Hole in a Strip Under Tension," Philosophical Transactions, Royal Society of London, Vol. 229, 1930, pp. 49-86.

8. Neuber, H., "Theory of Stress Concentration for Shear Strained Prismatic Bodies with Arbitrary Nonlinear Stress Strain Law," Journal of Applied Mechanics, Vol. 28, No. 4, 1961, pp. 544-550.

9. Stowell, E. Z., "Stress and Strain Concentration at a Circular Hole in an Infinite Plate," NACA Technical Note No. 2073, National Advisory Committee for Aeronautics, 1950.

10. Bowie, O. L., "Analysis of an Infinite Plate Containing Radial Cracks Originating from the Boundary of an Internal Circular Hole," Journal of Mathematics and Physics, Vol. 35, 1956, pp. 60-71.

11. Grandt, A. F., Jr., "Stress Intensity Factors for Some Thru-Cracked Fastener Holes," International Journal of Fracture, Vol. 11, No. 2, April 1975, pp. 283-294.

12. Adler, W. F., and D. M. Dupree, "Stress Analysis of Coldworked Fastener Holes," AFML-TR-74-44, Air Force Materials Laboratory, Wright-Patterson Air Force Base, July 1974.

13. Sharpe, W. N., Jr., "Measurement of Residual Strains Around Coldworked Fastener Holes," AFOSR-TR-77-0020, April 1976.

14. Grandt, A. F., and T. D. Hinnerichs, "Stress Intensity Factor Measurements for Flawed Fastener Holes," Preliminary draft.

15. Durelli, A. J., and V. J. Parks, Moiré Analysis of Strain, Englewood Cliffs, N. J.: Prentice-Hall, Inc., 1970.

16. Vinckier, A., and R. Dechaene, "Use of the Moiré Effect to Measure Plastic Strains," Journal of Basic Engineering, Vol. 82, Series D, June 1960, pp. 426-434.

17. Sciammarella, C. A., and A. J. Durelli, "Moiré Fringe as a Means of Analyzing Strains," Journal of Engineering Mechanics Division, Vol. 87, February 1961, pp. 55-74.

18. Cloud, G. L., "Slotted Apertures for Multiplying Grating Frequencies and Sharpening Fringe Patterns in Moiré Photography," AFML-TR-76-164, Air Force Materials Laboratory, Wright-Patterson Air Force Base, January 1977.

19. Duffy, D., "Measurement of Surface Displacement Normal to the Line of Sight," Experimental Mechanics, Vol. 14, No. 9, September 1974, pp. 378-384.

20. Crosley, P. B., S. Mostovoy, and F. J. Ripling, "An Optical-Interference Method for Experimental Stress Analysis of Cracks Structures," Engineering Fracture Mechanics, Vol. 4, No. 3, 1971, pp. 421-433.

21. Sommer, E., "An Optical Method for Determining the Crack-Tip Stress Intensity Factor,: Engineering Fracture Mechanics, Vol. 1, 1970, pp. 705-718.

22. Sharpe, W. N., Jr., "Interferometric Surface Strain Measurement," International Journal of Non-destructive Testing, Vol. 3, 1971, pp. 56-76.

23. Paris, P. C., and G. C. Sih, "Stress Analysis of Cracks," Fracture Toughness Testing and Its Applications, ASTM STP 381, American Society for Testing and Materials, 1965, pp. 30-81.

24. Elber, W., "The Significance of Fatigue Crack Closure," Damage Tolerance in Aircraft Structures, ASTM STP 486, American Society for Testing and Materials, 1971, pp. 230-242.

25. Manson, S. S., "Interfaces Between Fatigue, Creep, and Fracture," International Journal of Fracture Mechanics, Vol. 2, No. 1, March 1966, pp. 327-363.

26. Little, R. W., Elasticity, Englewood Cliffs, N.J.: Prentice-Hall, Inc., 1973.

27. Gough, H. J., and W. A. Wood, "A New Attack Upon the Problem of Fatigue of Metals, Using X-Ray Method of Precision," Proceedings of Royal Society of London, Series A, Vol. 154, 1936, pp. 510-522.

28. Gough, H. J., and D. Hansen, "The Behavior of Metals Subjected to Repeated Stresses," Proceedings of Royal Society of London, Series A, Vol. 104, 1923, pp. 538-565.

29. Orowan, E., "Theory of the Fatigue of Metals," Proceedings of Royal Society of London, Series A, Vol. 171, 1939, pp. 79-105.

30. Head, A. K., "The Mechanism of Fatigue of Metals," Journal of the Mechanics of Physics of Solids, Vol. 1, 1953, pp. 134-141.

31. Hempel, M., in A. M. Freudenthal, Ed., Fatigue in Aircraft Structures, Academic, New York, 1956.

32. Avery, D. H., and W. A. Backofen, in D. C. Drucker, Ed.-in-Chief, Fracture of Solids, Wiley, New York, 1963.

33. Manson, S. S., and M. H. Hirschberg, "Crack Initiation and Propagation in Notched Fatigue Specimens," Proceedings of the First International Conference of Fracture, The Japanese Society for Strength and Fracture of Materials, Vol. 1, September 1965, pp. 479-498.

34. Crews, J. H., Jr., "Crack Initiation at Stress Concentrations as Influenced by Prior Local Plasticity, Achievement of High Fatigue Resistance in Metals and Alloys," ASTM-STP-467, American Society for Testing Materials, 1970, pp. 37-52.

35. Stadnick, S. J., and JoDean Morrow, "Techniques for Smooth Specimen Simulation for the Fatigue Behavior of Notched Members," Testing for Prediction of Material Performance in Structures and Components, ASTM STP 515, American Society for Testing and Materials, 1972, pp. 229-252.

36. Topper, T. H., R. M. Wetzel, and JoDean Morrow, "Neuber's Rule Applied to Fatigue of Notched Specimens," Journal of Materials, Vol. 4, No. 1, March 1969, pp. 200-209.

37. Rich, D. L., and L. F. Impellizzeri, "Fatigue Analysis of Coldworked and Interference Fit Fastener Holes," A Report of McDonnell Aircraft Company, 1976.

38. Griffith, G. E., "Experimental Investigation of the Effects of Plastic Flow in a Tension Panel with a Circular Hole," NACA Technical Note No. 1705, National Advisory Committee for Aeronautics, 1949.

39. Smith, R. W., M. H. Hirschberg, and S. S. Manson, "Fatigue Behavior of Materials Under Strain Cyclic in Low and Intermediate Life Range," NASA Technical Note D-1574, National Aeronautics and Space Administration, April 1963.

40. Morrow, JoDean, "Cyclic Plastic Strain Energy and Fatigue of Metals," International Friction Damping, and Cyclic Plasticity, ASTM STP 378, American Society for Testing and Materials, 1965, pp. 45-87.

41. Martin, J. F., "Fatigue Damage Analysis for Irregular Shaped Structures Subjected to Representative Loads," FCP Report No. 10, College of Engineering, University of Illinois, Urbana, Illinois, December 1973.

42. Endo, T., and JoDean Morrow, "Cyclic Stress-Strain and Fatigue Behavior of Representative Aircraft Metals," Journal of Materials, Vol. 4, No. 1, March 1969, pp. 159-175.

43. Impellizzeri, L. F., "Cumulative Damage Analysis in Structural Fatigue," Effect of Environment and Complex Load History on Fatigue Life, ASTM STP 462, American Society for Testing and Materials, 1970, pp. 40-68.

44. Regalbuto, J. A., and O. E. Wheeler, "Stress Distribution from Interference Fits and Uniaxial Tension," Experimental Mechanics, Vol. 10, No. 7, July 1970, pp. 274-280.

45. Petrak, G. J., and R. P. Stewart, "Retardation of Cracks Emanating from Fastener Holes," Engineering Fracture Mechanics, Vol. 6, No. 2, September 1974, pp. 275-282.

46. Christensen, R. H., and M. B. Harmon, in Fatigue Crack Propagation, ASTM STP 415, American Society for Testing and Materials, 1967, pp. 5-24.

47. Paris, P., and F. Erdogan, "A Critical Analysis of Crack Propagation Laws," Journal of Basic Engineering, Vol. 85, Series D, No. 4, December 1963.

48. Jacoby, G., "Application for Microfractography to the Study of Crack Propagation Under Fatigue Stresses," AGARD Report No. 541, Advisory Group for Aerospace Research and Development, 1966.

49. Phillips, J. L., "Sleeve Coldworking Fastener Holes," AFML-TR-74010, Vol. 1, Air Force Material Laboratory, Wright Patterson Air Force Base, February 1974.

50. Sharpe, W. N., Jr., and A. F. Grandt, Jr., "A Preliminary Study of Fatigue Crack Retardation Using Laser Interferometry to Measure Crack Surface Displacements," Mechanics of Crack Growth, ASTM STP 590, American Society for Testing and Materials, 1976, pp. 302-320.

51. Inglis, C. E., "Stresses in a Cracked Plate Due to the Presence of Cracks and Sharp Corners," Transactions of Naval Architects, Vol. 60, No. 213, 1913.

52. Emery, A. F., "Stress Intensity Factor for Thermal Stresses in Thick Hollow Cylinders," Journal of Basic Engineering, Series D, March 1966, pp. 45-52.

53. Rice, J. R., "Some Remarks on Elastic Crack-Tip Stress Fields," International Journal of Solids and Structures, Vol. 8, No. 6, 1972, pp. 751-758.

54. Orange, T. W., "Crack Shapes and Stress Intensity Factors for Edge-Cracked Specimens," Stress Analysis and Growth of Cracks, Proceedings of the 1971 National Symposium on Fracture Mechanics, Part I, ASTM STP 513, American Society for Testing and Materials, 1972, pp. 71-78.

55. Irwin, G. R., "Plastic Zone Near a Crack and Fracture Toughness," Proceedings of Seventh Sagamore Conference IV-63, 1960.

56. Dugdale, D. S., "Yielding of Steel Sheets Containing Slits," Journal of the Mechanics and Physics of Solids, Vol. 8, 1960, pp. 100-108.

57. Rice, J. R., and A. F. Rosengren, "Plane Strain Deformation Near a Crack Tip in a Power Law Hardening Material," Journal of the Mechanics and Physics of Solids, Vol. 16, 1968, pp. 1-12.

58. Hutchinson, J. W., "Plastic Stress and Strain Fields at a Crack Tip," Journal of the Mechanics and Physics of Solids, Vol. 16, 1968, pp. 337-347.

59. Oppel, G. U., and P. W. Hill, "Strain Measurements at the Roots of Cracks and Notches," Experimental Mechanics, Vol. 4, No. 7, July 1964, pp. 206-211.

60. Kobayashi, A. S., W. L. Engstrom, and B. R. Simon, "Crack-Opening Displacement and Normal Strains in Centrally Notched Plates," Experimental Mechanics, Vol. 9, 1969, pp. 163-170.

61. Liu, H. W., and J. S. Ke, "Moiré Method," in Experimental Techniques in Fracture Mechanics, Vol. 2, Iowa State University Press, Ames, Iowa, 1975.

62. Underwood, J. H., and D. P. Kendall, "Measurement of Microscopic Plastic-Strain Distribution in the Region of a Crack Tip," Experimental Mechanics, Vol. 9, 1969, pp. 296-304.

APPENDIX A

CRACK GROWTH DATA

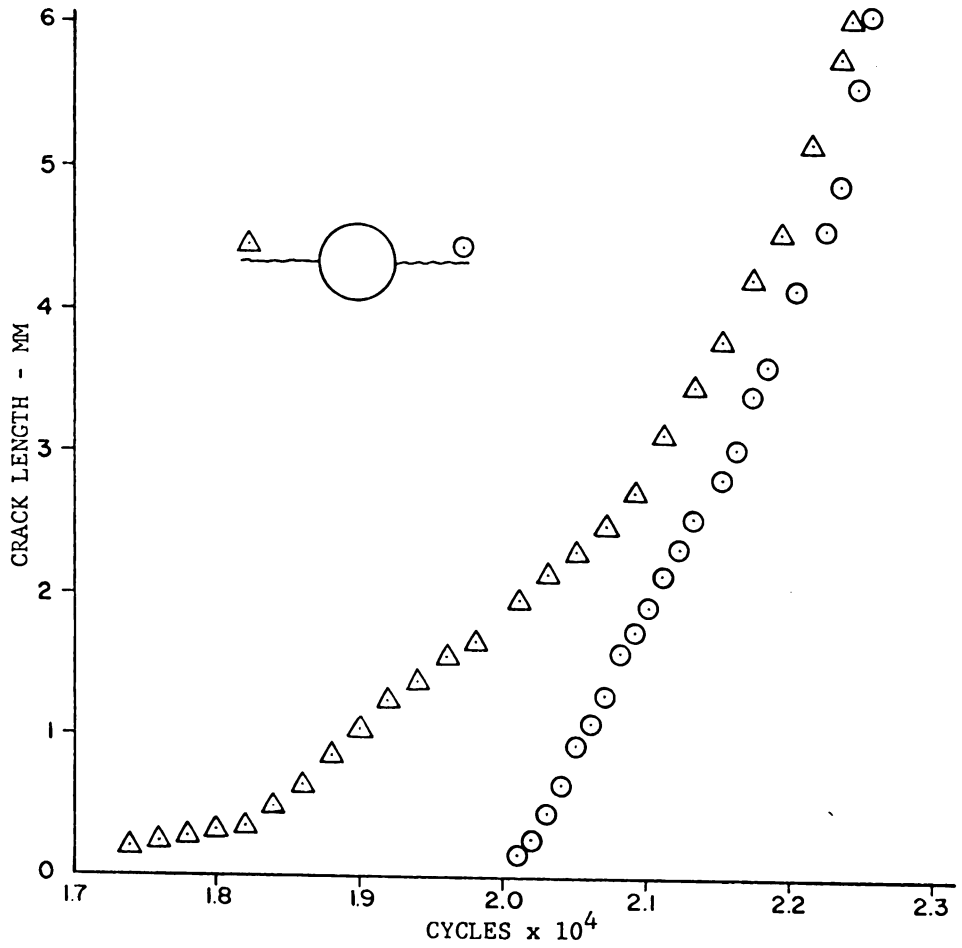

Figure A.1 Crack growth data for specimen no. 1 (non-coldworked.

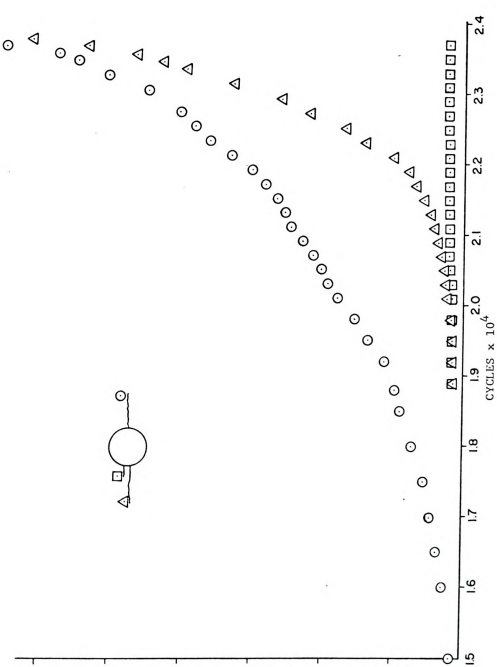

Figure A.2 Crack growth data for specimen no. 2 (non-coldworked).

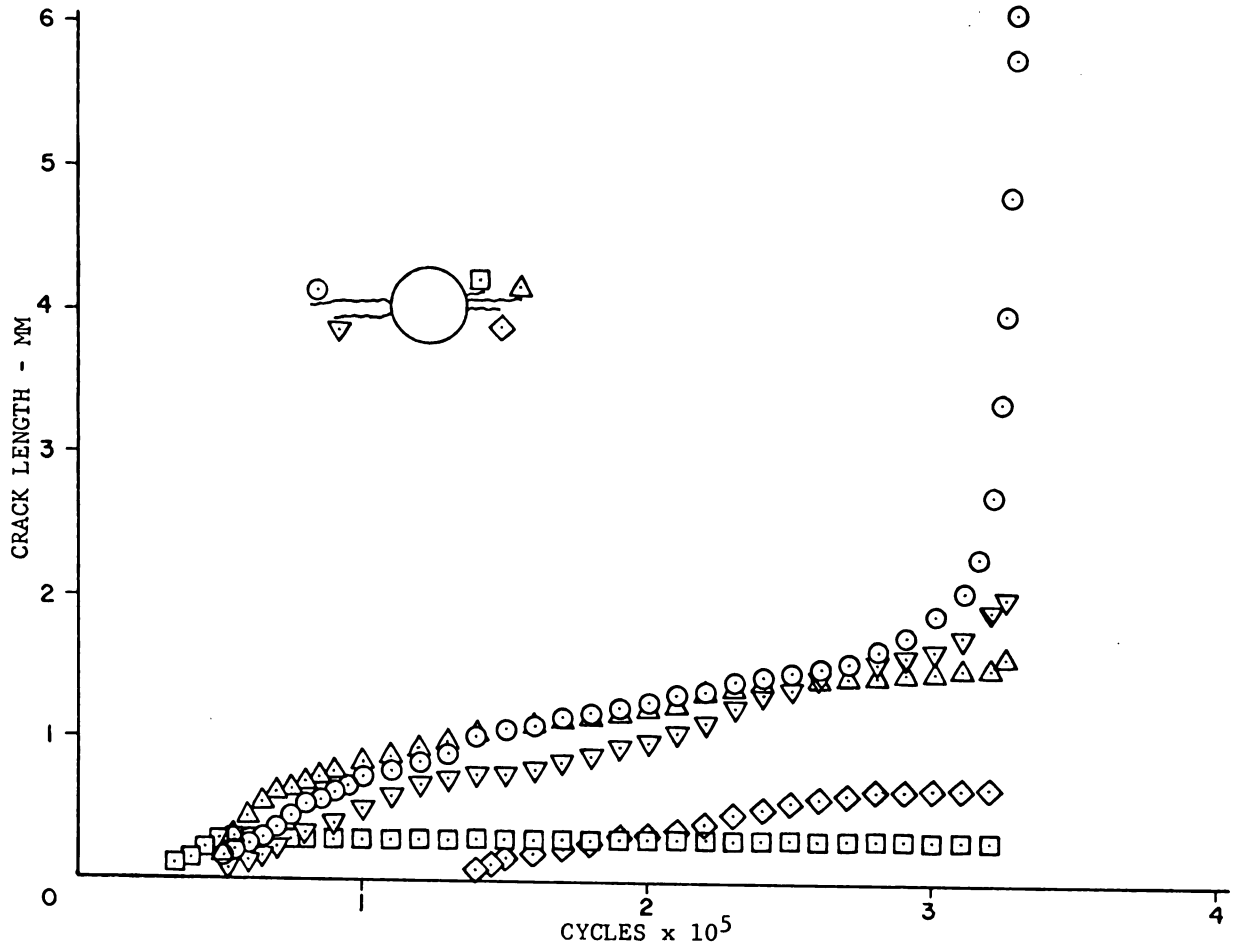

Figure A.3 Crack growth data for specimen no. 3 (medium coldworked).

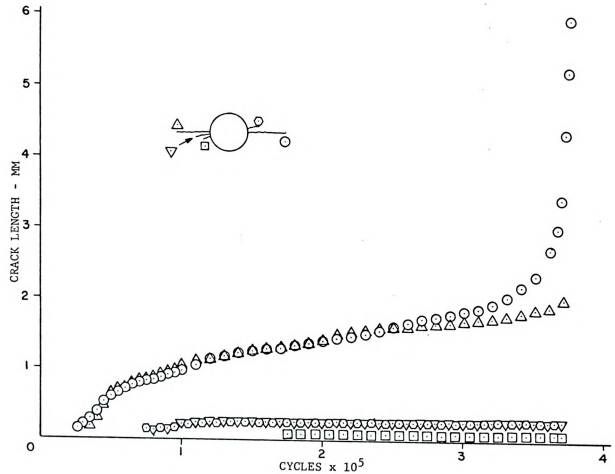

Figure A.4 Crack growth data for specimen no. 4 (medium coldworked).

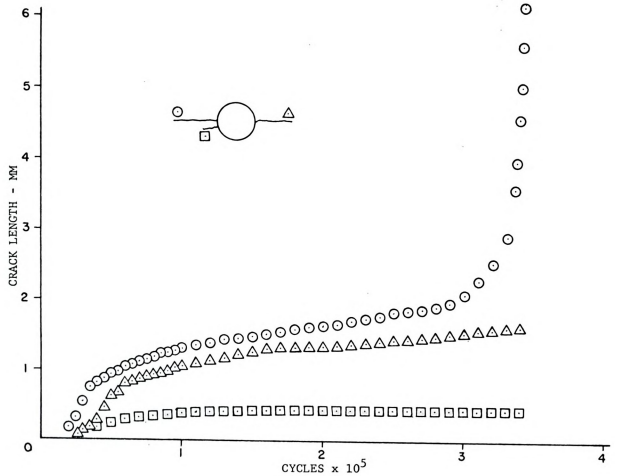

Figure A.5 Crack growth data for specimen no. 5 (heavy coldworked).

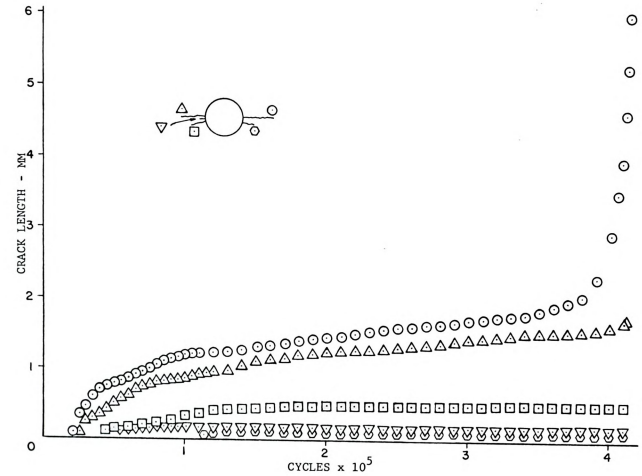

Figure A.6 Crack growth data for specimen no. 6 (heavy coldworked).

APPENDIX B

LOAD-DISPLACEMENT DATA

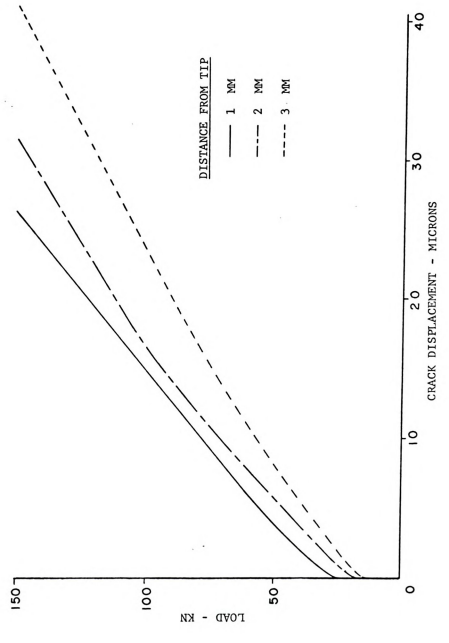

Figure B.1 Load-displacement curves obtained interferometrically at a crack length of 3 mm for non-coldworked specimen.

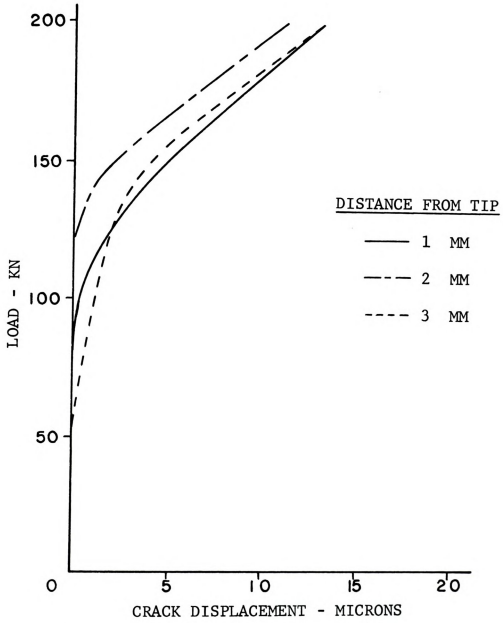

Figure B.2 Load-displacement curves obtained interferometrically at a crack length of 3 mm for medium coldworked specimen.

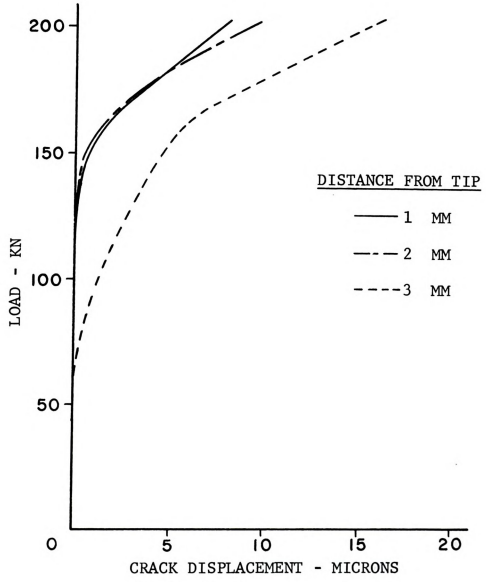

Figure B.3 Load-displacement curves obtained interferometrically at a crack length of 3 mm for heavy coldworked specimen.

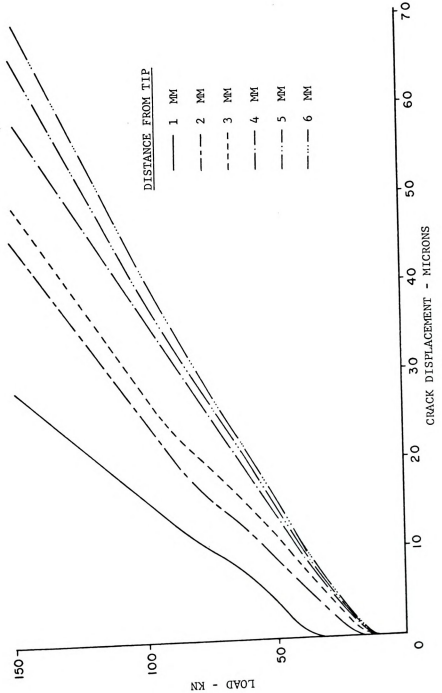

Figure B.4 Load-displacement curves obtained interferometrically at a crack length of 6 mm for non-coldworked specimen.

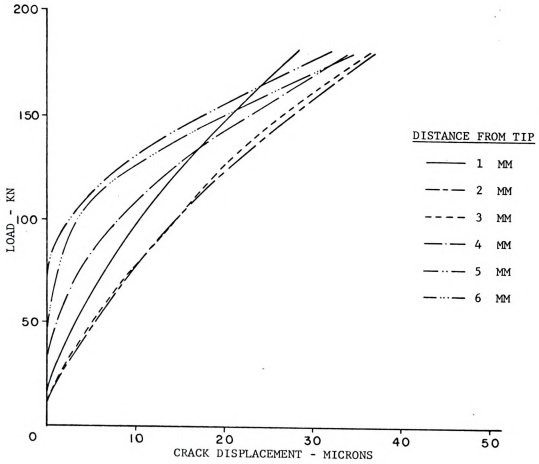

Figure B.5 Load-displacement curves obtained interferometrically at a crack length of 6 mm for medium coldworked specimen.

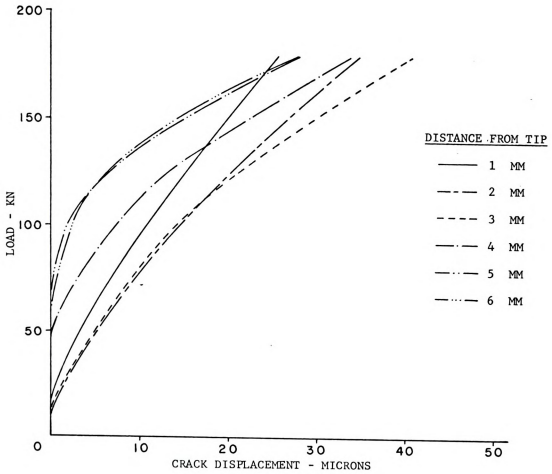

Figure B.6 Load-displacement curves obtained interferometrically at a crack length of 6 mm for heavy coldworked specimen.